

MONTE CARLO ANALYSIS OF THE EFFECTS OF MATERIAL AND SHAPE  
UNCERTAINTIES ON RADAR CROSS SECTION BY THE FINITE DIFFERENCE TIME  
DOMAIN METHOD

A THESIS SUBMITTED TO  
THE GRADUATE SCHOOL OF NATURAL AND APPLIED SCIENCES  
OF  
MIDDLE EAST TECHNICAL UNIVERSITY

BY

ALI KEMAL KAZAR

IN PARTIAL FULLFILLMENT OF THE REQUIREMENTS  
FOR  
THE DEGREE OF MASTER OF SCIENCE  
IN  
ELECTRICAL AND ELECTRONICS ENGINEERING

JULY 2013



Approval of the thesis:

**MONTE CARLO ANALYSIS OF THE EFFECTS OF MATERIAL AND SHAPE  
UNCERTAINTIES ON RADAR CROSS SECTION BY THE FINITE DIFFERENCE TIME  
DOMAIN METHOD**

submitted by **ALİ KEMAL KAZAR** in partial fulfillment of the requirements for the degree of  
**Master of Science in Electrical and Electronics Engineering Department, Middle East  
Technical University** by,

Prof. Dr. Canan Özgen  
Dean, Graduate School of **Natural and Applied Sciences**

\_\_\_\_\_

Prof. Dr. Gönül Turhan Sayan  
Head of Department, **Electrical and Electronics Engineering**

\_\_\_\_\_

Prof. Dr. Mustafa Kuzuoğlu  
Supervisor, **Electrical and Electronics Engineering Dept., METU**

\_\_\_\_\_

Assoc. Prof. Dr. Özlem Özgün  
Co-supervisor, **Electrical and Electronics Engineering Dept., TEDU**

\_\_\_\_\_

**Examining Committee Members**

Prof. Dr. Gönül Turhan Sayan  
Electrical and Electronics Engineering Dept., METU

\_\_\_\_\_

Prof. Dr. Mustafa Kuzuoğlu  
Electrical and Electronics Engineering Dept., METU

\_\_\_\_\_

Assoc. Prof. Dr. Özlem Özgün  
Electrical and Electronics Engineering Dept., TEDU

\_\_\_\_\_

Prof. Dr. Gülbin Dural  
Electrical and Electronics Engineering Dept., METU

\_\_\_\_\_

Prof. Dr. Özlem Aydın Çivi  
Electrical and Electronics Engineering Dept., METU

\_\_\_\_\_

**Date: 05.07.2013**

**I hereby declare that all information in this document has been obtained and presented in accordance with academic rules and ethical conduct. I also declare that, as required by these rules and conduct, I have fully cited and referenced all material and results that are not original to this work.**

Name, Last name : Ali Kemal Kazar

Signature :

## ABSTRACT

### **MONTE CARLO ANALYSIS OF THE EFFECTS OF THE MATERIAL AND SHAPE UNCERTAINTIES ON RADAR CROSS SECTION BY THE FINITE DIFFERENCE TIME DOMAIN METHOD**

Kazar, Ali Kemal  
M.S., Department of Electrical and Electronics Engineering  
Supervisor: Prof. Dr. Mustafa Kuzuoğlu  
Co-supervisor: Assoc. Prof. Dr. Özlem Özgün

July 2013, 86 pages

The aim of this research is to analyze the variations in Radar Cross Section (RCS) values of dielectric and conducting objects due to material and shape uncertainties by employing the Finite Difference Time Domain Method and the Monte Carlo approach in electromagnetic scattering problems. MATLAB codes are developed and validated to solve the electromagnetic scattering problem involving two and three dimensional arbitrarily-shaped objects. Basic principles of FDTD and its implementation in MATLAB are described. Based on the two-dimensional FDTD code, the results of several Monte Carlo simulations are presented by varying the relative permittivity and the geometry of the object. Several conclusions are drawn by post processing the coherent and incoherent components of the RCS values. The results are compared with Method of Moments results and analytical results if available, and a good agreement among the results is observed.

Keywords: Finite Difference Time Domain Method, Radar Cross Section, Monte Carlo Method, PEC objects, Dielectric objects, Effect of uncertainties, Electromagnetic scattering, MATLAB.

## ÖZ

### **ZAMANDA SONLU FARKLAR YÖNTEMİYLE MATERYAL VE ŞEKİL BELİRSİZLİKLERİNİN RADAR KESİT ALANINA ETKİLERİNİN MONTE CARLO YAKLAŞIMIYLA ANALİZ EDİLMESİ**

Kazar, Ali Kemal  
Yüksek Lisans, Elektrik-Elektronik Mühendisliği Bölümü  
Tez Yöneticisi: Prof. Dr. Mustafa Kuzuoğlu  
Ortak Tez Yöneticisi: Doç. Dr. Özlem Özgün

Temmuz 2013, 86 sayfa

Bu araştırmanın amacı elektromanyetik saçılma problemlerinden olan materyal ve şekildeki belirsizliklerin, yalıtkan ve iletken nesnelere Radar Kesit Alanı'ndaki değişimi üzerindeki etkisinin Zamanda Sonlu Farklar ve Monte Carlo yaklaşımıyla analiz edilmesidir. İki ve üç boyutlu herhangi bir şekle sahip nesnelere içeren elektromanyetik saçılma problemlerini çözebilmek amacıyla MATLAB kodları oluşturulmuştur ve geçerlilikleri kontrol edilmiştir. FDTD'nin temel adımlarıyla bunların MATLAB üzerindeki gerçeklemeleri tanıtılmıştır. İki boyutlu FDTD kodu temel alınarak, Monte Carlo simülasyonu ile göreceli dielektrik katsayısı ve geometrideki değişimleri içeren birçok sonuç sunulmuştur. Sonradan işleme tabi tutulan RCS'in ortalama ve standart sapma değerleri sayesinde birçok sonuç çıkarılmıştır. Mümkün olduğu durumda sonuçlar analitik ve Momentler Metodu yöntemlerinin sonuçlarıyla karşılaştırılmıştır ve aralarında yeterli bir uyum gözlenmiştir.

Anahtar Kelimeler: Zamanda Sonlu Farklar Yöntemi, Radar Kesit Alanı, Monte Carlo Metodu, Mükemmel iletken cisimler, Yalıtkan cisimler, Belirsizlik etkisi, Elektromanyetik saçılma, MATLAB.

*To My Grandfather*

## ACKNOWLEDGEMENTS

I would like to record my gratitude to Prof. Dr. Mustafa Kuzuođlu and Assoc. Prof. Dr. zlem zgün for their valuable guidance, opinions, and helpful codes they provided throughout my research.

I would like to express my thanks to my friends for their support and fellowship.

I am grateful to Aselsan Inc., who has provided the support I have needed to complete my thesis and to Tübitak, who has funded two year of my studies.

It is a pleasure to thank Cemil Meriç, Andrei Tarkovsky, Albert Camus, and Rene Guenon for their invaluable contribution to humanity.

Last but not least, I am grateful in my very heart to my merciful mother, decent father, unique sister and beloved brother for being always with me throughout my life, their endless support, love and encouragements.

## TABLE OF CONTENTS

<b>ABSTRACT .....</b>	<b>v</b>
<b>ÖZ.....</b>	<b>vi</b>
<b>LIST OF TABLES .....</b>	<b>xi</b>
<b>LIST OF FIGURES .....</b>	<b>xii</b>
<b>LIST OF ABBREVIATIONS.....</b>	<b>xiv</b>
<b>CHAPTERS</b>	
<b>1. INTRODUCTION .....</b>	<b>1</b>
1.1 Motivation .....	1
1.2 Scope of the Thesis.....	2
1.3 Our Approach .....	3
1.4 Contribution of this Thesis .....	3
1.5 Outline of Thesis .....	4
<b>2. THEORETICAL BACKGROUND .....</b>	<b>5</b>
2.1 Fundamentals of Finite Difference Time Domain Method.....	5
2.1.1 Discretization .....	6
2.1.2 Perfectly Matched Layer (PML) .....	10
2.1.3 The Total-Field / Scattered-Field .....	16
2.2 Near to Far Field Transformation .....	17
2.2.1 Phasor Domain Technique .....	17
2.2.2 Time Domain Technique .....	21
<b>3. FDTD IMPLEMENTATION METHOD.....</b>	<b>23</b>
3.1 Main Implementation Steps .....	24
3.1.1 The FDTD Wave Implementation (TM <sub>z</sub> 2-D and 3-D).....	24
3.1.2 The PML Implementation (TM <sub>z</sub> 2-D and 3-D) .....	28
3.1.3 Total / Scattered Field Boundary Implementation (TM <sub>z</sub> 2-D and 3-D).....	34
3.2 Simulation Results .....	36
3.2.1 2-D TM <sub>z</sub> Results.....	36
3.2.2 3-D Results .....	38
3.3 “1/2” Problem between the Electric and Magnetic Fields .....	40
3.3.1 Temporal Offset Effect on Signal.....	40
3.3.2 Spatial Offset Effect on Signal .....	41
<b>4. EFFECTS OF MATERIAL AND/OR SHAPE UNCERTAINTIES OVER RCS .....</b>	<b>43</b>
4.1 Effect of Material and Shape Uncertainties over RCS.....	43
4.1.1 Results for Permittivity Uncertainties .....	43
4.1.2 Results for Shape Uncertainties.....	54
4.2 Effect of a Small-size Secondary Object over the RCS of a Main object.....	66

4.2.1	Effect of the Dimension of the Secondary Object over RCS .....	66
4.2.2	RCS Analysis in Plane-Missile Model.....	70
4.2.3	Effect of the Distance between the Main and Secondary Objects over RCS .....	73
<b>5.</b>	<b>CONCLUSIONS AND FUTURE WORK .....</b>	<b>79</b>
5.1	Summary .....	79
5.2	Future Work .....	80
	<b>REFERENCES .....</b>	<b>81</b>
	<b>APPENDICES</b>	
<b>A.</b>	<b>ANALYTICAL RCS CALCULATION FOR CIRCULAR CYLINDERS (2-D – <math>TM_z</math>)....</b>	<b>85</b>

## LIST OF TABLES

TABLES	
<i>Table 2-1 Principal Component Analysis</i> .....	20
<i>Table 4-1 Evaluation of Code for (<math>\mu_m = 3</math> and <math>\sigma_{sd} = 0.1</math>)</i> .....	49
<i>Table 4-2 Evaluation of Code for (<math>\mu_m = 3</math> and <math>\sigma_{sd} = 0.5</math>)</i> .....	50
<i>Table 4-3 Mean and Standard Deviation of Forward RCS in Figure 4-25</i> .....	64
<i>Table 4-4 Mean and Standard Deviation Values of Forward RCS in Figure 4-26</i> .....	65

## LIST OF FIGURES

### FIGURES

<i>Figure 2-1 Representation of Electromagnetic Field Components in a Yee Cell in Rectangular Coordinate System</i> .....	7
<i>Figure 2-2 Orientation of Field Components</i> .....	10
<i>Figure 2-3 Berenger PML Technique</i> .....	13
<i>Figure 2-4 TF / SF Region for 2D Case</i> .....	16
<i>Figure 2-5 Surface Equivalence Theorem</i> .....	18
<i>Figure 3-1 Representation of Simulation Area</i> .....	23
<i>Figure 3-2 Space Settling of the Electric and Magnetic Field</i> .....	26
<i>Figure 3-3 PML Implementation</i> .....	33
<i>Figure 3-4 Orientation of Field Vectors at the Boundary for 2-D <math>TM_z</math></i> .....	35
<i>Figure 3-5 Fields Vectors at <math>k_a</math></i> .....	36
<i>Figure 3-6 Bistatic RCS of a PEC Circular Cylinder with “<math>r = 1.5\lambda</math>”</i> .....	37
<i>Figure 3-7 Bistatic RCS of a Dielectric Circular Cylinder with “<math>\epsilon_r = 1.2</math> and <math>r = 1.5\lambda</math>”</i> .....	37
<i>Figure 3-8 Bistatic RCS of a PEC Square Cylinder with “Side-length = <math>3\lambda</math>”</i> .....	38
<i>Figure 3-9 Bistatic RCS of a Dielectric Sphere with “<math>\epsilon_r = 1.2</math> and <math>r = 2\lambda</math>”</i> .....	39
<i>Figure 3-10 Bistatic RCS of a PEC Sphere with “<math>r = 2\lambda</math>”</i> .....	39
<i>Figure 3-11 <math>TM_z</math> Grid Representation</i> .....	40
<i>Figure 3-12 Bistatic RCS of PEC Circular Cylinder with “<math>r = 4\lambda/5</math>” [16]</i> .....	42
<i>Figure 4-1 Relative Permittivity Histogram for (<math>\mu_m = 3</math> and <math>\sigma_{sd} = 0.1</math>)</i> .....	45
<i>Figure 4-2 Forward RCS Distribution via FDTD for (<math>\mu_m = 3</math> and <math>\sigma_{sd} = 0.1</math>)</i> .....	46
<i>Figure 4-3 Relative Permittivity Histogram for (<math>\mu_m = 3</math> and <math>\sigma_{sd} = 0.5</math>)</i> .....	46
<i>Figure 4-4 Forward RCS Histogram via FDTD for (<math>\mu_m = 3</math> and <math>\sigma_{sd} = 0.5</math>)</i> .....	47
<i>Figure 4-5 Forward RCS as a function of Relative Permittivity for Circular Cylinder (Radius = <math>\lambda/2</math>)</i> .....	48
<i>Figure 4-6 Forward RCS Histograms by FDTD and Analytical Method for (<math>\mu_m = 3</math> and <math>\sigma_{sd} = 0.1</math>)</i> .....	49
<i>Figure 4-7 Forward RCS Histograms via FDTD and Exact Method for (<math>\mu_m = 3</math> and <math>\sigma_{sd} = 0.5</math>)</i> .....	50
<i>Figure 4-8 Relative Permittivity Histogram for (<math>\mu_m = 3</math> and <math>\sigma_{sd} = 0.5</math>)</i> .....	51
<i>Figure 4-9 Forward RCS Histogram via FDTD for (<math>\mu_m = 3</math> and <math>\sigma_{sd} = 0.5</math>)</i> .....	52
<i>Figure 4-10 Forward RCS as a function of Relative Permittivity for Square Cylinder (Side-length=<math>\lambda</math>)</i> .....	53
<i>Figure 4-11 Relative Permittivity Histogram for (<math>\mu_m = 3</math> and <math>\sigma_{sd} = 0.1</math>)</i> .....	53
<i>Figure 4-12 Forward RCS distribution via FDTD for (<math>\mu_m = 3</math> and <math>\sigma_{sd} = 0.1</math>)</i> .....	54
<i>Figure 4-13 Circular Cylinder with an Omitted Part</i> .....	55
<i>Figure 4-14 Forward RCS Histogram via FDTD for (<math>r = 0.5\lambda</math> and <math>a = 0.1\lambda</math>)</i> .....	55
<i>Figure 4-15 Forward RCS Histogram via FDTD for (<math>r = \lambda</math> and <math>a = 0.1\lambda</math>)</i> .....	56
<i>Figure 4-16 PEC Square Cylinder with PEC Square Deformity</i> .....	57
<i>Figure 4-17 Forward RCS as a function of the angular position of the deformity via FDTD for (<math>a = 3\lambda</math> and <math>b = 0.5\lambda</math>)</i> .....	58
<i>Figure 4-18 Forward RCS as a function of the angular position of the deformity via FDTD for (<math>a = 3\lambda</math> and <math>b = 0.25\lambda</math>)</i> .....	58
<i>Figure 4-19 Histogram of the Randomly Generated <math>\theta</math> Values between <math>150^0</math>-<math>210^0</math></i> .....	59
<i>Figure 4-20 Forward RCS Histogram for Angular Position between (<math>150^0</math>-<math>210^0</math>) via FDTD for (<math>a = 3\lambda</math> and <math>b = 0.5\lambda</math>)</i> .....	60
<i>Figure 4-21 Forward RCS Histogram for Angular Position between (<math>150^0</math>-<math>210^0</math>) via FDTD for (<math>a = 3\lambda</math> and <math>b = 0.25\lambda</math>)</i> .....	61
<i>Figure 4-22 Histogram of the Randomly Generated <math>\theta</math> Values between <math>230^0</math>-<math>300^0</math></i> .....	62
<i>Figure 4-23 Forward RCS Histogram for Angular Position between (<math>230^0</math>-<math>300^0</math>) via FDTD for (<math>a = 3\lambda</math> and <math>b = 0.5\lambda</math>)</i> .....	62
<i>Figure 4-24 Forward RCS Histogram for Angular Position between (<math>230^0</math>-<math>300^0</math>) via FDTD for (<math>a = 3\lambda</math> and <math>b = 0.25\lambda</math>)</i> .....	63

Figure 4-25 Forward RCS as a function of the angular position of the deformity for ( $a = 3\lambda$ and $b = 0.5\lambda$ ).....	64
Figure 4-26 Backward RCS as a function of the angular position of the deformity via FDTD for ( $a = 3\lambda$ and $b = 0.5\lambda$ ) .....	65
Figure 4-27 Forward RCS as a function of the side-length of the secondary object for ( $a = 3\lambda$ and $\theta = 0^0$ ) .....	67
Figure 4-28 Forward RCS as a function of the side-length of the secondary object for ( $a = 3\lambda$ and $\theta = 270^0$ ) .....	67
Figure 4-29 Backward RCS as a function of the side-length of the secondary object for ( $a = 3\lambda$ and $\theta = 90^0$ ) .....	68
Figure 4-30 Backward RCS as a function of the side-length of the secondary object for ( $a = 3\lambda$ and $\theta = 180^0$ ) .....	69
Figure 4-31 Backward RCS as a function of the side-length of the secondary object for ( $a = 3\lambda$ and $\theta = 270^0$ ) .....	69
Figure 4-32 Backward RCS as a function of the angle $\theta$ for different values of the side-length of the secondary object via FDTD for ( $a = 3\lambda$ ).....	70
Figure 4-33 Simulation Area for Plane-Missile Model.....	71
Figure 4-34 Forward RCS as a function of the distance between missile and plane ( $a = 3\lambda$ and $b = 0.5\lambda$ ; and $c = \lambda$ ) .....	72
Figure 4-35 Backward RCS as a function of the distance between missile and plane ( $a = 3\lambda$ and $b = 0.5\lambda$ ; and $c = \lambda$ ) .....	72
Figure 4-36 Simulation area to observe the effect of the distance between the main and secondary objects .....	73
Figure 4-37 Forward RCS as a function of the distance between the main and secondary objects ( $a = 3\lambda$ ; $b = 0.5\lambda$ ; and $\theta = 0^0$ ).....	74
Figure 4-38 Forward RCS as a function of the distance between the main and secondary objects ( $a = 3\lambda$ ; $b = 0.5\lambda$ ; and $\theta = 90^0$ ).....	74
Figure 4-39 Backward RCS as a function of the distance between the main and secondary objects ( $a = 3\lambda$ ; $b = 0.5\lambda$ ; and $\theta = 90^0$ ).....	75
Figure 4-40 Backward RCS as a function of the distance between the main and secondary objects ( $a = 3\lambda$ ; $b = 0.5\lambda$ ; and $\theta = 180^0$ ).....	76
Figure 4-41 Backward RCS as a function of the distance between the main and secondary objects ( $a = 3\lambda$ ; $b = 0.5\lambda$ ; and $\theta = 270^0$ ).....	76
Figure 4-42 Backward RCS as a function of angle $\theta$ for different values of distance between the main and secondary objects ( $a = 3\lambda$ ; $b = 0.5\lambda$ ) .....	77

## LIST OF ABBREVIATIONS

<b>ABC</b>	Absorbing Boundary Condition
<b>PML</b>	Perfectly Matched Layer
<b>FDTD</b>	Finite Difference Time Domain
<b>MoM</b>	Method of Moments
<b>RCS</b>	Radar Cross Section
<b>PEC</b>	Perfect Electric Conductor
<b>UPML</b>	Unsplit Perfectly Matched Layer
<b>CPML</b>	Convolutional Perfectly Matched Layer
<b>CFSPML</b>	Complex Frequency Shifted PML

## CHAPTER 1

### INTRODUCTION

#### 1.1 Motivation

Researchers have tried to classify and identify the complexity in the mathematical models of natural phenomena. Their major concern was to reduce the complexity to a single law governing it. A famous example of this approach is the contributions of James Clark Maxwell to explain the natural laws of electromagnetism. The set of laws which define how electric charges and electric currents act as sources for the electric and magnetic fields and how they affect each other are translated into a systematic expression by James Clark Maxwell [1]. Electromagnetic Theory [2-5], which is directly related to Maxwell's Equations, has had an impressive impact on several areas such as industrial and military applications, telecommunications, and biomedical engineering.

Several techniques are used to deal with electromagnetic problems that can be categorized as experimental, analytical, or numerical [6]. Experimental techniques do not allow much flexibility and they are not proper to use regarding cost, and difficulty of realization aspects. Although the experimental measurements provide valuable data, the whole process can be expensive in terms of money and manpower required.

Before utilization of numerical methods, classical analytical methods like separation of variables and integral solutions have been used to solve some of the electromagnetic problems. Analytical methods required a high degree of cleverness, familiarity with mathematical methods, and computational labor to be applied. Since most of the problems have complex geometries, a limited range of practical problems, known as canonical problems, with simpler geometries could be examined. This explains why it is uncommon to solve practical electromagnetic problems by analytical approaches. Therefore, it is needed to solve electromagnetic problems by a more convenient technique giving approximate solutions of sufficient accuracy [7-9]. This was the fundamental idea behind the starting point of numerical methods to solve electromagnetic problems in 1960s with the availability of modern computers. Since then, researchers have spent a significant effort on resolving real-life, complex electromagnetic related problems which are either intractable or do not have closed form analytical solutions. Once computers became available, researchers immediately began using them to deal with electromagnetic problems that do not have analytical solutions. Furthermore, the ability to simulate the behavior of complex systems before they are actually built, is one of the basic drives behind obtaining reliable computational approaches. Not only numerical approaches have the immense practical significance for engineering work, but also numerical algorithms are wonderful tools for studying and visualizing engineering electromagnetic [10-11].

Kane Yee introduced the Finite Difference Time Domain method [12] (the name was not coined by Yee) in 1966, which solves Maxwell's equations to model electromagnetic propagation. Yee's algorithms were in the time domain and based on Maxwell's curl equations. Since then, numerous textbooks, journal papers and graduate theses have been produced to examine the Finite Difference Time Domain approach. Allen Taflovit coined the name "Finite Difference Time Domain Method (FDTD)" [13]. He is one of the most-cited researchers in FDTD [14].

Finite Difference Time Domain (FDTD) method has become probably the most popular computational approach in electromagnetic engineering [15-16]. FDTD approach is a well established, sufficiently accurate and easy-to-implement method. Wide-band information can be gathered by means of a single simulation due to being a time-domain method [17-18]. Since the physical behavior of electromagnetic fields could be observed in the computational volume by FDTD, the method is particularly functional for gathering engineering insight into complex wave interaction [19] and for educational purposes dealing with electromagnetic area.

It has become widespread practice in almost all scientific disciplines to use probability models and statistical methods in data evaluation. We demand a perfect (noiseless) world, but it must be admitted that the perfect world is only an imagination in our head. Kant stated that we reflect our mind over the nature [20]. Now, we can only talk about the statistics and probability instead of exactness. Science gives us some number depending on measurement, which has a mean (coherent component) and variance (incoherent component) [21]. Unknown conditions or lack of information can be handled via probability that allows us to speak quantitatively in terms of some consistent average behavior.

Claude Monet, one of the foremost members of the impressionist movement, has showed the uncertainty in nature in one of his influential paintings called Saint Lazare Station [22]. Not only the movement or the perfectness of nature has been painted, but also he depicted the noise, the uncertain part of the nature. Painting of Saint Lazare Station is the most rhetorical expression of noise in the outside world and only an artist can describe uncertainty in this way.

We live in an uncertain world not to be fully predicted in advance. For example, in civil engineering, structures must be built without fully knowing material properties, the wind load, etc. Engineers must be able to depict random events in a quantitative way and how these events can be incorporated into engineering analysis [23]. Although one encounters several difficulties in engineering applications due to inaccurate measurements and uncertainties, statistics and probabilistic approaches provide powerful tools for managing risk.

The main reason of using probabilistic methods in engineering is that uncertainties are unavoidable in any engineering analysis and design. Uncertainty arises due to incompleteness of the available information, natural processes and phenomena inherently random. Definite decision in such cases cannot be taken. However, decisions are required even with the incomplete information and for the natural processes [24].

Decisions in such a situation are taken under the conditions of uncertainty. Thus, the effects of uncertainty in engineering problems are important. Probability theory provides a formal basis for quantifying risk or uncertainty in engineering problems, which are otherwise being dealt with qualitatively using engineering judgments.

The role of probabilistic methods in engineering can be broadly summarized as follows: the modeling of engineering problems and evaluation of system performance under conditions of uncertainty, systematic development of design criteria, explicitly taking into account the significance of uncertainty, the logical framework for risk assessment and risk benefit tradeoff analysis relative to decision making.

The causes of uncertainties can be listed as follows: parameter uncertainties (inability in evaluating accurate model parameters, inherent variations in model parameters), data uncertainties (error in measurements, limitations in adequate representation of sample data), and operational change in set conditions.

As an example, environmental risk assessment is decided through estimation of model parameters, identification of probability distribution, determination of dependencies among variables, estimation of model uncertainties.

## **1.2 Scope of the Thesis**

This thesis deals with the development and application of the simulation methods commonly used in electromagnetic engineering in conjunction with the FDTD method. In this dissertation, it is expected to develop an appropriate MATLAB code utilizing FDTD method that has the capability of calculating the Radar Cross Section (RCS) of Perfectly Electrical Conductor (PEC) and dielectric objects in two and three dimensional (2-D, 3-D) problems.

Generating a robust RCS calculation code is one of the requirements of this thesis. FDTD is a useful method because of its effectiveness to analyze the interaction of arbitrarily-shaped objects with

electromagnetic fields. Setting the constitutive parameters within each space cell correctly is sufficient to identify an arbitrary object for FDTD technique.

Uncertainties in the constitutive parameters (i.e., permittivity, permeability, and conductivity) as well as small shape variations cause fluctuations in the radar cross section (RCS) of the object [25]. It is essential to perform an appropriate statistical characterization of randomness in objects due to the fact that such uncertainties occur frequently in realistic applications, for instance in radar surveillance, remote sensing, target tracking etc.

In this thesis, FDTD method is accompanied by the Monte Carlo technique to analyze uncertainties [23]. Monte Carlo method is based on the generation of a set of random parameters or shape imperfectness and the computation of the RCS for each such parameter or shape by employing FDTD method. Subsequently, the statistical properties of the RCS are gathered by post processing the family of calculated RCS values. The necessary computational resources increase rapidly especially for large sized problems in the Monte Carlo approach as a result of the repeated solutions of the problem.

As a result, the scope of this thesis can be summarized as calculating the effect of randomness in electromagnetic phenomena and the effect of smaller-size secondary objects (which is a simplified, canonical representation of missile – plane model) over RCS of a main object with an effective numerical method FDTD by utilizing the Monte Carlo technique.

### **1.3 Our Approach**

In this thesis, FDTD technique is adopted for the RCS computation of arbitrarily-shaped objects. Complex shaped objects are defined straightforwardly by setting the values of the constitutive parameters within each cell. Our approaches are validated by employing analytical (if possible) or some other numerical technique, such as the Method of Moments (MoM). Influence of randomness over the RCS is detected by Monte Carlo method. It is investigated how the relation between a secondary smaller object and a main object influences the behavior of RCS by changing the position and dimensions of the secondary object.

Our approach on the whole system has the following steps:

- Firstly, an effective FDTD code is developed to simulate the interaction of arbitrarily-shaped PEC or dielectric object with the electromagnetic field in near field area [26].
- Secondly, the gathered data of electromagnetic fields are converted into the phasor domain, because the FDTD is a time domain method.
- Thirdly, near field phasor (frequency domain data) values are transformed into far field to compute RCS of the object via Surface Equivalence Theorem.
- Finally, Monte Carlo algorithm is utilized to identify uncertainties and the effect of secondary object over the RCS of the main object.

### **1.4 Contribution of this Thesis**

The main contributions of this dissertation are as follows:

- FDTD algorithm is applied to examine RCS calculations of arbitrarily-shaped objects [27].
- Effect of randomness in relative dielectric constant and shape imperfectness are examined in detail. Behavior of RCS is investigated for such cases by Monte Carlo analysis.
- A real world problem, namely detecting the missile departing from a plane, is transformed into a simplified canonical model. The behavior of the RCS for this case is inferred from the FDTD technique.

## 1.5 Outline of Thesis

The thesis is organized as follows:

Chapter 2 explains theoretical background about FDTD method and the technique used to obtain RCS information from the simulation result. Also, related works are introduced.

Chapter 3 presents our code step by step to simulate electric and magnetic fields in a finite space and its interaction with a defined object.

In Chapter 4, the results for randomness in constitutive parameters are presented and Monte Carlo method is utilized to evaluate data. Imperfection in shape is examined in detail in this chapter. Also, the results for a secondary object simulation are provided in the rest of Chapter 4.

In Chapter 5, the summary of the thesis is given and future works are proposed.

## CHAPTER 2

### THEORETICAL BACKGROUND

This chapter has two main parts concentrating on the theoretical background of the thesis. The first part is about FDTD method and its specific form that is used in our simulation. The second part is about near to far field transformation. Surface Equivalence method is introduced since it is used to calculate the radar cross section.

#### 2.1 Fundamentals of Finite Difference Time Domain Method

FDTD method was first introduced by Yee in his paper about numerical transformations of Maxwell's equations [12]. This method was named as "FDTD" by Allen Taflove in 1980 [13]. All Maxwell's equations are transformed into their finite difference counter parts. Time dependent Maxwell's equations and constitutive equations in an isotropic and source free medium are as follows:

$$\nabla \times \mathbf{E} = -\frac{\partial \mathbf{B}}{\partial t} - \mathbf{M} \quad (2.1)$$

$$\nabla \times \mathbf{H} = \frac{\partial \mathbf{D}}{\partial t} - \mathbf{J} \quad (2.2)$$

$$\nabla \cdot \mathbf{D} = 0 \quad (2.3)$$

$$\nabla \cdot \mathbf{B} = 0 \quad (2.4)$$

$$\mathbf{D} = \epsilon \mathbf{E} \quad (2.5)$$

$$\mathbf{B} = \mu \mathbf{H} \quad (2.6)$$

where  $\mu$  and  $\epsilon$  are permeability (henrys/meter) and permittivity (farads/meter),  $\mathbf{J}$ : electric current density (amperes/meter<sup>2</sup>) and  $\mathbf{M}$ : equivalent magnetic current density (volts/meter<sup>2</sup>) in the medium. Magnetic current source is not a physically-realizable source, but it is defined to make Maxwell's equations symmetric. The field and flux components are defined as below:

$\mathbf{E}$  : Electric field intensity (volts/meter)

$\mathbf{D}$  : Electric flux density (coulombs/meter<sup>2</sup>)

$\mathbf{H}$  : Magnetic field intensity (amperes/meter)

$\mathbf{B}$  : Magnetic flux density (webers/meter<sup>2</sup>)

The current source could be decomposed into two parts [14]:

$$\mathbf{J} = \mathbf{J}_{source} + \sigma \mathbf{E} \quad (2.7)$$

$$\mathbf{M} = \mathbf{M}_{source} + \sigma^* \mathbf{H} \quad (2.8)$$

Where  $\sigma$  is electric conductivity (siemens/meter) and  $\sigma^*$  is equivalent magnetic loss (ohms/meter).  $\mathbf{J}_{\text{source}}$  and  $\mathbf{M}_{\text{source}}$  are independent sources. The two wave equations could be driven from Maxwell's equations as follows:

$$\frac{\partial \mathbf{H}}{\partial t} = -\frac{1}{\mu} \nabla \times \mathbf{E} - \frac{1}{\mu} (\mathbf{M}_{\text{source}} + \sigma^* \mathbf{H}) \quad (2.9)$$

$$\frac{\partial \mathbf{E}}{\partial t} = \frac{1}{\epsilon} \nabla \times \mathbf{H} - \frac{1}{\epsilon} (\mathbf{J}_{\text{source}} + \sigma \mathbf{E}) \quad (2.10)$$

If these equations are expressed in three dimensional Cartesian coordinates, they could be written out in the following six set of equations.

$$\frac{\partial H_x}{\partial t} = \frac{1}{\mu} \left[ \frac{\partial E_y}{\partial z} - \frac{\partial E_z}{\partial y} - (M_{\text{source}_x} + \sigma^* H_x) \right] \quad (2.11)$$

$$\frac{\partial H_y}{\partial t} = \frac{1}{\mu} \left[ \frac{\partial E_z}{\partial x} - \frac{\partial E_x}{\partial z} - (M_{\text{source}_y} + \sigma^* H_y) \right] \quad (2.12)$$

$$\frac{\partial H_z}{\partial t} = \frac{1}{\mu} \left[ \frac{\partial E_x}{\partial y} - \frac{\partial E_y}{\partial x} - (M_{\text{source}_z} + \sigma^* H_z) \right] \quad (2.13)$$

$$\frac{\partial E_x}{\partial t} = \frac{1}{\epsilon} \left[ \frac{\partial H_z}{\partial y} - \frac{\partial H_y}{\partial z} - (J_{\text{source}_x} + \sigma E_x) \right] \quad (2.14)$$

$$\frac{\partial E_y}{\partial t} = \frac{1}{\epsilon} \left[ \frac{\partial H_x}{\partial z} - \frac{\partial H_z}{\partial x} - (J_{\text{source}_y} + \sigma E_y) \right] \quad (2.15)$$

$$\frac{\partial E_z}{\partial t} = \frac{1}{\epsilon} \left[ \frac{\partial H_y}{\partial x} - \frac{\partial H_x}{\partial y} - (J_{\text{source}_z} + \sigma E_z) \right] \quad (2.16)$$

For 2-D  $\text{TM}_z$  case, the equations in a rectangular coordinate system reduce to the following scalar equations.

$$\frac{\partial H_x}{\partial t} = \frac{1}{\mu} \left[ -\frac{\partial E_z}{\partial y} - (M_{\text{source}_x} + \sigma^* H_x) \right] \quad (2.17)$$

$$\frac{\partial H_y}{\partial t} = \frac{1}{\mu} \left[ \frac{\partial E_z}{\partial x} - (M_{\text{source}_y} + \sigma^* H_y) \right] \quad (2.18)$$

$$\frac{\partial E_z}{\partial t} = \frac{1}{\epsilon} \left[ \frac{\partial H_y}{\partial x} - \frac{\partial H_x}{\partial y} - (J_{\text{source}_z} + \sigma E_z) \right] \quad (2.19)$$

These equations are valid for linear, isotropic, nondispersive and lossy materials.

### 2.1.1 Discretization

The main idea behind the Finite Difference Time Domain method is the discretization of Maxwell's equations in time and space, such that it becomes convenient to simulate Maxwell's equations via computers. A set of finite difference equations for the equations given above could be defined with respect to a Yee Cell [7]. Yee places the components of  $\mathbf{E}$  and  $\mathbf{H}$  in a unit cell of the lattice as shown in Figure 2-1.

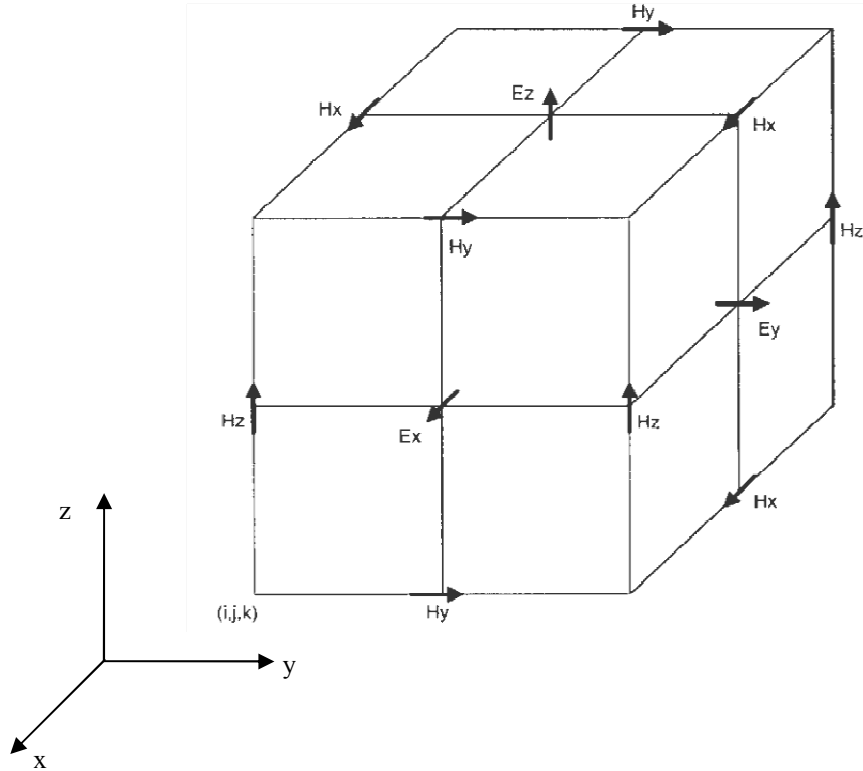


Figure 2-1 Representation of Electromagnetic Field Components in a Yee Cell in Rectangular Coordinate System

The components of electric and magnetic fields are evaluated at alternate half space, which is termed as a leap-frog arrangement. Firstly, all of the  $\mathbf{E}$  components are computed using formerly stored  $\mathbf{H}$  components in the modeled space and are stored in memory. Next, magnetic field components are calculated using the electric field values just computed, and this process is repeated periodically.

The space and time derivatives are central-difference in nature and second-order accurate. Yee's algorithm is a robust method and has advantages. The continuity of field components can easily be achieved, if the material defined in the simulation region is parallel to one of the space coordinates. Therefore, an efficient method could be implemented during putting different materials in a simulation space by only specifying the materials permittivity and permeability at each field location. After some manipulations, the curl equations can be converted to six scalar equations in finite-difference form. Defining the following coefficients will make our representation more convenient:

$$C_{a_{i,j,k}} = \frac{1 - \sigma_{i,j,k} \Delta t / 2\epsilon_{i,j,k}}{1 + \sigma_{i,j,k} \Delta t / 2\epsilon_{i,j,k}} \quad (2.20)$$

$$C_{b_{i,j,k}} = \frac{\Delta t / \epsilon_{i,j,k} \Delta_1}{1 + \sigma_{i,j,k} \Delta t / 2\epsilon_{i,j,k}} \quad (2.21)$$

$$C_{b_2 i,j,k} = \frac{\Delta_t / \varepsilon_{i,j,k} \Delta_2}{1 + \sigma_{i,j,k} \Delta_t / 2 \varepsilon_{i,j,k}} \quad (2.22)$$

$$D_{a i,j,k} = \frac{1 - \sigma_{i,j,k}^* \Delta_t / 2 \mu_{i,j,k}}{1 + \sigma_{i,j,k}^* \Delta_t / 2 \mu_{i,j,k}} \quad (2.23)$$

$$D_{b_1 i,j,k} = \frac{\Delta_t / \mu_{i,j,k} \Delta_1}{1 + \sigma_{i,j,k}^* \Delta_t / 2 \mu_{i,j,k}} \quad (2.24)$$

$$D_{b_2 i,j,k} = \frac{\Delta_t / \mu_{i,j,k} \Delta_2}{1 + \sigma_{i,j,k}^* \Delta_t / 2 \mu_{i,j,k}} \quad (2.25)$$

If the space increments ( $\Delta_1$  and  $\Delta_2$ ) are equal for three spatial dimensions, the second part of the coefficient becomes the same ( $C_b = C_{b_1} = C_{b_2}$  and  $D_b = D_{b_1} = D_{b_2}$ ), which characterizes two possible different lattice increments.  $\Delta_t$  denotes time increment. After introducing the coefficient, the six scalar equations in finite-difference form are given as:

$$E_{x, i, j + \frac{1}{2}, k + \frac{1}{2}}^{n + \frac{1}{2}} = C_{a, i, j + \frac{1}{2}, k + \frac{1}{2}} E_{x, i, j + \frac{1}{2}, k + \frac{1}{2}}^{n - \frac{1}{2}} + C_{b, i, j + \frac{1}{2}, k + \frac{1}{2}} (H_{z, i, j + 1, k + \frac{1}{2}}^n - H_{z, i, j, k + \frac{1}{2}}^n + H_{y, i, j + \frac{1}{2}, k}^n - H_{y, i, j + \frac{1}{2}, k + 1}^n - J_{x, i, j + \frac{1}{2}, k + \frac{1}{2}}^n \Delta) \quad (2.26)$$

$$E_{y, i - \frac{1}{2}, j + 1, k + \frac{1}{2}}^{n + \frac{1}{2}} = C_{a, i - \frac{1}{2}, j + 1, k + \frac{1}{2}} E_{y, i - \frac{1}{2}, j + 1, k + \frac{1}{2}}^{n - \frac{1}{2}} + C_{b, i - \frac{1}{2}, j + 1, k + \frac{1}{2}} (H_{x, i - \frac{1}{2}, j + 1, k + 1}^n - H_{x, i, j + 1, k}^n + H_{z, i - 1, j + 1, k + \frac{1}{2}}^n - H_{z, i, j + 1, k + \frac{1}{2}}^n - J_{y, i - \frac{1}{2}, j + 1, k + \frac{1}{2}}^n \Delta) \quad (2.27)$$

$$E_{z, i - \frac{1}{2}, j + \frac{1}{2}, k + 1}^{n + \frac{1}{2}} = C_{a, i - \frac{1}{2}, j + \frac{1}{2}, k + 1} E_{z, i - \frac{1}{2}, j + \frac{1}{2}, k + 1}^{n - \frac{1}{2}} + C_{b, i - \frac{1}{2}, j + \frac{1}{2}, k + 1} (H_{y, i, j + \frac{1}{2}, k + 1}^n - H_{y, i - 1, j + \frac{1}{2}, k + 1}^n + H_{x, i - \frac{1}{2}, j, k + 1}^n - H_{x, i - \frac{1}{2}, j + 1, k + 1}^n - J_{z, i - \frac{1}{2}, j + \frac{1}{2}, k + 1}^n \Delta) \quad (2.28)$$

$$H_{x, i - \frac{1}{2}, j + 1, k + 1}^{n + \frac{1}{2}} = D_{a, i - \frac{1}{2}, j + 1, k + 1} H_{x, i - \frac{1}{2}, j + 1, k + 1}^{n - \frac{1}{2}} + D_{b, i - \frac{1}{2}, j + 1, k + 1} (E_{y, i - \frac{1}{2}, j + 1, k + \frac{3}{2}}^n - E_{y, i - \frac{1}{2}, j + 1, k + \frac{1}{2}}^n + E_{z, i - \frac{1}{2}, j + \frac{1}{2}, k + 1}^n - E_{z, i - \frac{1}{2}, j + \frac{3}{2}, k + 1}^n - M_{x, i - \frac{1}{2}, j + 1, k + 1}^n \Delta) \quad (2.29)$$

$$\begin{aligned}
H_{y_{i,j+\frac{1}{2},k+1}}^{n+\frac{1}{2}} &= D_{a_{i,j+\frac{1}{2},k+1}} H_{y_{i,j+\frac{1}{2},k+1}}^{n-\frac{1}{2}} + D_{b_{i,j+\frac{1}{2},k+1}} (E_{z_{i+\frac{1}{2},j+\frac{1}{2},k+1}}^n \\
&\quad - E_{z_{i-\frac{1}{2},j+\frac{1}{2},k+1}}^n + E_{x_{i,j+\frac{1}{2},k+\frac{1}{2}}}^n - E_{x_{i,j+\frac{1}{2},k+\frac{3}{2}}}^n \\
&\quad - M_{y_{i,j+\frac{1}{2},k+1}}^n \Delta)
\end{aligned} \tag{2.30}$$

$$\begin{aligned}
H_{z_{i,j+1,k+\frac{1}{2}}}^{n+\frac{1}{2}} &= D_{a_{i,j+1,k+\frac{1}{2}}} H_{z_{i,j+1,k+\frac{1}{2}}}^{n-\frac{1}{2}} + D_{b_{i,j+1,k+\frac{1}{2}}} (E_{x_{i,j+\frac{3}{2},k+\frac{1}{2}}}^n \\
&\quad - E_{x_{i,j+\frac{1}{2},k+\frac{1}{2}}}^n + E_{y_{i-\frac{1}{2},j+1,k+\frac{1}{2}}}^n - E_{y_{i+\frac{1}{2},j+1,k+\frac{1}{2}}}^n \\
&\quad - M_{z_{i,j+1,k+\frac{1}{2}}}^n \Delta)
\end{aligned} \tag{2.31}$$

The finite – difference expressions for  $TM_z$  case are given as:

$$\begin{aligned}
E_{z_{i-\frac{1}{2},j+\frac{1}{2}}}^{n+\frac{1}{2}} &= C_{a_{i-\frac{1}{2},j+\frac{1}{2}}} E_{z_{i-\frac{1}{2},j+\frac{1}{2}}}^{n-\frac{1}{2}} + C_{b_{i-\frac{1}{2},j+\frac{1}{2}}} (H_{y_{i,j+\frac{1}{2}}}^n - H_{y_{i-1,j+\frac{1}{2}}}^n \\
&\quad + H_{x_{i-\frac{1}{2},j}}^n - H_{y_{i-\frac{1}{2},j+1}}^n - J_{z_{i-\frac{1}{2},j+\frac{1}{2}}}^n \Delta)
\end{aligned} \tag{2.32}$$

$$\begin{aligned}
H_{x_{i-\frac{1}{2},j+1}}^{n+1} &= D_{a_{i-\frac{1}{2},j+1}} H_{x_{i-\frac{1}{2},j+1}}^n + D_{b_{i-\frac{1}{2},j+1}} (E_{z_{i-\frac{1}{2},j+\frac{1}{2}}}^{n+\frac{1}{2}} - E_{z_{i-\frac{1}{2},j+\frac{3}{2}}}^{n+\frac{1}{2}} \\
&\quad - M_{x_{i-\frac{1}{2},j+1}}^{n+\frac{1}{2}} \Delta)
\end{aligned} \tag{2.33}$$

$$H_{y_{i,j+\frac{1}{2}}}^{n+1} = D_{a_{i,j+\frac{1}{2}}} H_{y_{i,j+\frac{1}{2}}}^n + D_{b_{i,j+\frac{1}{2}}} (E_{z_{i+\frac{1}{2},j+\frac{1}{2}}}^{n+\frac{1}{2}} - E_{z_{i-\frac{1}{2},j+\frac{1}{2}}}^{n+\frac{1}{2}} - M_{y_{i,j+\frac{1}{2}}}^{n+\frac{1}{2}} \Delta) \tag{2.34}$$

where the cell is assumed as square and  $\Delta$  denotes the space increments used for the finite differences.

Taflove and Brodwin obtained the correct criterion on numerical stability for Yee's algorithm and, solved the sinusoidal steady-state electromagnetic scattering problems in two- and three-dimensions in 1975. The derivation of the stability criterion is given in their paper. The stability of the time stepping algorithm [28] of the equation above is satisfied by the following criteria on  $\Delta_t$ :

$$\Delta_t \leq \frac{1}{v_{max} \sqrt{\Delta_x^2 + \Delta_y^2 + \Delta_z^2}} \tag{2.35}$$

In the equation,  $v_{max}$  denotes maximum phase velocity. And the space lattice increment ( $\Delta_x$ ,  $\Delta_y$ , and  $\Delta_z$ ) is generally taken as  $\lambda/20$  (1/20 of wavelength) to yield sufficient approximation and minimize finite difference error. It is stated that if the space increment is taken as  $\lambda/60$ , the stair case error (the error in modeling curved surfaces) is going to disappear. However, it can be guessed that decreasing space increment up to this level yields inefficiency.

The spatial arrangement of electric and magnetic fields nodes is shown in Figure 2-2 for a  $TM_z$  polarization wave. Electric and magnetic fields are plotted as circles and squares (with a line that indicates the orientation of the field component).

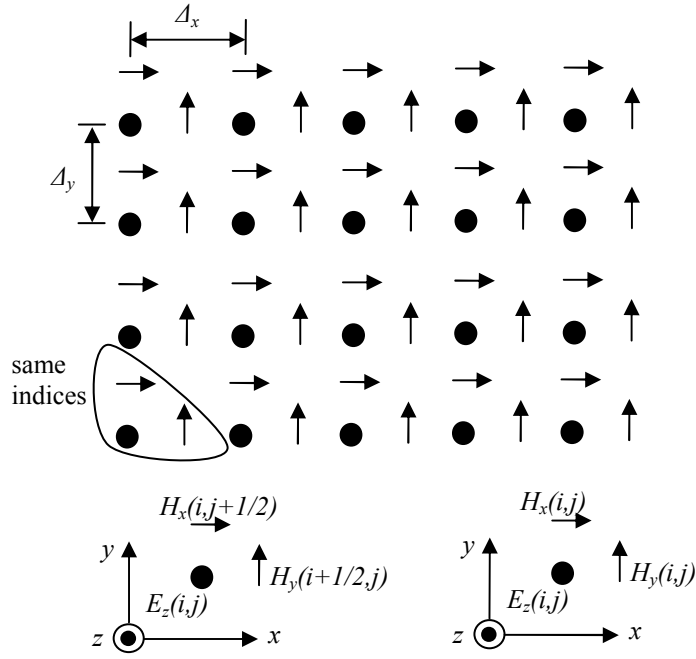


Figure 2-2 Orientation of Field Components

In this subsection, the main idea behind the FDTD algorithm was introduced and useful formulation techniques were given to develop a FDTD simulation. In scattering applications, the field extends to infinity and we have to restrict the wave simulation in a finite area/volume. To achieve this goal, the “Perfectly Matched Layer” concept is going to be introduced in the following subsection.

### 2.1.2 Perfectly Matched Layer (PML)

In this section, Perfectly Matched Layer approach and its implementations are going to be introduced. The main problem in the FDTD formulation is that the simulation region must be finite occupying an area/volume which must not be very large because of finite resources offered by computers. In electromagnetic scattering/radiation problems, the electromagnetic field must not be reflected from the outer boundary. We must take this point into consideration since the dissertation topic (i.e. RCS calculation) is that kind of problem. The simulation region cannot be excessively large or unbounded, therefore the outer boundary must be designed not to reflect the scattered field. Various methods have been introduced to achieve this purpose known as Absorbing Boundary Conditions (ABCs) [29]. PML is an efficient method to terminate simulation regions. Therefore the PML method is going to be introduced in this section.

Berenger proposed a new technique to terminate simulation regions in his papers [30-31], which is named as PML by him. This method is based on the use of an absorbing layer that is designed to absorb electromagnetic waves without reflection. Theoretically, the matched layer absorbs any kind of wave travelling towards the outer boundary without reflection. PML absorbing media has proven to be the most robust and efficient technique for the termination of FDTD lattices.

If we try to define perfectly matched layer for three dimensions, Maxwell’s equations will be our starting point to calculate the non-reflection conditions.

$$\epsilon \frac{\partial E_{xy}}{\partial t} + \sigma_y E_{xy} = \frac{\partial (H_{zx} + H_{zx})}{\partial y} \quad (2.36)$$

$$\epsilon \frac{\partial E_{xz}}{\partial t} + \sigma_z E_{xz} = -\frac{\partial(H_{yz} + H_{yx})}{\partial z} \quad (2.37)$$

$$\epsilon \frac{\partial E_{yz}}{\partial t} + \sigma_z E_{yz} = \frac{\partial(H_{xy} + H_{xz})}{\partial z} \quad (2.38)$$

$$\epsilon \frac{\partial E_{yx}}{\partial t} + \sigma_x E_{yx} = -\frac{\partial(H_{zx} + H_{zy})}{\partial x} \quad (2.39)$$

$$\epsilon \frac{\partial E_{zx}}{\partial t} + \sigma_x E_{zx} = \frac{\partial(H_{yz} + H_{yx})}{\partial x} \quad (2.40)$$

$$\epsilon \frac{\partial E_{zy}}{\partial t} + \sigma_y E_{zy} = -\frac{\partial(H_{xy} + H_{xz})}{\partial y} \quad (2.41)$$

$$\mu \frac{\partial H_{xy}}{\partial t} + \sigma_y^* H_{xy} = -\frac{\partial(E_{zx} + E_{zx})}{\partial y} \quad (2.42)$$

$$\mu \frac{\partial H_{xz}}{\partial t} + \sigma_z^* H_{xz} = \frac{\partial(E_{yz} + E_{yx})}{\partial z} \quad (2.43)$$

$$\mu \frac{\partial H_{yz}}{\partial t} + \sigma_z^* H_{yz} = -\frac{\partial(E_{xy} + E_{xz})}{\partial z} \quad (2.44)$$

$$\mu \frac{\partial H_{yx}}{\partial t} + \sigma_x^* H_{yx} = \frac{\partial(E_{zx} + E_{zy})}{\partial x} \quad (2.45)$$

$$\mu \frac{\partial H_{zx}}{\partial t} + \sigma_x^* H_{zx} = -\frac{\partial(E_{yz} + E_{yx})}{\partial x} \quad (2.46)$$

$$\mu \frac{\partial H_{zy}}{\partial t} + \sigma_y^* H_{zy} = \frac{\partial(E_{xy} + E_{xz})}{\partial y} \quad (2.47)$$

The PML technique will be explained on a  $TM_z$  wave equation. It is assumed that the computation region is vacuum. Therefore, the following condition must be satisfied to avoid the reflection of the incoming wave:

$$\frac{\sigma}{\epsilon_0} = \frac{\sigma^*}{\mu_0} \quad (2.48)$$

Where  $\epsilon_0$  is free space permittivity ( $8.854 \times 10^{-12}$  farads/meter) and  $\mu_0$  is free space permeability ( $4\pi \times 10^{-7}$  henrys/meter). The impedance of the wave is equal to the vacuum's impedance under this assumption and there is no reflection when plane wave propagates normally across a vacuum-medium interface. The main idea behind this method is that the  $E_z$  field is divided into two components (for  $TM_z$  case). The wave could be written in the following form:

$$\mu_2 \frac{\partial H_x}{\partial t} + \sigma_y^* H_x = -\frac{\partial E_z}{\partial y} \quad (2.49)$$

$$\mu_2 \frac{\partial H_y}{\partial t} + \sigma_x^* H_y = \frac{\partial E_z}{\partial x} \quad (2.50)$$

$$\epsilon_2 \frac{\partial E_{zx}}{\partial t} + \sigma_x E_{zx} = \frac{\partial H_y}{\partial x} \quad (2.51)$$

$$\epsilon_2 \frac{\partial E_{zy}}{\partial t} + \sigma_y E_{zy} = -\frac{\partial H_x}{\partial y} \quad (2.52)$$

where,  $E_z$  is split into two components;

$$E_z = E_{zx} + E_{zy} \quad (2.53)$$

The parameters  $\sigma_x$  and  $\sigma_y$  are electric conductivities, and the parameters  $\sigma_x^*$  and  $\sigma_y^*$  are magnetic losses.

If these sets of equations are analyzed, the results can be inferred from the equations. The equations define an absorbing medium, if “ $\sigma_x = \sigma_y$ ” and “ $\sigma_x^* = \sigma_y^*$ ”. Another inference is that if “ $\sigma_y = \sigma_y^* = 0$ ”, the medium could absorb a plane wave  $E_{zx}$  and  $H_y$  propagate along x, but not absorb a plane wave  $E_{zy}$  and  $H_x$  propagating along y. The same condition is valid for the contrary situation. The phasor form of the equation could be written as:

$$j\omega\mu_2 s_y^* H_x = -\frac{\partial(E_{zx} + E_{zy})}{\partial y} \quad (2.54)$$

$$j\omega\mu_2 s_x^* H_y = \frac{\partial(E_{zx} + E_{zy})}{\partial x} \quad (2.55)$$

$$j\omega\epsilon_2 s_x E_{zx} = \frac{\partial H_y}{\partial x} \quad (2.56)$$

$$j\omega\epsilon_2 s_y E_{zy} = -\frac{\partial H_x}{\partial y} \quad (2.57)$$

Where,  $s_w = (1 + \frac{\sigma_w}{j\omega\epsilon_2})$ ;  $s_w^* = (1 + \frac{\sigma_w^*}{j\omega\mu_2})$ ;  $w = x, y$ . After making necessary conversion, the wave equation and its plane wave solution could be given as:

$$\frac{1}{s_x} \frac{\partial}{\partial x} \frac{1}{s_x^*} \frac{\partial}{\partial x} E_z + \frac{1}{s_y} \frac{\partial}{\partial y} \frac{1}{s_y^*} \frac{\partial}{\partial y} E_z + \omega^2 \mu_2 \epsilon_2 E_z = 0 \quad (2.58)$$

$$E_z = E_0 \tau e^{-j\sqrt{s_x s_x^*} k_{2x} x - j\sqrt{s_y s_y^*} k_{2y} y} \quad (2.59)$$

Where  $\tau$  is transmission coefficient and  $k$  denotes wave number. The wave equation for a plane wave assumption is given [14]. The reflection could derived from the boundary condition applied at matched layer surface.

$$\Gamma = \left( \frac{k_{1x}}{w\mu_0} - \frac{k_{2x}}{w\mu_2} \sqrt{\frac{s_x}{s_x^*}} \right) \left( \frac{k_{1x}}{w\mu_0} + \frac{k_{2x}}{w\mu_2} \sqrt{\frac{s_x}{s_x^*}} \right)^{-1} \quad (2.60)$$

where  $\Gamma$  is reflection coefficient. If we assume that the following equalities are achieved ( $\epsilon_0 = \epsilon_2$ ,  $\mu_0 = \mu_2$ , and  $s_x = s_x^*$ ), the reflection coefficient becomes equal to zero. Therefore, no reflection occurs and the simulation region virtually extends to infinity. Berenger’s PML application on two dimensional spaces is shown in Figure 2-3.

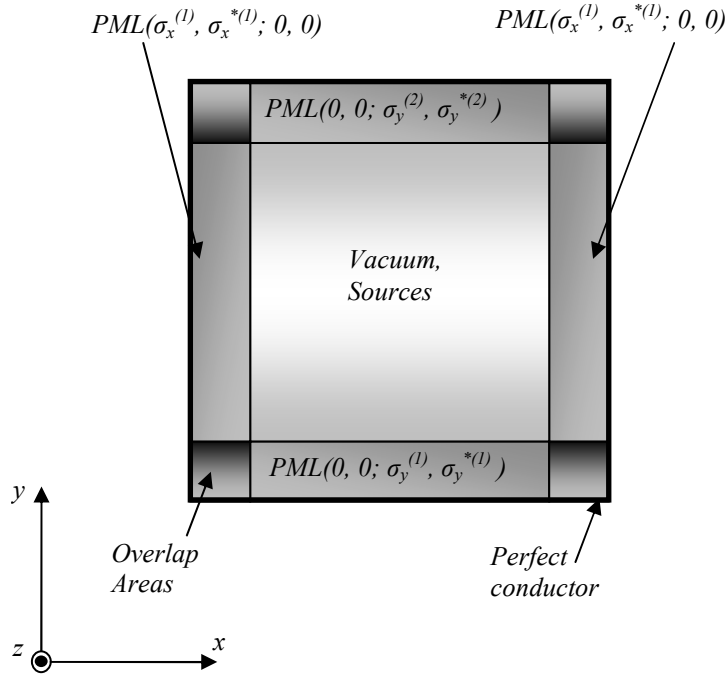


Figure 2-3 Berenger PML Technique

The method proposed by Berenger is a hypothetical assumption, and it is hard to implement. But in some works it is shown that a physical model could be applied [32] based on an anisotropic (uniaxial) medium.

### 2.1.2.1 Uniaxial Perfectly Matched Layer (UPML)

The technique is also known as Unsplit Perfectly Matched Layer (UPML) which combines the split fields of Berenger's PML by creating permittivity and permeability tensors for the PML layers [33]. The PML layer becomes physically realizable with a uniaxial material. Therefore, the electromagnetic fields no longer need to be split up. Sullivan also proposed an implementation method not to split the fields by using the electrical displacement to calculate the magnetic field instead of the electric field [34].

The UPML method is formulated as follows: First, it is assumed that the normal region is surrounded by a uniaxial anisotropic medium. Then, dispersion relation of the uniaxial medium is derived. The reflection coefficient on the interface is set to zero to make a reflection-free region on the boundary between PML and normal region. After that, it can be seen that reflectionless boundary condition occurs when the region is composed of a uniaxial medium. The permittivity and permeability tensors can be written:

$$\bar{\epsilon}_2 = \epsilon_0 \bar{s}; \quad \bar{\mu}_2 = \mu_0 \bar{s}; \quad \bar{s} = \begin{bmatrix} s_x^{-1} & 0 & 0 \\ 0 & s_x & 0 \\ 0 & 0 & s_x \end{bmatrix} \quad (2.61)$$

where  $s_x = 1 + \sigma_x / j\omega\epsilon_0$ ;

It can be seen from the tensors that the electromagnetic fields are not split, but the parameters between the electric field and the magnetic fields are frequency-dependent. Therefore, auxiliary

evaluations have to be made during implementation of FDTD for the field calculation. The equations for  $TM_z$  field could be given as:

$$\frac{\partial \bar{H}_y}{\partial x} - \frac{\partial \bar{H}_x}{\partial y} = j\omega \bar{D}_z \quad (2.62)$$

for;

$$\bar{D}_z = \epsilon s_y \bar{E}_z \quad (2.63)$$

The time domain representation is done via Inverse Fourier transform and its implementation to FDTD could be given;

$$D_z^{n+1} = \left( \frac{\epsilon}{\epsilon - \sigma_y \Delta t} \right) D_z^{n+1/2} + \left( \frac{\epsilon \Delta t}{\epsilon - \sigma_y \Delta t} \right) \left( \frac{H_{y_{i+1,j}}^{n+1/2} - H_{y_{i,j}}^{n+1/2}}{\Delta x} - \frac{H_{x_{i+1/2,j+1/2}}^{n+1/2} - H_{x_{i+1/2,j-1/2}}^{n+1/2}}{\Delta y} \right) \quad (2.64)$$

After derivation of electrical displacement, the electric field is implemented. Similar calculations are performed for the magnetic field and the magnetic flux density.

### 2.1.2.2 Convolutional Perfectly Matched Layer (CPML)

UPML is a useful method to define an ABC layer around the simulation region, but some auxiliary vectors are necessary to calculate the electromagnetic field. Another drawback of PML is that it is not efficient at absorbing evanescent waves [35], [36]. The problem is solved by placing the PML sufficiently far from obstacle which is put in the simulation region to eliminate the evanescent waves. This difficulty is solved by the complex frequency shifted (CFS) PML [37]. It is found that the CFS-PML proposed in [37] is an efficient method to eliminate evanescent waves, and reduces the size of the computational domain. CPML is based on a stretched coordinate formulation and a recursive convolution. The complex stretching variable is chosen as [37]:

$$s_i = \kappa_i + \frac{\sigma_i}{\alpha_i + j\omega\epsilon_0}, \quad i = x, y, z \quad (2.65)$$

Where  $\alpha_i$  is real and  $\kappa_i$  is real and  $\geq 1$ . We take  $(\bar{s}_i = s_i^{-1})$  the Inverse Fourier Transform of the complex stretching variable:

$$\bar{s}_i(t) = \frac{\delta(t)}{\kappa_i} - \frac{\sigma_i}{\epsilon_0 \kappa_i^2} e^{-\left(\frac{\sigma_i}{\epsilon_0 \kappa_i} \frac{\alpha_i}{\epsilon_0}\right)t} u(t) = \frac{\delta(t)}{\kappa_i} + \zeta_i(t) \quad (2.66)$$

Where  $\delta(t)$  is the impulse function and  $u(t)$  is the unit step function. The time dependent form of Ampere's law is written by the tensor in the time domain. As we know, multiplication in the frequency domain converts to convolution in the time domain. The discrete impulse response of the stretching variable could be given as:

$$\begin{aligned}
Z_{0_i}(m) &= \int_{m\Delta_t}^{(m+1)\Delta_t} \zeta_i(\tau) d\tau = -\frac{\sigma_i}{\epsilon_0 \kappa_i^2} \int_{m\Delta_t}^{(m+1)\Delta_t} e^{-\left(\frac{\sigma_i}{\epsilon_0 \kappa_i} - \frac{\alpha_i}{\epsilon_0}\right)\tau} d\tau \\
&= a_i e^{-\left(\frac{\sigma_i}{\kappa_i} + \alpha\right)\frac{m\Delta_t}{\epsilon_0}}
\end{aligned} \tag{2.67}$$

The multiplier is given as follows:

$$a_i = \frac{\sigma_i}{\sigma_i \kappa_i + \kappa_i^2 \alpha_i} \left( e^{-\left(\frac{\sigma_i}{\kappa_i} + \alpha\right)\frac{\Delta_t}{\epsilon_0}} - 1 \right) \tag{2.68}$$

From the function given above, the time domain form of Ampere's law and its discrete form could be written as follows:

$$\begin{aligned}
\epsilon_r \epsilon_0 \frac{\partial E_x}{\partial t} + \sigma E_x &= \frac{1}{\kappa_y} \frac{\partial H_z}{\partial y} - \frac{1}{\kappa_z} \frac{\partial H_x}{\partial z} + \zeta_y(t) * \frac{\partial H_z}{\partial y} - \zeta_z(t) * \frac{1}{\kappa_z} \frac{\partial H_x}{\partial z} \tag{2.69} \\
\epsilon_r \epsilon_0 \frac{E_x^{n+1} - E_x^n}{\Delta_t} + \sigma \frac{E_x^{n+1} + E_x^n}{2} &= \frac{H_z^{n+\frac{1}{2}} - H_z^{n-\frac{1}{2}}}{\kappa_y \Delta_y} - \frac{H_y^{n+\frac{1}{2}} - H_y^{n-\frac{1}{2}}}{\kappa_z \Delta_z} \\
&+ \sum_{m=0}^{N-1} Z_{0_y}(m) \frac{H_z^{n-m+\frac{1}{2}} - H_z^{n-m-\frac{1}{2}}}{\Delta_y} \\
&- \sum_{m=0}^{N-1} Z_{0_z}(m) \frac{H_y^{n-m+\frac{1}{2}} - H_y^{n-m-\frac{1}{2}}}{\Delta_z}
\end{aligned} \tag{2.70}$$

Where  $\epsilon_r$  is relative permittivity. Because of the simple exponential form of  $Z_{0_i}(m)$ , the following auxiliary function could be defined:

$$\psi_{exy, i+\frac{1}{2}, j, k}^{n+\frac{1}{2}} = e^{-\left(\frac{\sigma_i}{\kappa_i} + \alpha\right)\frac{\Delta_t}{\epsilon_0} n - \frac{1}{2}} + a_y \frac{\left( H_z^{n+\frac{1}{2}} - H_z^{n-\frac{1}{2}} \right)}{\Delta_y} \tag{2.71}$$

$$\psi_{exz, i+\frac{1}{2}, j, k}^{n+\frac{1}{2}} = e^{-\left(\frac{\sigma_i}{\kappa_i} + \alpha\right)\frac{\Delta_t}{\epsilon_0} n - \frac{1}{2}} + a_z \frac{\left( H_y^{n+\frac{1}{2}} - H_y^{n-\frac{1}{2}} \right)}{\Delta_z} \tag{2.72}$$

By this equation, the discrete form of Ampere's equation could be given:

$$\begin{aligned}
\epsilon_r \epsilon_0 \frac{E_x^{n+1} - E_x^n}{\Delta_t} + \sigma \frac{E_x^{n+1} + E_x^n}{2} &= \frac{H_z^{n+\frac{1}{2}} - H_z^{n-\frac{1}{2}}}{\kappa_y \Delta_y} - \frac{H_y^{n+\frac{1}{2}} - H_y^{n-\frac{1}{2}}}{\kappa_z \Delta_z} \\
&+ \psi_{exy, i+\frac{1}{2}, j, k}^{n+\frac{1}{2}} - \psi_{exz, i+\frac{1}{2}, j, k}^{n+\frac{1}{2}}
\end{aligned} \tag{2.73}$$

### 2.1.3 The Total-Field / Scattered-Field

Decomposing the simulation region into total and scattered field areas is an effective technique to calculate the RCS of an object. Eliminating the incident field also relieves the PML region, and it increases the dynamic range. The technique depends on the linearity of Maxwell's Equations so that the scattered and incident fields could be treated independently. The electric and magnetic fields are given as:

$$\mathbf{E}^t = \mathbf{E}^i + \mathbf{E}^s \quad (2.74)$$

$$\mathbf{H}^t = \mathbf{H}^i + \mathbf{H}^s \quad (2.75)$$

It is seen that if we know the incident field values the scattered field could be driven from the equations above. A simulation region for a 2D case is given at Figure 2-4.

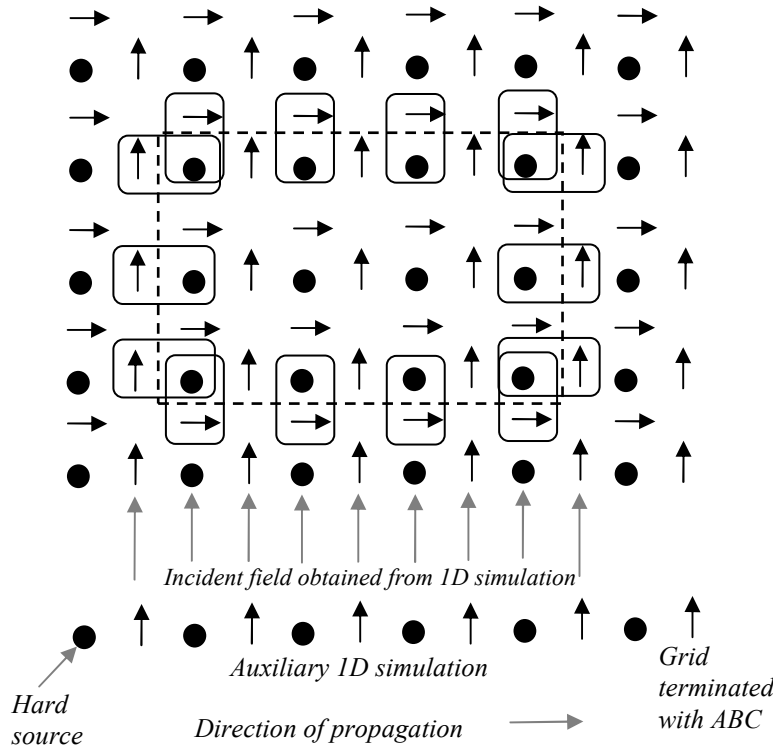


Figure 2-4 TF / SF Region for 2D Case

The FDTD method is applied normally to the simulation region, and at the scattered and total field boundary, some update equations must be added to the simulation. At the boundary, the incident field must be eliminated from the total field to obtain the scattered field [18].

Three equations at the boundary of total / scattered field for electric and magnetic fields must be modified for  $TM_z$  case.

The incident field at all points and at all time instants has to be known to write the equations. An auxiliary one dimensional wave equation is simulated besides the main simulation. Then the data found in the simulation is applied to the main FDTD simulation.

### 2.1.3.1 Plane Wave Excitation

A total field – scattered field application could only be defined by a plane wave excitation. The plane wave excitation is proposed by Yee in his most prominent paper [12]. According to Yee, the following equation must be in a code to define a plane wave (the electric and magnetic field values must be assigned at the same time):

$$E_z = \sin(2\pi ft) \quad (2.76)$$

$$H_y = \frac{1}{\eta} E_z \quad (2.77)$$

where  $\eta$  is the impedance of the medium. But as we stated above, an auxiliary 1D wave equation is simulated to separate TF / SF boundary. The equation could be used during defining the plane wave excitation to assign the electric and magnetic fields.

$$E_z^{i,n} = E^{i,n} \quad (2.78)$$

$$H_x^{i,n+\frac{1}{2}} = H^{i,n+\frac{1}{2}} \sin\phi \quad (2.79)$$

$$H_y^{i,n+\frac{1}{2}} = -H^{i,n+\frac{1}{2}} \cos\phi \quad (2.80)$$

where  $\phi$  is the angle between the wave direction and x – coordinate.

## 2.2 Near to Far Field Transformation

The near field data found by FDTD simulation has to be converted to far field for RCS calculation problems. The FDTD simulation region must be finite. The region could not be extended to infinity. The method is mostly used for the calculation of the electromagnetic field near a scatterer. However, some electromagnetic problems have to deal with the far field, for example RCS calculations, antenna problems, etc. Instead of increasing the extent of the simulation region, some methods are proposed to convert the near field data to far field. Up to now, several studies were done in this area. In the literature, two groups of methods are introduced, which are the frequency domain [25], [27], [38], [39] and time domain [40]-[43] transformation methods.

When we look at these two different methods; the main difference is that in the time domain method the near field waves are directly converted to far field in the time domain and far field data is transformed to the frequency domain. But in the frequency method the near field time domain data is converted to the frequency domain and the phasor is transformed to the far field.

### 2.2.1 Phasor Domain Technique

The frequency domain method is proposed by Taflove [25], [44]. Before introducing the method, we are going to explain two techniques to obtain sinusoidal steady state magnitude and phase information. The data can be obtained by directly programming a single frequency incident plane wave or taking the Discrete Fourier Transform of the pulse waveform response.

The first one is that the simulation region is excited by a sinusoidal wave and the data at a rectangular virtual surface surrounding a scatterer is obtained [45]. Before getting data we have to wait several wave periods to arrive at the steady state condition, and a staggering wave form must be applied to minimize error of short rise time. From the data we have to extract sinusoidal steady state magnitude and phase information. Firstly, the DC offset must be eliminated. After that the finite derivative of the wave over the virtual surface space is taken to find the phase values. The zero derivative points of the waveform are used to find the phase values of other part of wave form.

The second technique is that the data on the virtual surface are stored in memory with respect to time. Then, the Discrete Fourier Transform of the time data of each point is obtained to get sinusoidal steady state magnitude and phase information. A drawback of this technique is that the Fourier Transform of many lattice cell fields versus time wave forms would significantly add to the total requirements for computer storage and execution.

The main idea behind the transformation depends on Surface Equivalence Theorem [2] which is given in the Figure 2-5.

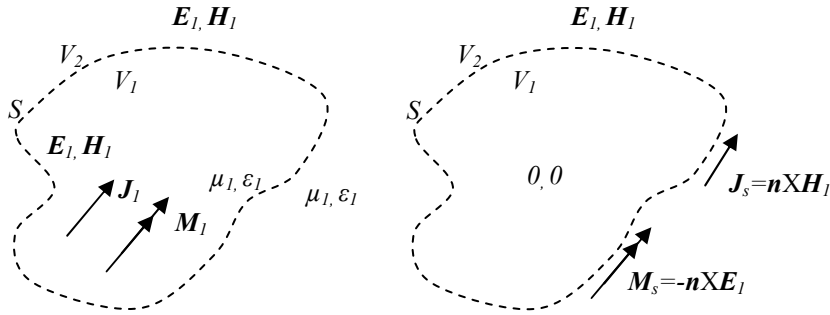


Figure 2-5 Surface Equivalence Theorem

This theorem proposes that the far field could be driven from the tangential electric and magnetic currents defined over a virtual surface surrounding the scatterer.

Surface equivalence theorem is suitable to calculate radar cross section of an object. The method is implemented in the following manner: First, an imaginary closed surface surrounding the scatterers is formed. The electromagnetic fields obey the boundary conditions on the surface. If the current density is chosen properly, the inside of the surface becomes field-free region and the fields at outside region are equal to the radiation produced by the actual source. This technique could be used to obtain the fields at the outside of the surface with the current density at the imaginary surface [30]. The technique needs integration of the current densities over the surface to calculate far field.

### 2.2.1.1 3-D Near to Far Field Transformation

The surface equivalent electric and magnetic currents ( $J_{Seq}$  and  $M_{Seq}$ ) are found from the scattered electric and magnetic fields and the following equations are used.

$$J_{Seq}(r) = \hat{n} \times H^s(r) \quad (2.81)$$

$$M_{Seq}(r) = -\hat{n} \times E^s(r) \quad (2.82)$$

In three dimensions the following procedure could be followed. The technique needs the phasor form of the field vectors and these are obtained by the Fourier transform of flowing time domain data. By Green's Theorem the far field is calculated. The Green's Function is given as:

$$G(\mathbf{r}, \mathbf{r}'_a) = \frac{e^{-jk_0|\mathbf{r}-\mathbf{r}'_a|}}{|\mathbf{r}-\mathbf{r}'_a|} \quad (2.83)$$

The formulation for the three dimensional case is presented below [14]. First, a pair of vector potentials are defined, as follows:

$$\mathbf{A} = \frac{\mu_0}{4\pi} \int_S \mathbf{J}_s \frac{e^{-jkR}}{R} ds' \cong \frac{\mu_0 e^{-jkr}}{4\pi r} \mathbf{N} \quad (2.84)$$

$$\mathbf{F} = \frac{\epsilon_0}{4\pi} \int_S \mathbf{M}_s \frac{e^{-jkR}}{R} ds' \cong \frac{\epsilon_0 e^{-jkC}}{4\pi r} \mathbf{L} \quad (2.85)$$

The  $\mathbf{N}$  and  $\mathbf{L}$  are defined to make the calculation easier.

$$\mathbf{N} = \int_S \mathbf{J}_s e^{jkr' \cos\psi} ds' \quad (2.86)$$

$$\mathbf{L} = \int_S \mathbf{M}_s e^{jkr' \cos\psi} ds' \quad (2.87)$$

Where:  $\mathbf{r} = r\hat{\mathbf{r}}$ ;  $\mathbf{r}' = r'\hat{\mathbf{r}}'$ ;  $\mathbf{R} = R\hat{\mathbf{R}} = \mathbf{r} - \mathbf{r}'$ ;  $\psi \equiv$  angle between  $\mathbf{r}$  and  $\mathbf{r}'$ .  $R$  is the distance between the source and observation point.

$$R = [r^2 + (r')^2 - 2rr' \cos\psi]^{1/2} \quad (2.88)$$

Two useful far field approximations are utilized to make calculation feasible. For phase variations;

$$R \cong r - r' \cos\psi \quad (2.89)$$

And for amplitude variations;

$$R \cong r \quad (2.90)$$

The electric and magnetic fields could be derived from the vector potentials and the relation is given by the following formulas:

$$\mathbf{E} = -j\omega \left[ \mathbf{A} + \frac{1}{k^2} \nabla(\nabla \cdot \mathbf{A}) \right] - \frac{1}{\epsilon_0} \nabla \times \mathbf{F} \quad (2.91)$$

$$\mathbf{H} = -j\omega \left[ \mathbf{F} + \frac{1}{k^2} \nabla(\nabla \cdot \mathbf{F}) \right] + \frac{1}{\mu_0} \nabla \times \mathbf{A} \quad (2.92)$$

The radial field components have negligible amplitude compared to  $\theta$  and  $\phi$  components because of the "1/r<sup>2</sup>" or higher terms in them. Simplifications could be applied to the equations above due to the fact that the far field approximations are concerned.

It is convenient to firstly calculate the vector phasor  $\mathbf{N}$  and  $\mathbf{L}$  for FDTD simulations. After that the far field and radar cross section are obtained from them. The  $\theta$  and  $\phi$  components are written as:

$$N_\theta = \iint_S (J_x \cos\theta \cos\phi + J_y \cos\theta \sin\phi - J_z \sin\theta) e^{jkr' \cos\psi} ds' \quad (2.93)$$

$$N_\phi = \iint_S (-J_x \sin\phi + J_y \cos\phi) e^{jkr' \cos\psi} ds' \quad (2.94)$$

$$L_\theta = \iint_S (M_x \cos\theta \cos\phi + M_y \cos\theta \sin\phi - M_z \sin\theta) e^{jkr' \cos\psi} ds' \quad (2.95)$$

$$L_\phi = \iint_S (-M_x \sin\phi + M_y \cos\phi) e^{jkr' \cos\psi} ds' \quad (2.96)$$

The equations could be implemented in the computer program to calculate the far field. The exponential phase term could be written as:

$$r' \cos\psi = \mathbf{r}' \cdot \hat{\mathbf{r}} = (x' \hat{\mathbf{x}} + y' \hat{\mathbf{y}} + z' \hat{\mathbf{z}})(\hat{\mathbf{x}} \sin\theta \cos\phi + \hat{\mathbf{y}} \sin\theta \sin\phi + \hat{\mathbf{z}} \cos\theta) = x' \sin\theta \cos\phi + y' \sin\theta \sin\phi + z' \cos\theta \quad (2.97)$$

The integral is taken over the imaginary rectangular box (six surfaces) and the current density is obtained from the phasor domain scattered field vectors which are given in Table 2-1.

Table 2-1 Principal Component Analysis

	$J_x$	$J_y$	$J_z$	$M_x$	$M_y$	$M_z$
-x (surface 1)	0	$H_z$	$-H_y$	0	$-E_z$	$E_y$
+x (surface 2)	0	$-H_z$	$H_y$	0	$E_z$	$-E_y$
-y (surface 3)	$-H_z$	0	$H_x$	$E_z$	0	$-E_x$
+y (surface 4)	$H_z$	0	$-H_x$	$-E_z$	0	$E_x$
-z (surface 5)	$H_y$	$-H_x$	0	$-E_y$	$E_x$	0
+z (surface 6)	$-H_y$	$H_x$	0	$E_y$	$-E_x$	0

The radar cross section is simply determined from the vector phasors given above. For a unit excitation the RCS is written as (having the dimension of square meters);

$$RCS(\theta, \phi) = \frac{k^2}{8\pi\eta_0} (|L_\phi + \eta_0 N_\theta|^2 + |L_\theta - \eta_0 N_\phi|^2) \quad (2.98)$$

where the intrinsic impedance of free space is  $\eta_0 = \sqrt{\frac{\mu_0}{\epsilon_0}}$ .

### 2.2.1.2 2-D $TM_z$ Near to Far Field Transformation

The theorem states that the equivalent surface currents produce the same scattered field in the exterior region of the boundary. The formulation also starts from the vector potential of the electric and magnetic fields to extract the far field for 2-D  $TM_z$  case (similar to the 3-D case).

After calculating the electric and magnetic vector potentials, the far field for a  $TM_z$  case is given by:

$$E_z^s = -j\omega\mu_0\psi_{z_{eq}} + jk_0(-F_{x_{eq}}\sin\phi + F_{y_{eq}}\cos\phi) \quad (2.99)$$

where;

$$\psi_{z_{eq}} \sim K \int_{S_a} J_{s_{eqz}}(x', y') e^{jk_0(x'\cos\phi + y'\sin\phi)} dl' \quad (2.100)$$

$$F_{x,y_{eq}} \sim K \int_{S_a} M_{s_{eqx,y}}(x', y') e^{jk_0(x'\cos\phi + y'\sin\phi)} dl' \quad (2.101)$$

and

$$K = \frac{e^{-jk_0\rho}}{\sqrt{8\pi k_0\rho}} e^{-j(3\pi/4)} \quad (2.102)$$

After the calculation given above, the RCS is evaluated as;

$$RCS = 2\pi\rho \left| \frac{E_z^s}{E^i} \right|^2 \quad (2.103)$$

Where  $\rho = \rho\hat{\rho}$  is the observation point in 2-D. RCS of an arbitrary shaped object could be simulated with the technique presented above.

### 2.2.2 Time Domain Technique

The method is derived in terms of the frequency domain transformation method which is introduced above. The far zone scattered electric field in phasor domain is expressed as follows:

$$E_\theta = -\eta W_\theta - U_\phi \quad (2.104)$$

$$E_\phi = -\eta W_\phi + U_\theta \quad (2.105)$$

Where;

$$\mathbf{W} = \frac{j e^{-jkR} \int_{S'} \mathbf{J} e^{-jkr' \cdot \hat{\mathbf{r}}} ds'}{2\lambda R} \quad (2.106)$$

$$\mathbf{U} = \frac{j e^{-jkR} \int_{S'} \mathbf{M} e^{-jkr' \cdot \hat{\mathbf{r}}} ds'}{2\lambda R} \quad (2.107)$$

where  $\lambda$  indicates wavelength. Now, to drive the time domain counter parts of  $\mathbf{W}$  and  $\mathbf{U}$ , the Inverse Fourier Transform is applied to  $\mathbf{W}$  and  $\mathbf{U}$  (phase difference in the frequency domain is equal to latency in the time domain):

$$\mathbf{w}(t) = \frac{1}{4\pi Rc} \frac{d}{dt} \left\{ \int_{S'} \mathbf{j}_s \left[ t + \frac{\mathbf{r}' \cdot \hat{\mathbf{r}}}{c} - \frac{R}{c} \right] ds' \right\} \quad (2.108)$$

$$\mathbf{u}(t) = \frac{1}{4\pi Rc} \frac{d}{dt} \left\{ \int_{S'} \mathbf{m}_s \left[ t + \frac{\mathbf{r}' \cdot \hat{\mathbf{r}}}{c} - \frac{R}{c} \right] ds' \right\} \quad (2.109)$$

Here,  $c$  ( $3 \times 10^8$  meters/second) denotes the velocity of light. In the function above, the time domain electric and magnetic currents are used to calculate  $\mathbf{W}$  and  $\mathbf{U}$ . The technique to obtain the electric and magnetic currents from the values of the scattered field is given above. After calculating the

special form of the radiation vector, the far electric fields could be obtained from the following equations:

$$e_{\theta} = -\eta w_{\theta} - u_{\phi} \quad (2.110)$$

$$e_{\phi} = -\eta w_{\phi} + u_{\theta} \quad (2.111)$$

## CHAPTER 3

### FDTD IMPLEMENTATION METHOD

In this chapter, the developed MATLAB codes are explained step by step. The technique basically depends on Taflove's method [25] on analyzing the scattered field of complex objects, which define the calculation of RCS of objects by FDTD method step by step. Also this method is explained precisely in Taflove's book [14].

In the paper [25], Taflove separates the simulation region into three parts; the total field region, the scattered field region and finally PML region. The schematic representation of this approach could be seen in Figure 3-1 which depicts 2-D case because of being simple to represent and explain.

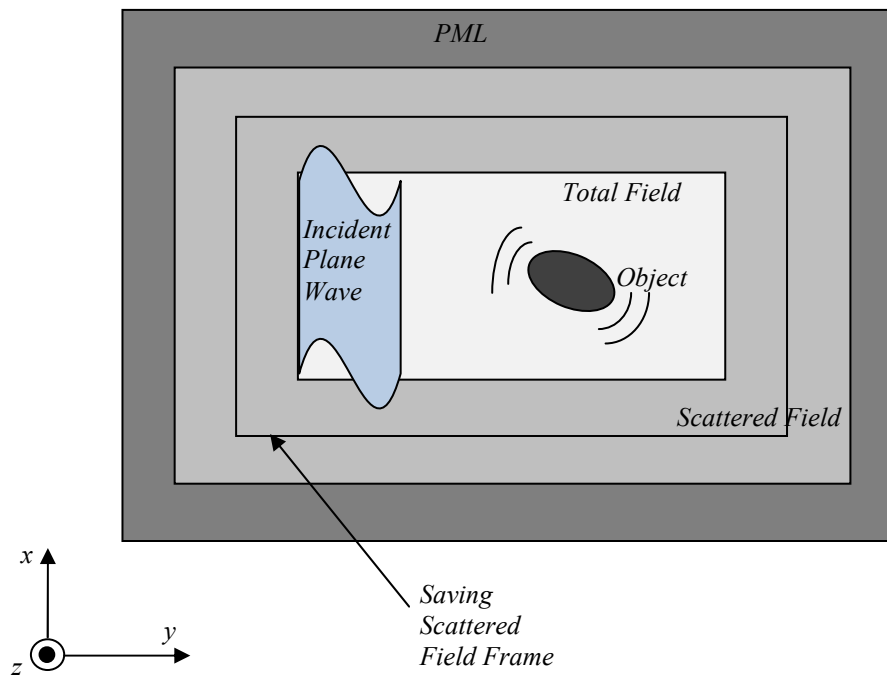


Figure 3-1 Representation of Simulation Area

The first region (the total field region) is the basic simulation area, in which the incident field ( $\mathbf{E}^i$ ,  $\mathbf{H}^i$ ) and the scattered ( $\mathbf{E}^s$ ,  $\mathbf{H}^s$ ) can be observed simultaneously [47]. There is no need to define a boundary condition on the interface between the object and the total field area, because implementation of curl equation in FDTD gives proper results. This region is excited by a  $\text{TM}_z$  plane wave in our 2-D study. After that, the three dimensional case will be put into practice to extend the study to more realistic objects.

As can be seen, the scattered field region is separated from the total field region by a rectangular surface performing the duty of connecting these two regions. The total and scattered field could be implemented by adding and subtracting the incident field at the rectangular surface.

The second region is known as the scattered field region which has only scattered electric and magnetic field components ( $\mathbf{E}^s, \mathbf{H}^s$ ). After gathering the scattered field values, the far scattered field is obtained directly from the near field values by surface equivalence theorems (Huygens' Theorem). There are only scattered electromagnetic field values in the second region because of making the transformation easier. The near field equivalent current computed via scattered field is then transformed to derive the Radar Cross Section (RCS). Another cause of separating the scattered field is that the PML region becomes more effective in absorbing the electromagnetic field.

The third region is Perfectly Matched Layer to absorb the electromagnetic field. Implementing the PML region serves to simulate the extension to infinity. Theoretical boundless space extension could be carried out by the PML region.

We are going to explain the following steps to fully understand the developed MATLAB codes and their applications.

### 3.1 Main Implementation Steps

Sullivan has proposed an efficient method, such that that the electric field is not directly obtained from the magnetic field to implement Unsplit Perfectly Matched Layer in the implementation of FDTD. Firstly, the electric displacement is calculated from the magnetic field, and after that the electric field is acquired from the electric flux density [18], [46].

#### 3.1.1 The FDTD Wave Implementation (TM<sub>z</sub> 2-D and 3-D)

Sullivan uses the normalized electric field and electric flux density to bring the electric and magnetic fields values on the same order of magnitude. This offers us a simpler implementation of FDTD. The electric field and electric displacement are converted into the normalized forms and the later formulas are created on the normalized values. Normalization is achieved by the following changes [48]:

$$\tilde{\mathbf{E}} = \sqrt{\frac{\epsilon_0}{\mu_0}} \mathbf{E} \quad (3.1)$$

$$\tilde{\mathbf{H}} = \sqrt{\frac{1}{\epsilon_0 \mu_0}} \mathbf{H} \quad (3.2)$$

From the normalized values, Maxwell's equations for TM<sub>z</sub> could be written as:

$$\frac{\partial D_z}{\partial t} = \frac{1}{\sqrt{\epsilon_0 \mu_0}} \left( \frac{\partial H_y}{\partial x} - \frac{\partial H_x}{\partial y} \right) \quad (3.3)$$

$$D_z(\omega) = \epsilon_r^*(\omega) E_z(\omega) \quad (3.4)$$

$$\frac{\partial H_x}{\partial t} = -\frac{1}{\sqrt{\epsilon_0 \mu_0}} \frac{\partial E_z}{\partial y} \quad (3.5)$$

$$\frac{\partial H_y}{\partial t} = \frac{1}{\sqrt{\epsilon_0 \mu_0}} \frac{\partial E_z}{\partial x} \quad (3.6)$$

The second equation is written in the phasor domain to make a lossy dielectric implementation easily. The term  $\epsilon_r^*$  is written in the following form which defines the electric field and the electric displacement as:

$$\epsilon_r^*(\omega) = \epsilon_r + \frac{\sigma}{j\omega\epsilon_0} \quad (3.7)$$

$$D_z(\omega) = \epsilon_r E_z(\omega) + \frac{\sigma}{j\omega\epsilon_0} E_z(\omega) \quad (3.8)$$

Then, the equation is converted to the time domain and the discrete form could be written as:

$$\mathbf{D}(t) = \epsilon_r \mathbf{E}(t) + \frac{\sigma}{\epsilon_0} \int_0^t \mathbf{E}(t') dt' \quad (3.9)$$

After converting the equation to the time domain, the discrete form in time could easily be applied to the equation. The following finite difference equation is suitable to put into practice where  $t = n\Delta_t$ ;

$$\mathbf{D}^n = \epsilon_r \mathbf{E}^n + \frac{\sigma \Delta_t}{\epsilon_0} \sum_{i=0}^n \mathbf{E}^i \quad (3.10)$$

$$\mathbf{D}^n = \epsilon_r \mathbf{E}^n + \frac{\sigma \Delta_t}{\epsilon_0} \mathbf{E}^n + \frac{\sigma \Delta_t}{\epsilon_0} \sum_{i=0}^{n-1} \mathbf{E}^i \quad (3.11)$$

The electric field value is calculated from the equation above as follows;

$$\mathbf{E}^n = \frac{\mathbf{D}^n - \frac{\sigma \Delta_t}{\epsilon_0} \sum_{i=0}^{n-1} \mathbf{E}^i}{\epsilon_r + \frac{\sigma \Delta_t}{\epsilon_0}} \quad (3.12)$$

An extra vector is defined to make calculation proper and the electric field could be updated as:

$$\mathbf{I}^n = \frac{\sigma \Delta_t}{\epsilon_0} \sum_{i=0}^n \mathbf{E}^i \quad (3.13)$$

$$\mathbf{E}^n = \frac{\mathbf{D}^n - \mathbf{I}^{n-1}}{\epsilon_r + \frac{\sigma \Delta_t}{\epsilon_0}} \quad (3.14)$$

The space orientation of the electric and magnetic fields in 2-D case is given in Figure 3-2.

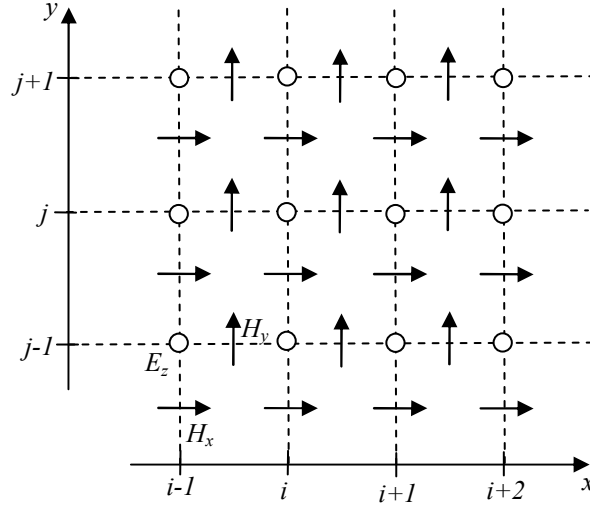


Figure 3-2 Space Settling of the Electric and Magnetic Field

The time increment is defined as  $\Delta_t = \frac{\Delta_x}{2c_0}$  to make multiplication factor 0.5. Now, with respect to Figure 3-2 the FDTD implementation could be given as follows;

$$dz[i][j] = dz[i][j] + 0.5 * (hy[i][j] - hy[i-1][j] - hx[i][j] + hx[i][j-1]) \quad (3.15)$$

$$ez[i][j] = gaz[i][j] * (dz[i][j] - iz[i][j]) \quad (3.16)$$

$$iz[i][j] = iz[i][j] + gbz[i][j] * ez[i][j] \quad (3.17)$$

$$hx[i][j] = hx[i][j] + 0.5 * (ez[i][j] - ez[i][j+1]) \quad (3.18)$$

$$hy[i][j] = hy[i][j] + 0.5 * (ez[i+1][j] - ez[i][j]) \quad (3.19)$$

Where;

$$gax[k] = \frac{1}{\epsilon_0 + (\frac{\sigma \Delta_t}{e_r})} \quad (3.20)$$

$$gbx[k] = \frac{\sigma \Delta_t}{e_r} \quad (3.21)$$

After obtaining the implementation of 2-D  $TM_z$  field, it is easy to develop a 3-D wave realization for the FDTD. Yee's paper [12] gives the details for 3-D situation. Here, the electric field is positioned 1/2 of cell width from the origin in the direction of its orientation, and the magnetic fields are placed 1/2 of cell width in each direction excluding that of its orientation. Perhaps, the 3-D implementation is thought as harder than the 2-D, however the same method is applied to the three dimensional simulations. The only difference is that all field vectors are used for all three dimensions, and it is a straightforward method. Again the normalized values of the electric field and electric displacement

are going to be used for simplicity without putting an extra notation to the  $E$  and  $D$ . In Figure 2-1, the space orientation of the electric and magnetic fields are defined.

The wave equations will be defined over the electric displacement to make PML implementation proper which is going to be introduced below. There are six equations to calculate all components in three dimensions.

After the finite difference approximation, it is easy to implement the three dimensional wave equation in the computer programs. The proper programmable format of the six equations is given below:

$$\begin{aligned} dx[i][j][k] &= dx[i][j][k] + 0.5 * (hz[i][j][k] \\ &- hz[i][j-1][k] - hy[i][j][k] \\ &+ hy[i][j][k-1]) \end{aligned} \quad (3.22)$$

$$\begin{aligned} dy[i][j][k] &= dy[i][j][k] + 0.5 * (hx[i][j][k] \\ &- hx[i][j][k-1] - hz[i][j][k] \\ &+ hz[i-1][j][k]) \end{aligned} \quad (3.23)$$

$$\begin{aligned} dz[i][j][k] &= dz[i][j][k] + 0.5 * (hy[i][j][k] \\ &- hy[i-1][j][k] - hx[i][j][k] \\ &+ hx[i][j-1][k]) \end{aligned} \quad (3.24)$$

$$\begin{aligned} hx[i][j][k] &= hx[i][j][k] + 0.5 * (ey[i][j][k+1] \\ &- ey[i][j][k] - ez[i][j+1][k] \\ &+ ez[i][j][k]) \end{aligned} \quad (3.25)$$

$$\begin{aligned} hy[i][j][k] &= hy[i][j][k] + 0.5 * (ez[i+1][j][k] \\ &- ez[i][j][k] - ex[i][j][k+1] \\ &+ ex[i][j][k]) \end{aligned} \quad (3.26)$$

$$\begin{aligned} hz[i][j][k] &= hz[i][j][k] + 0.5 * (ex[i][j+1][k] \\ &- ex[i][j][k] - ey[i+1][j][k] \\ &+ ey[i][j][k]) \end{aligned} \quad (3.27)$$

Maxwell's equations are written for the FDTD implementation by using these equations. The same format is suitable for one and two dimensional simulations. Only, the number of equations is increased in the three dimensional form.

The equations given above are for free space. For two-dimensional case, we introduced how it is converted. The same calculations are performed for three dimensional case as follows:

$$ex[i][j][k] = gax[i][j][k] * (dx[i][j][k] - ix[i][j][k]) \quad (3.28)$$

$$ix[i][j][k] = ix[i][j][k] + gbx[i][j][k] * ex[i][j][k] \quad (3.29)$$

$$ey[i][j][k] = gay[i][j][k] * (dy[i][j][k] - iy[i][j][k]) \quad (3.30)$$

$$iy[i][j][k] = iy[i][j][k] + gby[i][j][k] * ey[i][j][k] \quad (3.31)$$

$$ez[i][j][k] = gaz[i][j][k] * (dz[i][j][k] - iz[i][j][k]) \quad (3.32)$$

$$iz[i][j][k] = iz[i][j][k] + gbz[i][j][k] * ez[i][j][k] \quad (3.33)$$

The difference from the two dimensional case is that there are three electric field components. The “*ga* and *gb*” factors are the same as those given in the equations specified for the two dimensional case. Different types of materials are implemented by defining the conductance and the dielectric constant value for all cells in three dimensions.

### 3.1.2 The PML Implementation (TM<sub>z</sub> 2-D and 3-D)

The FDTD simulation must handle the difficulty that the fields extend to infinity for some types of problems. To accomplish this, an absorbing boundary condition is imposed at the boundary of simulation area. Therefore the wave does not reflect back to the simulation region, in this way the simulation area is virtually extended to infinity.

PML (Perfectly Matched Layer) method is proposed by Berenger [31] and it is mostly used to absorb the electromagnetic waves at the boundary. A matched layer (in which the wave is attenuated) is defined outside the simulation area. The reflection at the interface between the simulation region and matched layer must be eliminated. The amount of reflection is calculated by:

$$\Gamma = \frac{\eta_A - \eta_B}{\eta_A + \eta_B} \quad (3.34)$$

where the intrinsic impedance is written as:

$$\eta = \sqrt{\frac{\mu}{\epsilon}} \quad (3.35)$$

The field vectors are decomposed into two components in the method introduced by Berenger. Another method is introduced to make Berenger’s method more useable and easier to implement in the computer programs. Also, the method of Berenger is defined only as a mathematical explanation, and it has not a physical basis. Therefore Uniaxial PML method is defined to overcome the problems.

Sullivan proposes an implementation of PML method in his book [18] by avoiding the splitting of the field vectors. He used this method in his many works, and the efficiency of the method is proved in this way [34], [48], and [49]. Not surprisingly, one must start from Maxwell’s equations to explain Sullivan’s method. The wave equation in the matched layer is given by fictitious dielectric constants and permeability ( $\epsilon_{Fz}^*, \mu_{Fx}^*$ ) for 2-D TM<sub>z</sub> case as follows ( $\mathbf{D}$  and  $\mathbf{E}$  are normalized fields):

$$j\omega D_z \epsilon_{Fz}^*(x) \epsilon_{Fz}^*(y) = c_0 \left( \frac{\partial H_y}{\partial x} - \frac{\partial H_x}{\partial y} \right) \quad (3.36)$$

$$D_z(\omega) = \epsilon_r^*(\omega) E_z(\omega) \quad (3.37)$$

$$j\omega H_x \mu_{Fx}^*(x) \mu_{Fx}^*(y) = -c_0 \frac{\partial E_z}{\partial y} \quad (3.38)$$

$$j\omega H_y \mu_{Fy}^*(x) \mu_{Fy}^*(y) = c_0 \frac{\partial E_z}{\partial x} \quad (3.39)$$

There are two conditions to form a PML. The first one is that the intrinsic impedance of the matched layer must be equal to the intrinsic impedance of free space:

$$\eta_0 = \eta_m = \sqrt{\frac{\mu_{Fx}^*}{\epsilon_{Fz}^*}} = 1 \quad (3.40)$$

The equation above becomes equal to one because of the normalization. The relative dielectric constant and relative permeability must satisfy the following conditions:

$$\epsilon_{Fx}^* = \frac{1}{\epsilon_{Fy}^*} \quad (3.41)$$

$$\mu_{Fx}^* = \frac{1}{\mu_{Fy}^*} \quad (3.42)$$

These relative constants are given as follows:

$$\epsilon_{Fm}^* = \epsilon_{Fm} + \frac{\sigma_{Dm}}{j\omega\epsilon_0} \quad (3.43)$$

$$\mu_{Fm}^* = \mu_{Fm} + \frac{\sigma_{Hm}}{j\omega\mu_0} \quad (3.44)$$

For  $m = x$  or  $y$ .

The following selection of the parameters is suitable for satisfying the PML conditions:

$$\epsilon_{Fm} = \mu_{Fm} = 1 \quad (3.45)$$

$$\frac{\sigma_{Dm}}{\epsilon_0} = \frac{\sigma_{Hm}}{\mu_0} = \frac{\sigma_D}{\epsilon_0} \quad (3.46)$$

The method is explained below only for one direction and it will be extended to full form. The following equations must be preserved for "x" direction:

$$j\omega\left(1 + \frac{\sigma_D(x)}{j\omega\epsilon_0}\right)D_z = c_0\left(\frac{\partial H_y}{\partial x} - \frac{\partial H_x}{\partial y}\right) \quad (3.47)$$

$$j\omega\left(1 + \frac{\sigma_D(x)}{j\omega\epsilon_0}\right)^{-1}H_x = -c_0\frac{\partial E_z}{\partial y} \quad (3.48)$$

$$j\omega\left(1 + \frac{\sigma_D(x)}{j\omega\epsilon_0}\right)H_y = c_0\frac{\partial E_z}{\partial x} \quad (3.49)$$

Firstly we look at the first equation and the electric displacement is written as:

$$j\omega\left(1 + \frac{\sigma_D(x)}{j\omega\epsilon_0}\right)D_z = j\omega D_z + \frac{\sigma_D(x)}{\epsilon_0}D_z \quad (3.50)$$

This equation is converted into the finite difference form.

$$\begin{aligned} \frac{\partial D_z}{\partial t} + \frac{\sigma_D(x)}{\epsilon_0}D_z & \\ & \cong \frac{D_z^{n+\frac{1}{2}}(i,j) - D_z^{n-\frac{1}{2}}(i,j)}{\Delta t} \\ & + \frac{\sigma_D(x)D_z^{n+\frac{1}{2}}(i,j) + D_z^{n-\frac{1}{2}}(i,j)}{2\epsilon_0} \\ & = D_z^{n+\frac{1}{2}}(i,j)\frac{1}{\Delta t}\left[1 + \frac{\sigma_D(i)\Delta t}{2\epsilon_0}\right] \\ & - D_z^{n-\frac{1}{2}}(i,j)\frac{1}{\Delta t}\left[1 - \frac{\sigma_D(i)\Delta t}{2\epsilon_0}\right] \end{aligned} \quad (3.51)$$

Now, we substitute this into the equation:

$$\begin{aligned}
D_z^{n+\frac{1}{2}}(i,j) &= gi3(i)D_z^{n-\frac{1}{2}}(i,j) \\
&+ gi2(i)0.5[H_y^n\left(i+\frac{1}{2},j\right) \\
&- H_y^n\left(i-\frac{1}{2},j\right) - H_x^n\left(i,j+\frac{1}{2}\right) \\
&+ H_x^n\left(i,j-\frac{1}{2}\right)]
\end{aligned} \tag{3.52}$$

where we have used the relation  $\frac{\Delta_t}{\Delta_x}c_0 = \frac{1}{2}$ . The parameters gi2 and gi3 are as follows;

$$gi2(i) = \frac{1}{1 + \frac{\sigma_D(i)\Delta_t}{2\epsilon_0}} \tag{3.53}$$

$$gi3(i) = \frac{1 - \frac{\sigma_D(i)\Delta_t}{2\epsilon_0}}{1 + \frac{\sigma_D(i)\Delta_t}{2\epsilon_0}} \tag{3.54}$$

The same steps are traced for the third equation:

$$\begin{aligned}
H_y^{n+1}\left(i+\frac{1}{2},j\right) &= fi3\left(i+\frac{1}{2}\right)H_y^n\left(i+\frac{1}{2},j\right) \\
&+ fi2\left(i+\frac{1}{2}\right)0.5[E_z^{n+\frac{1}{2}}(i+1,j) \\
&- E_z^{n+\frac{1}{2}}(i,j)]
\end{aligned} \tag{3.55}$$

And the parameters are given as:

$$fi2\left(i+\frac{1}{2}\right) = \frac{1}{1 + \frac{\sigma_D\left(i+\frac{1}{2}\right)\Delta_t}{2\epsilon_0}} \tag{3.56}$$

$$fi3\left(i+\frac{1}{2}\right) = \frac{1 - \frac{\sigma_D\left(i+\frac{1}{2}\right)\Delta_t}{2\epsilon_0}}{1 + \frac{\sigma_D\left(i+\frac{1}{2}\right)\Delta_t}{2\epsilon_0}} \tag{3.57}$$

However the second equation needs a different treatment. The equation is rewritten as:

$$j\omega H_x = -c_0\left[\frac{\partial E_z}{\partial y} + \frac{\sigma_D(x)}{\epsilon_0} \frac{1}{j\omega} \frac{\partial E_z}{\partial y}\right] \tag{3.58}$$

The finite difference implementation is given as:

$$\begin{aligned}
&\frac{H_z^{n+1}\left(i,j+\frac{1}{2}\right) - H_z^n\left(i,j+\frac{1}{2}\right)}{\Delta_t} \\
&= -c_0\left[-\frac{curl\_e}{\Delta_x} - \frac{\sigma_D(x)}{\epsilon_0} \Delta_t \sum_{n=0}^T \frac{curl\_e}{\Delta_x}\right]
\end{aligned} \tag{3.59}$$

where  $curl\_e$  is defined as:

$$curl\_e = E_z^{n+\frac{1}{2}}(i,j) - E_z^{n+\frac{1}{2}}(i,j+1) \tag{3.60}$$

Finally, the equation could be written as:

$$I_{H_x}^{n+\frac{1}{2}}\left(i, j + \frac{1}{2}\right) = I_{H_x}^{n-\frac{1}{2}}\left(i, j + \frac{1}{2}\right) + \text{curl}_e \quad (3.61)$$

$$fi1(i) = \frac{\sigma(i)\Delta_t}{2\epsilon_0} \quad (3.62)$$

$$\begin{aligned} H_x^{n+1}\left(i, j + \frac{1}{2}\right) \\ = H_x^n\left(i, j + \frac{1}{2}\right) + 0.5\text{curl}_e \\ + fi1(i)I_{H_x}^{n+\frac{1}{2}}\left(i, j + \frac{1}{2}\right) \end{aligned} \quad (3.63)$$

The f and g parameters are set to an optimum value with the experimental data by Sullivan. The parameters are defined by an auxiliary parameter.

$$xn = \frac{\sigma\Delta_t}{2\epsilon_0} \quad (3.64)$$

$$xn(i) = 0.333\left(\frac{i}{\text{length\_pml}}\right)^3 \quad (3.65)$$

$$fi1(i) = xn(i) \quad (3.66)$$

$$gi2(i) = \left(\frac{1}{1 + xn(i)}\right) \quad (3.67)$$

$$gi3(i) = \left(\frac{1 - xn(i)}{1 + xn(i)}\right) \quad (3.68)$$

The PML is implemented in the x direction. Therefore we have to extend this to the y direction. The full equation is written as:

$$j\omega\left(1 + \frac{\sigma_D(x)}{j\omega\epsilon_0}\right)\left(1 + \frac{\sigma_D(y)}{j\omega\epsilon_0}\right)D_z = c_0\left(\frac{\partial H_y}{\partial x} - \frac{\partial H_x}{\partial y}\right) \quad (3.69)$$

$$j\omega\left(1 + \frac{\sigma_D(x)}{j\omega\epsilon_0}\right)^{-1}\left(1 + \frac{\sigma_D(y)}{j\omega\epsilon_0}\right)H_x = -c_0\frac{\partial E_z}{\partial y} \quad (3.70)$$

$$j\omega\left(1 + \frac{\sigma_D(x)}{j\omega\epsilon_0}\right)\left(1 + \frac{\sigma_D(y)}{j\omega\epsilon_0}\right)^{-1}H_y = c_0\frac{\partial E_z}{\partial x} \quad (3.71)$$

The same procedure which is implemented for only the x direction is used and the finite difference form is evaluated as:

$$\begin{aligned} D_z^{n+\frac{1}{2}}(i, j) \\ = gi3(i)gj3(j)D_z^{n-\frac{1}{2}}(i, j) \\ + gi2(i)gj2(j)0.5[H_y^n\left(i + \frac{1}{2}, j\right) \\ - H_y^n\left(i - \frac{1}{2}, j\right) - H_x^n\left(i, j + \frac{1}{2}\right) + H_x^n\left(i, j - \frac{1}{2}\right)] \end{aligned} \quad (3.72)$$

The  $H_x$  and  $H_y$  are expressed as follows:

$H_y$ :

$$\text{curl}_e = E_z^{n+\frac{1}{2}}(i+1, j) - E_z^{n+\frac{1}{2}}(i, j) \quad (3.73)$$

$$I_{H_y}^{n+\frac{1}{2}}\left(i + \frac{1}{2}, j\right) = I_{H_y}^{n-\frac{1}{2}}\left(i + \frac{1}{2}, j\right) + \text{curl}_e \quad (3.74)$$

$$\begin{aligned} H_y^{n+1}\left(i + \frac{1}{2}, j\right) \\ = fj3\left(i + \frac{1}{2}\right)H_y^n\left(i + \frac{1}{2}, j\right) - fi2\left(i + \frac{1}{2}\right)0.5\text{curl}_e + fj1(j)I_{H_y}^{n+\frac{1}{2}}\left(i + \frac{1}{2}, j\right) \end{aligned} \quad (3.75)$$

$H_x$ :

$$\text{curl}_e = E_z^{n+\frac{1}{2}}(i, j) - E_z^{n+\frac{1}{2}}(i, j+1) \quad (3.76)$$

$$I_{H_x}^{n+\frac{1}{2}}\left(i, j + \frac{1}{2}\right) = I_{H_x}^{n-\frac{1}{2}}\left(i, j + \frac{1}{2}\right) + \text{curl}_e \quad (3.77)$$

$$\begin{aligned} H_x^{n+1}\left(i, j + \frac{1}{2}\right) \\ = fj3\left(j + \frac{1}{2}\right)H_x^n\left(i, j + \frac{1}{2}\right) - fj2(j)0.5\text{curl}_e + fi1(i)I_{H_x}^{n+\frac{1}{2}}\left(i, j + \frac{1}{2}\right) \end{aligned} \quad (3.78)$$

There is a seamless transition between the main part and the matched layer part by setting  $fi1$  and  $fj1$  to zero and the other parameters to one. In the Figure 3-3, the definition of the simulation area is depicted.

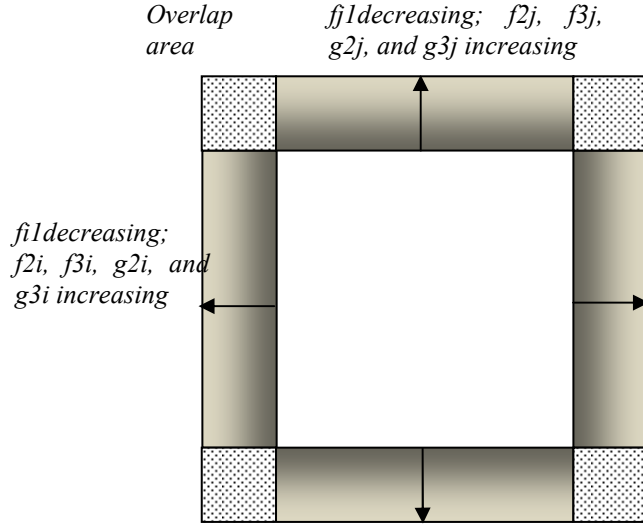


Figure 3-3 PML Implementation

Developing a three-dimensional PML directly follows the two-dimensional one. In two-dimensional case, we only deal with “x” and “y” directions. In addition to this, the “z” direction is imported to extend PML implementation to the three-dimension.  $D_z$  could be written as to develop a 3-D PML:

$$j\omega\left(1 + \frac{\sigma_D(x)}{j\omega\epsilon_0}\right)\left(1 + \frac{\sigma_D(y)}{j\omega\epsilon_0}\right)\left(1 + \frac{\sigma_D(z)}{j\omega\epsilon_0}\right)^{-1}D_z = c_0\left(\frac{\partial H_y}{\partial x} - \frac{\partial H_x}{\partial y}\right) \quad (3.79)$$

The equation could be written as the following form.

$$j\omega\left(1 + \frac{\sigma_D(x)}{j\omega\epsilon_0}\right)\left(1 + \frac{\sigma_D(y)}{j\omega\epsilon_0}\right)D_z = c_0\left(1 + \frac{\sigma_D(z)}{j\omega\epsilon_0}\right)\left(\frac{\partial H_y}{\partial x} - \frac{\partial H_x}{\partial y}\right) = c_0 \text{curl}_h + c_0 \frac{\sigma_z(z)}{\epsilon_0} \frac{1}{j\omega} \text{curl}_h \quad (3.80)$$

The last part will define:

$$I_{Dz} = \frac{1}{j\omega} \text{curl}_h \quad (3.81)$$

The phasor domain representation is transformed into the time domain. It could be seen that the left side of the equation is the same with 2-D implementation. The right side is slightly different, and it contains integration in the time domain.

$$\begin{aligned} \text{curl}_h = & [H_y^n \left( i + \frac{1}{2}, j, k + \frac{1}{2} \right) - H_y^n \left( i - \frac{1}{2}, j, k + \frac{1}{2} \right) \\ & - H_x^n \left( i, j + \frac{1}{2}, k + \frac{1}{2} \right) \\ & + H_x^n \left( i, j - \frac{1}{2}, k + \frac{1}{2} \right)] \end{aligned} \quad (3.82)$$

$$I_{Dz}^n \left( i, j, k + \frac{1}{2} \right) = I_{Dz}^{n-1} \left( i, j, k + \frac{1}{2} \right) + \text{curl}_h \quad (3.83)$$

$$\begin{aligned} D_z^{n+\frac{1}{2}} \left( i, j, k + \frac{1}{2} \right) \\ = & gi3(i)gj3(j)D_z^{n-\frac{1}{2}} \left( i, j, k + \frac{1}{2} \right) \\ & + gi2(i)gj2(j)0.5(\text{curl}_h \\ & + gk1(k)I_{Dz}^n \left( i, j, k + \frac{1}{2} \right)) \end{aligned} \quad (3.84)$$

The “g” parameters are the same as those given for the two dimensional case. As can be seen, the integral parameter is an additional three-dimensional array  $I_{Dz}$  which is also needed for all of the field vectors (six field vectors for the three-dimensional case) and it occupies an important part of the computer memory and is a waste of computer resources. Therefore the array is broken up into two smaller three-dimensional arrays which are at the lower and upper part of “z” direction for  $D_z$  given above. And the main part of the simulation becomes easier to calculate. The equation for upper and lower part of the simulation turns into;

$$\text{curl}_h = (hy[i][j][k] - hy[i-1][j][k] - hx[i][j][k] + hx[i][j-1][k]) \quad (3.85)$$

$$idzl[i][j][k] = idzl[i][j][k] + \text{curl}_h \quad (3.86)$$

$$\begin{aligned} dz[i][j][k] \\ = & gi3[i] * gj3[j] * dz[i][j][k] + gi2[i] \\ & * gj2[j] * 0.5 * (\text{curl}_h + gk1[k] \\ & * idzl[i][j][k]) \end{aligned} \quad (3.87)$$

The equation at the main part of the simulation region, which is the middle part of the area, becomes:

$$\begin{aligned} dz[i][j][k] \\ = & gi3[i] * gj3[j] * dz[i][j][k] + gi2[i] \\ & * gj2[j] * 0.5 * \text{curl}_h \end{aligned} \quad (3.88)$$

The normal FDTD simulation is only run at this part.

### 3.1.3 Total / Scattered Field Boundary Implementation (TM<sub>z</sub> 2-D and 3-D)

The total / scattered field must be separated in some problems, if for example only the scattered field vectors are needed to calculate far field values and radar cross sections. Therefore scattered field vectors have to be obtained to calculate these parameters. A plane wave excitation is possible and the simulation of plane wave is employed in many problems.

Eliminating the incident field part relieves the PML because of the difficulty in providing the perfect absorption. Sullivan uses an auxiliary one-dimensional wave simulation to obtain incident field values at any point and at any time instant. The incident field part is eliminated from the total field. The simulation region of this implementation for 2-D TM<sub>z</sub> is shown in Figure 3-4.

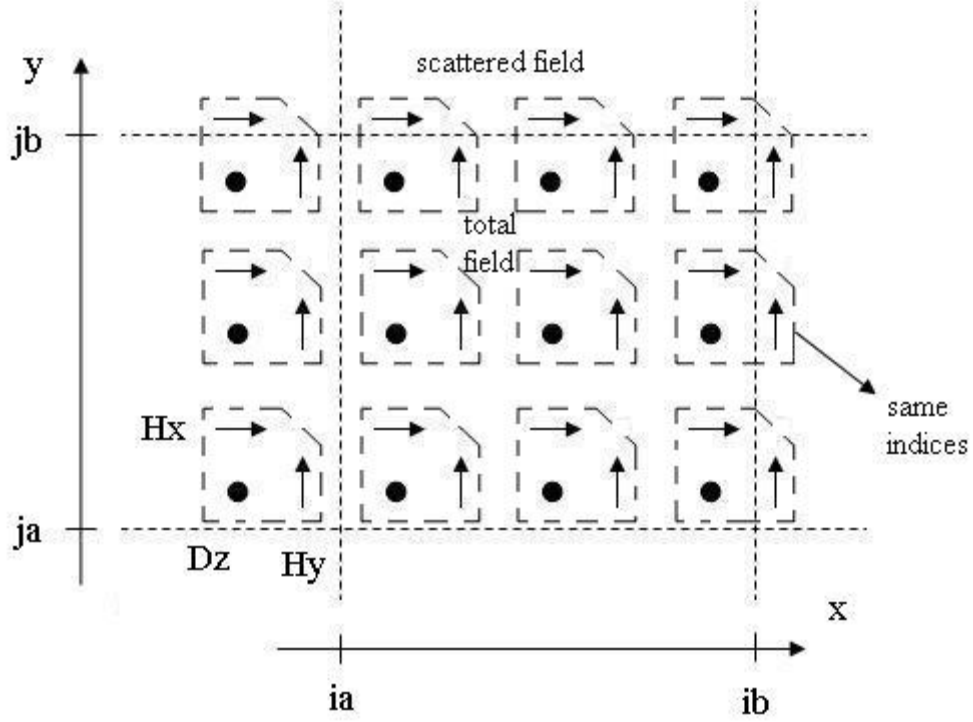


Figure 3-4 Orientation of Field Vectors at the Boundary for 2-D  $TM_z$

Implementing the interface conditions on the total / scattered field boundary is not difficult. Normal FDTD simulation is implemented and at the boundary the field values must be modified. The total field is the sum of the incident and scattered fields.

When a total field value at the boundary uses the reflected field, it is needed to add the incident field at that point during the simulation. The following modifications must be made for a two dimensional  $TM_z$  case with respect to Figure 3-4:

The first one  $D_z$  at  $j = j_a$  and  $j = j_b$ :

$$D_z(i, j_a) = D_z(i, j_a) + 0.5H_{x_{inc}}(j_a - \frac{1}{2}) \quad (3.89)$$

$$D_z(i, j_b) = D_z(i, j_b) - 0.5H_{x_{inc}}(j_b + \frac{1}{2}) \quad (3.90)$$

The second one  $H_x$  at just outside  $j = j_a$  and  $j = j_b$ :

$$H_x(i, j_a - \frac{1}{2}) = H_x(i, j_a - \frac{1}{2}) + 0.5E_{z_{inc}}(j_a) \quad (3.91)$$

$$H_x(i, j_b + \frac{1}{2}) = H_x(i, j_b + \frac{1}{2}) - 0.5E_{z_{inc}}(j_b) \quad (3.92)$$

The third one  $H_y$  at just outside  $i = i_a$  and  $i = i_b$ :

$$H_y(i_a - \frac{1}{2}, j) = H_y(i_a - \frac{1}{2}, j) - 0.5E_{z_{inc}}(j) \quad (3.93)$$

$$H_y(i_b + \frac{1}{2}, j) = H_y(i_b + \frac{1}{2}, j) + 0.5E_{z_{inc}}(j) \quad (3.94)$$

Generating the total / scattered fields in three-dimensions is the same as the two-dimensional case. Only the following modification must be made besides the modification made during the two-dimensional case:

$$D_y \left( i, j + \frac{1}{2}, ka \right) = D_y \left( i, j + \frac{1}{2}, kb \right) - 0.5H_{xinc}(j) \quad (3.95)$$

$$D_y \left( i, j + \frac{1}{2}, kb + 1 \right) = D_y \left( i, j + \frac{1}{2}, ka \right) + 0.5H_{xinc}(j) \quad (3.96)$$

The total / scattered field at “ka” is depicted at Figure 3-5.

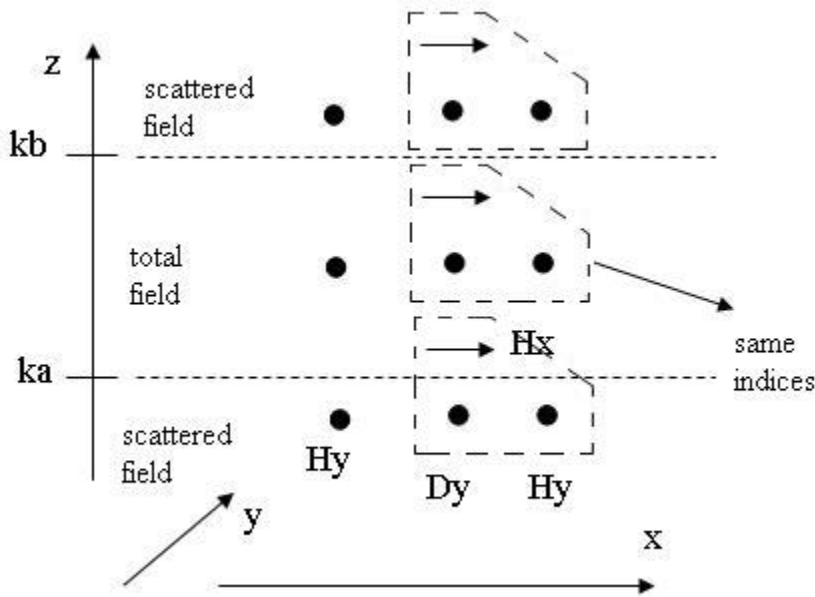


Figure 3-5 Fields Vectors at  $k_a$

## 3.2 Simulation Results

The method defined above is implemented in MATLAB and RCS values of some objects are evaluated with the code.

### 3.2.1 2-D $TM_z$ Results

Sullivan's method has been implemented in the simulation code [18]. Two dimensional  $TM_z$  electromagnetic field simulations are performed in MATLAB. As it is explained in reference [18], normalized electric field and electric displacement values are used. UPML is used as the absorbing boundary condition. The plane wave excitation and TF / SF method are used. Near to far field transformation introduced in [25] by Taflove is utilized on the near scattered field to obtain RCS at far field. Frequency transformation is made at a single frequency (1.5 GHz) to acquire phasor domain values of the time domain scattered field values.

The MATLAB code for 2-D  $TM_z$  waves is written and some simulations are performed with a circular cylinder and square cylinder. Simulation results are compared with the exact and Method of Moment (MoM) calculations in Figure 3-6, Figure 3-7, and Figure 3-8.

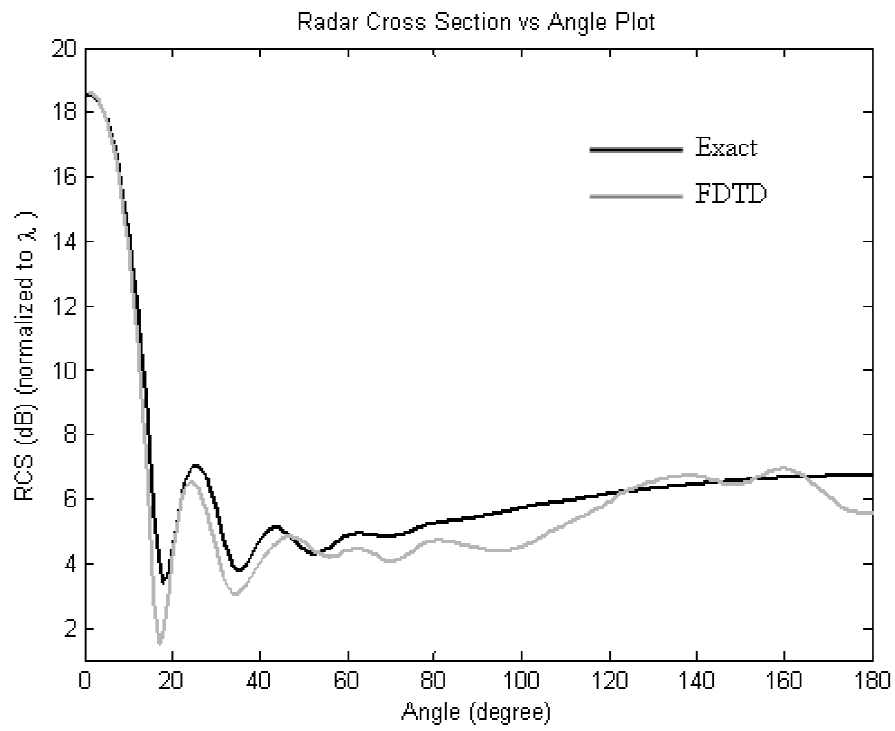


Figure 3-6 Bistatic RCS of a PEC Circular Cylinder with “ $r = 1.5\lambda$ ”

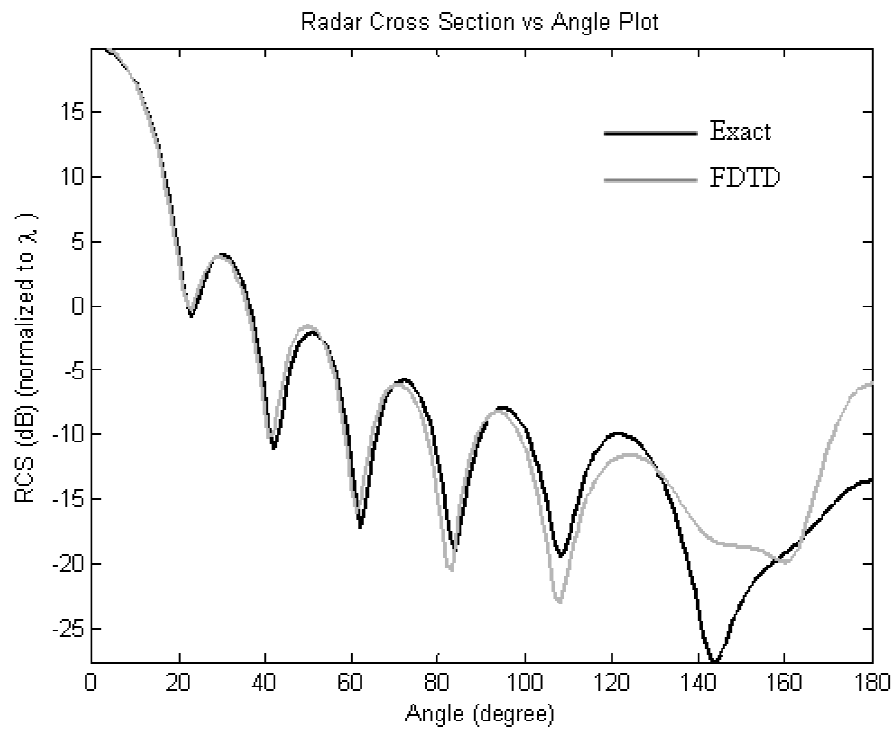


Figure 3-7 Bistatic RCS of a Dielectric Circular Cylinder with “ $\epsilon_r = 1.2$  and  $r = 1.5\lambda$ ”

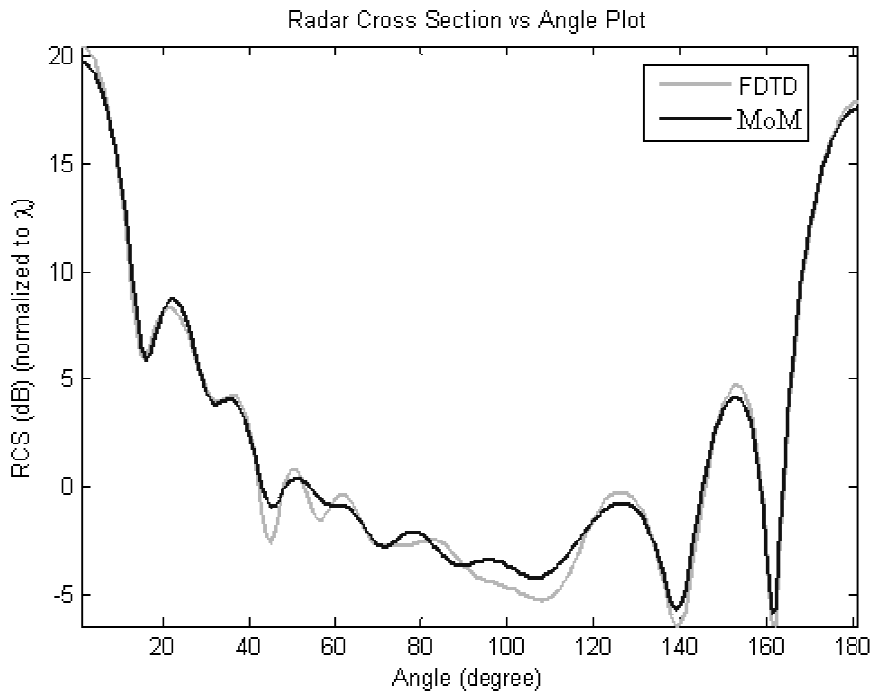


Figure 3-8 Bistatic RCS of a PEC Square Cylinder with “Side-length =  $3\lambda$ ”

As it could be understood from the figure above that FDTD method gives more accurate results when the staircase error is eliminated by fitting the geometry of the object to the Cartesian grid. Since the object in this simulation is square, its shape is more convenient for FDTD characterized by Cartesian coordinate system.

### 3.2.2 3-D Results

In 3-D MATLAB code, firstly the constants are defined. The field and auxiliary vectors are initialized to the initial values. After that the parameters are calculated over the space coordinate to define the PML cells and the PEC sphere.

The main parts of the code (i.e., time stepping of the electromagnetic fields, total / scattered field boundary implementation) are written. The frequency domain electric and magnetic fields vectors are evaluated over the imaginary surface which depends on the surface equivalence theorem.

The near to far field conversion is applied after the time stepping part. The current densities are found from the scattered field vectors which are in the phasor domain. Then the  $\mathbf{N}$  and  $\mathbf{L}$  vectors are calculated with the method introduced in Chapter 2. The RCS of the PEC sphere is drawn by the vectors.

The MATLAB code for 3-D is written and some simulations are performed with a sphere.

The RCS of the PEC sphere found by the FDTD simulation does not match to the exact result because of imperfection of the method. Converting Maxwell’s equations to the finite difference format brings some error to the simulation. The RCS of the PEC sphere is depicted in the Figure 3-10 and the RCS of dielectric sphere is given in Figure 3-9.

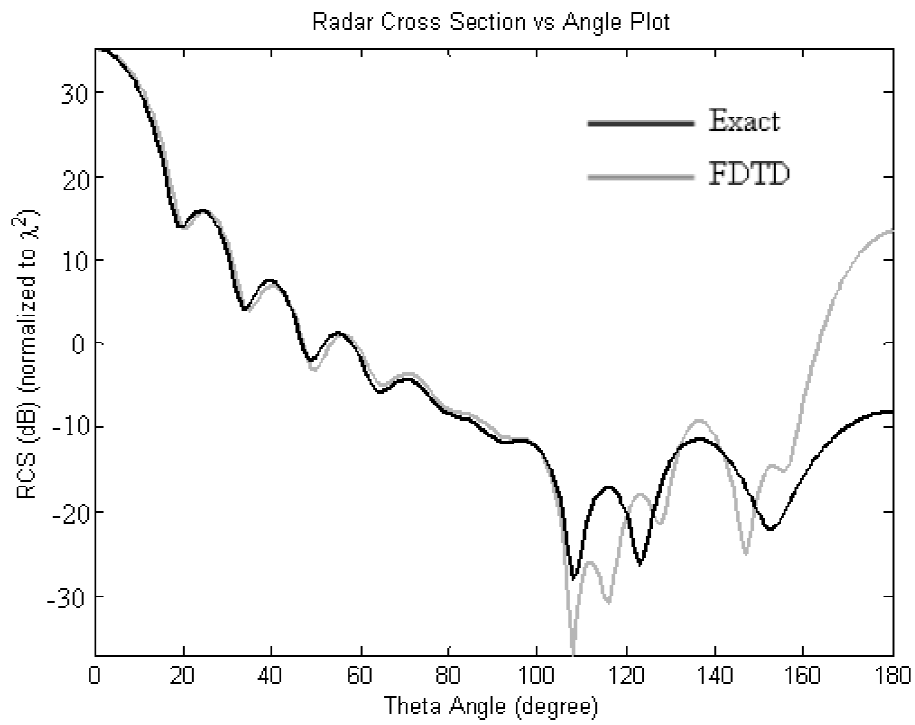


Figure 3-9 Bistatic RCS of a Dielectric Sphere with “ $\epsilon_r = 1.2$  and  $r = 2\lambda$ ”

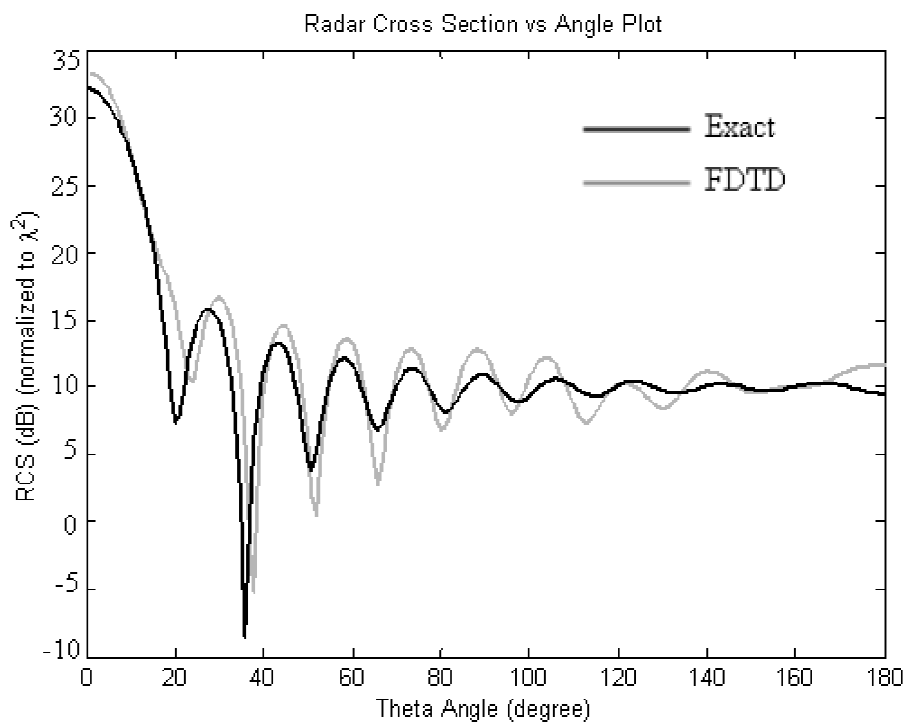


Figure 3-10 Bistatic RCS of a PEC Sphere with “ $r = 2\lambda$ ”

### 3.3 “1/2” Problem between the Electric and Magnetic Fields

When it is tried to obtain RCS of an arbitrary object, the electric and magnetic currents over a surrounding surface is needed to calculate the scattered far field values. Transformation from near to far field requires that the electric and magnetic fields are defined over a single surface and at the same time which is related to the fields phase references [18]. For example, the electromagnetic field positions on a surface with respect to Yee algorithm is seen in Figure 3-11. If the electric field on the single surface is taken, there is “(1/2) $\Delta_x$  or (1/2) $\Delta_y$ ” spatial offset between the magnetic fields and the electric field.

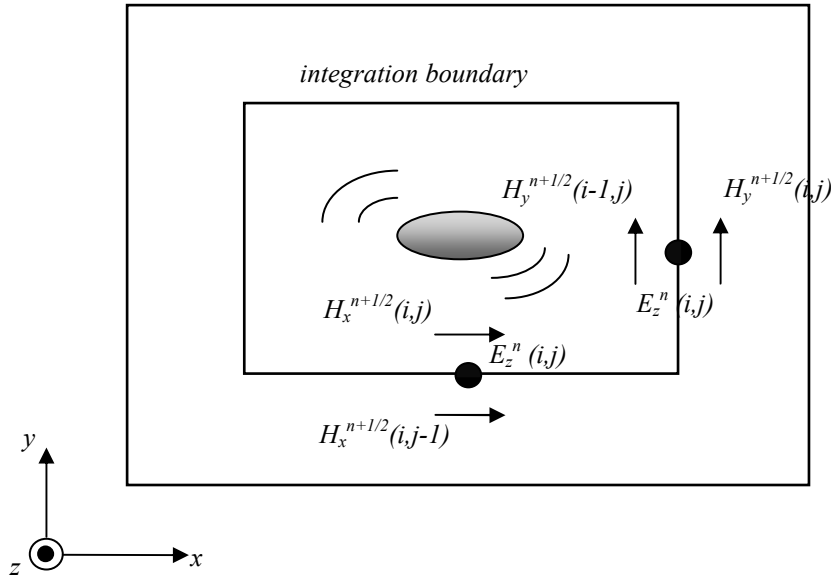


Figure 3-11  $TM_z$  Grid Representation

In terms of the time difference during FDTD calculation, it could be seen that also there is “1/2” time offset between the electric and magnetic fields because of the leap-frog algorithm. The equations defined in the FDTD methodology could be given as follows:

$$H_x^{(n-\frac{1}{2})\Delta t}(i\Delta_x, [j + \frac{1}{2}]\Delta_y) = H_x^{n-\frac{1}{2}}(i, j) \quad (3.97)$$

$$H_y^{(n-\frac{1}{2})\Delta t}([i + \frac{1}{2}]\Delta_x, j\Delta_y) = H_y^{n-\frac{1}{2}}(i, j) \quad (3.98)$$

$$E_z^{n\Delta t}(i\Delta_x, j\Delta_y) = E_z^n(i, j) \quad (3.99)$$

where, n is the temporal step.  $\Delta_x$  and  $\Delta_y$  are the spatial increments. The space and time problem is shown at the equations. The problems will be explained in the following parts.

#### 3.3.1 Temporal Offset Effect on Signal

The temporal offset could easily be modeled with a phase factor for the frequency domain data. The electric fields are calculated at “ $n = 1, 2, 3...$ ” time steps and the magnetic fields are evaluated at half time alternate where “ $n = 3/2, 5/2, 7/2...$ ”. The Fourier Transform of a discrete signal and its “1/2” temporal offset could be written as follows:

$$E_z^n(i, j) = \sum_{k=\langle NT \rangle} \hat{E}_z^k(i, j) e^{-j_j k \frac{2\pi}{NT} n} \quad (3.100)$$

$$E_z^{n-1/2}(i, j) = \sum_{k=\langle NT \rangle} (\hat{E}_z^k(i, j) e^{-j_j k \frac{\pi}{NT}}) e^{j_j k \frac{2\pi}{NT} n} \quad (3.101)$$

Where  $j_j$  denotes  $\sqrt{-1}$ . The  $\hat{E}_z^k(i, j)$  term is the Fourier transform of our signal  $E_z^n(i, j)$ . It could be stated that it is possible to multiply the Fourier transform form of the field ( $\hat{E}_z^k(i, j)$ ) by the factor ( $e^{-j_j k \frac{\pi}{NT}}$ ) to account for the temporal offset situation of the signal. The “1/2” time offset problem can be eliminated by this method.

### 3.3.2 Spatial Offset Effect on Signal

In Figure 3-11, the spatial offset between the electric and magnetic fields are shown. A method which is mostly used to eliminate this problem is that the spatial average of the nodes at either side of the boundary is applied to the magnetic field and it is assumed that the result of this mean is equal to the boundary values of the magnetic field [44], [25]. However, it is going to be proved that the method is not a useful technique to overcome the trouble. Utilizing arithmetic mean to the magnetic fields is provided by the next equation:

$$\hat{H}_y^k(i, j) = \frac{1}{2} \mathcal{F}[H_y^{n-\frac{1}{2}}(i-1, j) + H_y^{n-\frac{1}{2}}(i, j)] \quad (3.102)$$

It is presumed that the spatial offset problem is gotten rid of by the technique. These values are later used to transform the near field to the far field. The Fourier Transform of the time domain data is (assume  $H_y$  is a harmonic plane wave):

$$H_y^{n-\frac{1}{2}}(i, j) = \cos\left(\omega \left[n - \frac{1}{2}\right] \Delta_t - \xi\right) \quad (3.103)$$

$$= \frac{e^{j_j(k' \frac{2\pi}{NT} [n-\frac{1}{2}] \Delta_t + \xi)} + e^{-j_j(k' \frac{2\pi}{NT} [n-\frac{1}{2}] \Delta_t + \xi)}}{2}$$

$$\hat{H}_y^{k'}(i, j) = \frac{1}{2} e^{-j_j [k_x (i + \frac{1}{2}) \Delta_x + k_y j \Delta_y]} \quad (3.104)$$

Fourier Transform of the arithmetic mean is:

$$\hat{H}_y^{k'}(i, j) = e^{-j_j k_y j \Delta_y} \frac{e^{-j_j k_x (i - \frac{1}{2}) \Delta_x} + e^{-j_j k_x (i + \frac{1}{2}) \Delta_x}}{4} \quad (3.105)$$

$$= \frac{1}{2} e^{-j_j (k_x i \Delta_x + k_y j \Delta_y)} \cos\left(\frac{k_x \Delta_x}{2}\right)$$

The first part of the equation is exact expression for the magnetic field on the boundary, but cosine part represents an error on signal. When we examine the cosine term, it goes to zero only if the spatial increment is zero. Taking average after the transformation also gives the same result with the equation above.

In Figure 3-12 [16], the results are given in the Schneider’s book for a circular PEC cylinder. The simulation results are not the same exactly but close to the given results. The problem defined by Schneider [16] is that “1/2” time and space difference between the electric and magnetic field causes mismatch between exact solution and FDTD results.

As it is shown in Schneider’s book, the FDTD calculations do not fit precisely to the exact solution, since there is 1/2 difference between the magnetic and the electric field during post processing of FDTD where near to far field transformation is performed . The 1/2 difference directly reflects over surface currents and it causes the incorrectness on RCS.

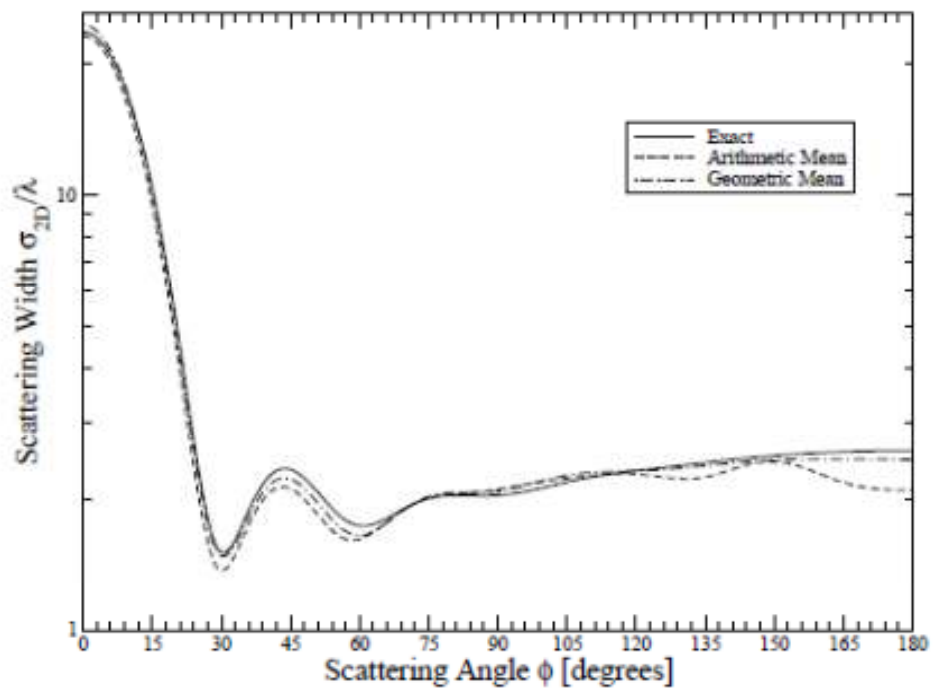


Figure 3-12 Bistatic RCS of PEC Circular Cylinder with “ $r = 4\lambda/5$ ” [16]

## CHAPTER 4

### EFFECTS OF MATERIAL AND/OR SHAPE UNCERTAINTIES OVER RCS

This chapter is dedicated to the analysis of some stochastic problems of electromagnetics via the FDTD code which has been explained in chapters 2 and 3. For certain cases, the FDTD results are verified by means of analytical solutions (provided that they are available) and also by the Method of Moments (MoM). The FDTD code is effective to analyze parameter and shape uncertainties. Since stochastic analysis is carried out by Monte Carlo simulations, the randomness in shape and/or material parameters are taken into account by choosing samples of these from a pre-defined set. In the context of FDTD analysis, this corresponds to change the relative permittivity values of the cells or the shape of the object while the computational domain is kept fixed. Also the change in the RCS of a main object in the presence of secondary small objects is easy to examine by applying the FDTD code.

The incident wave is assumed to come from  $-y$  direction in all simulations explained below. Also, the space increment is taken as  $\lambda/20$  in all simulations.

#### 4.1 Effect of Material and Shape Uncertainties over RCS

Albeit measurement devices give information about the specification and shape of materials, it may not be possible to get adequate data for real objects. The presence of uncertainty of material properties affects simulation results in practical applications. For example, the imprecision in permittivity and conductance of human tissues brings an error to simulation which deviates away from the ideal results. The sources of imprecision are mostly rooted in randomness of material parameters and geometry of objects. Although technological improvements in measuring devices mitigate impact of uncertainty, the imperfection in the real world cannot be eliminated completely.

Unless the source of the randomness could be eliminated, the consequences of ambiguity have to be examined to overcome the problem. There are some methods to examine the reflection of uncertainty over simulation results. The mean and standard deviation of simulation results for RCS of objects could be obtained. The impact of uncertainty on the simulation response may be predicted in the early stages of calculation by knowing the uncertainty profile of random material parameters and object geometry in the model.

This problem can be examined by Monte Carlo Analysis. Although it is a time consuming method to deal with, the method could be applied to all kinds of statistical problems. It is usually unproblematic to utilize the Monte Carlo Method extensively in engineering. Stochastic analysis is generally justified by Monte Carlo Analysis because of its robustness.

FDTD is a suitable method to analyze the imperfections or uncertainties in the outside world via the Monte Carlo Method. When the Monte Carlo method is utilized, the following steps are pursued: Firstly, the input parameters must be analyzed. Potential inputs and their statistical characteristics must be defined at the beginning. Samples of the inputs are generated randomly according to their statistical characteristics. The deterministic computation is executed by using the randomly generated samples of the inputs. After that, all simulation results are collected and analyzed to gather their statistical properties. Allowing the use of the deterministic model for the simulation is the most powerful aspect of the Monte Carlo approach. The data for statistical analysis are collected through several simulations carried out for the set of samples of input variables.

##### 4.1.1 Results for Permittivity Uncertainties

Some simulations are run for a circular dielectric cylinder whose radius is equal to  $\lambda/2$  and square dielectric cylinder whose dimension is equal to  $\lambda$ . First of all, the relative permittivity values are

produced with respect to normal distribution (Gaussian distribution) whose probability density function is as follows;

$$f(x) = \frac{1}{\sqrt{2\pi\sigma_{sd}^2}} e^{-\frac{(x-\mu_m)^2}{2\sigma_{sd}^2}} \quad (4.1)$$

Where  $\sigma_{sd}$  and  $\mu_m$  denote standard deviation and mean. The produced relative permittivity data are taken as input for our 2D – FDTD code and RCS values are calculated via the simulation. After that, the attained RCS values are gathered over a histogram to analyze its distribution characteristics. The mean and standard deviation parameters of the RCS are computed by using the obtained data. The mean and variance formulation are given below;

$$\mu_m = E[x] = \int_{-\infty}^{+\infty} xf(x)dx \quad (4.2)$$

$$\sigma_{sd}^2 = E[(x - \mu_m)^2] = \int_{-\infty}^{+\infty} (x - \mu_m)^2 f(x)dx \quad (4.3)$$

The standard deviation is equal to the square root of the variance. The equations are for the continuous domain calculation. They are converted to the discrete domain as follows;

$$E[x] = \frac{1}{N} \sum_{n=1}^N X_n \quad (4.4)$$

$$E[(x - \mu_m)^2] = \frac{1}{N} \sum_{n=1}^N (X_n - \mu_m)^2 \quad (4.5)$$

#### 4.1.1.1 Permittivity Uncertainties for Dielectric Circular Cylinder

As it is stated, the simulations are run for the circular cylinder whose radius is  $0.5\lambda$ . The first set of data are collected for the relative permittivity values whose mean is 3 and standard deviation is equal to 0.1 as shown in Figure 4-1.

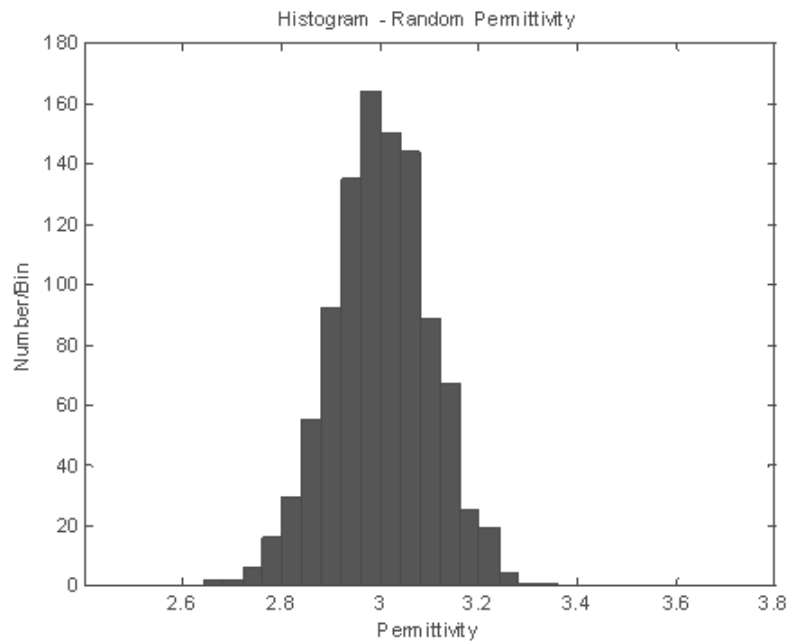


Figure 4-1 Relative Permittivity Histogram for ( $\mu_m = 3$  and  $\sigma_{sd} = 0.1$ )

The results gathered via FDTD could be seen in Figure 4-2. The RCS values are shown on a histogram. The mean of RCS data, which are calculated through normal (dimensionless) RCS values and converted to the dB scale, is 13.1344 dB, and its standard deviation calculated with the same method is equal to 3.9758 dB. A normally distributed curve which has the same mean and standard deviation values with RCS values is fitted in Figure 4-2. The Gaussian curve is fitted to the histogram by MATLAB function “*histfit*”.

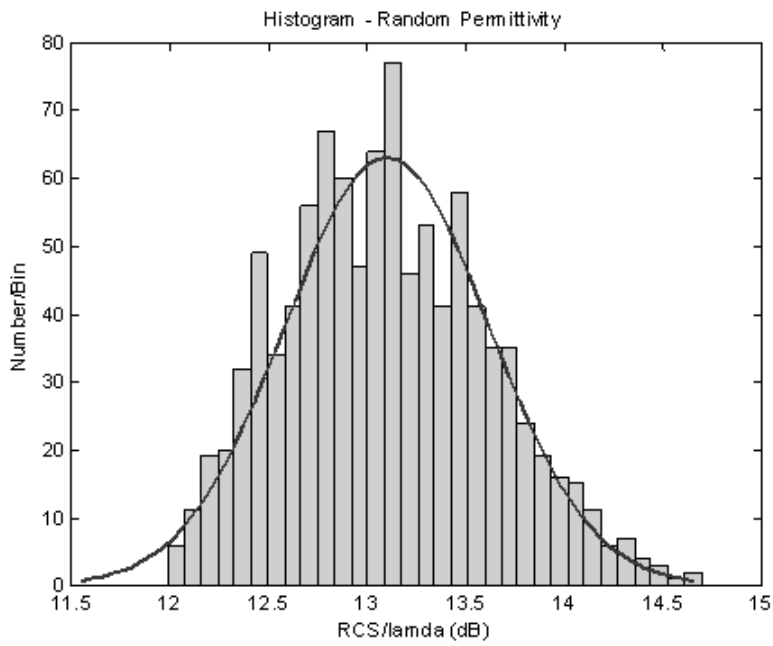


Figure 4-2 Forward RCS Distribution via FDTD for ( $\mu_m = 3$  and  $\sigma_{sd} = 0.1$ )

The second set of data are obtained by relative permittivity values which are normally distributed with mean 3 and standard deviation 0.5 as given in Figure 4-3.

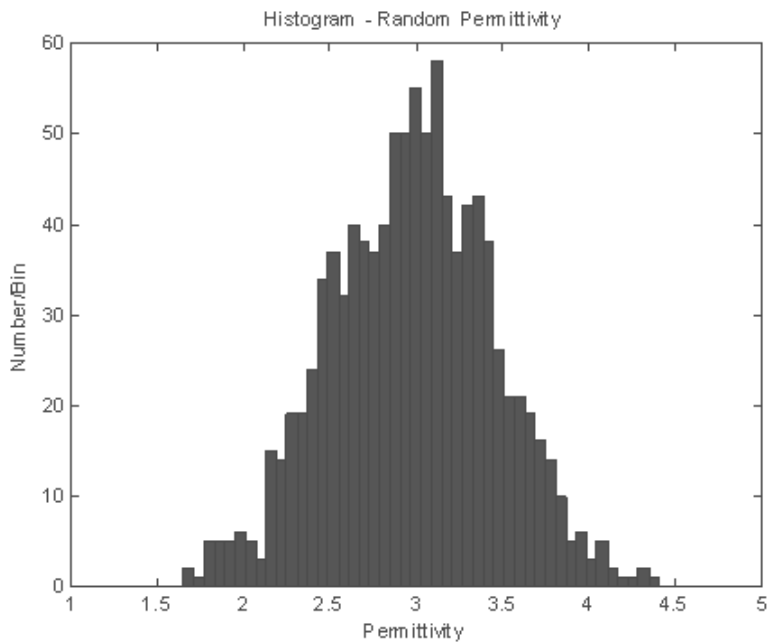


Figure 4-3 Relative Permittyvity Histogram for ( $\mu_m = 3$  and  $\sigma_{sd} = 0.5$ )

Firstly, the RCS values are calculated via FDTD as shown in Figure 4-4 and it could be understood that the RCS does not match with a known distribution. It mostly accumulates around 12 dB. The mean and standard deviation of the RCS are calculated as 13.2944 dB and 7.7295 dB.

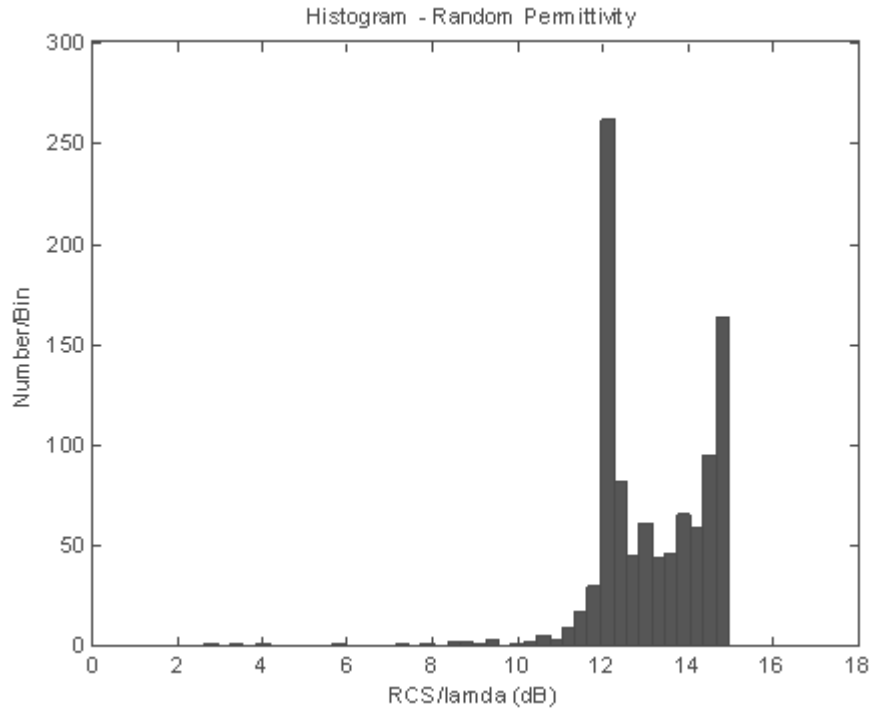


Figure 4-4 Forward RCS Histogram via FDTD for ( $\mu_m = 3$  and  $\sigma_{sd} = 0.5$ )

To sum up, if the variance of relative permittivity is sufficiently small, the RCS of the object is close to Gaussian distribution. As we expect the mean of RCS is exactly driven from the mean of relative permittivity.

The forward RCS of circular cylinder is plotted with respect to the relative permittivity to analyze the alteration and trajectory of forward RCS. The results are calculated with FDTD and analytically as given in Figure 4-5. Firstly, the forward RCS traces a dramatic raise up to the point where the relative permittivity is about 2.8. The forward RCS becomes smaller while the relative permittivity comes close to 1. The RCS disappears when the relative permittivity is equal to 1 because of vanishing of scattered field. The forward RCS becomes approximately 15 dB. It can be seen that the increase is not definitive. The incident wave interaction with the object develops into a complex form. Then, the RCS shows a decrease up to 0 dB and again an increase which is finally around 15 dB. Now, if stochastic results given above are thought under this outcome, they can be taken as expected. The RCS values pass the local maximum (corresponding to the relative permittivity at 2.8) easily when the standard deviation is taken as 0.5. Therefore, the gathered forward RCS values lose their Gaussian form. However, the RCS preserves its Gaussian form when the standard deviation is small enough like 0.1. Because, the RCS values corresponding to most of the relative permittivity values generated cannot reach the local maximum. The dependence of RCS on input relative permittivity does not degenerate, and the forward RCS illustrates a Gaussian form.

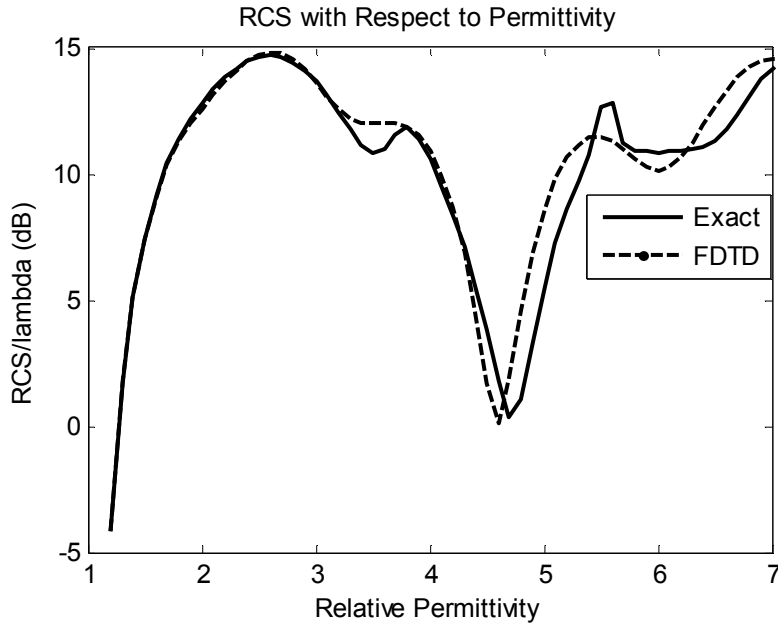


Figure 4-5 Forward RCS as a function of Relative Permittivity for Circular Cylinder ( $Radius = \lambda/2$ )

#### 4.1.1.1.1 Comparison of FDTD with Exact Results for Verification of the Code

The RCS of the circular cylinder for the same permittivity values are calculated by FDTD and analytically. Analytical RCS calculation method is compared with the FDTD results.

The root mean square error is calculated to evaluate the correctness of the FDTD codes. The root mean square error is computed with the following formula:

$$Error = \sqrt{\frac{\sum_{i=1}^N (RCS_{exact}^i - RCS_{FDTD}^i)^2}{N}} \quad (4.6)$$

The results are gathered from analytical and FDTD simulations for randomly generated relative permittivity whose standard deviation is 0.1 in Figure 4-6. The mean and standard deviation turn out to be close to one another and given in Table 4-1.

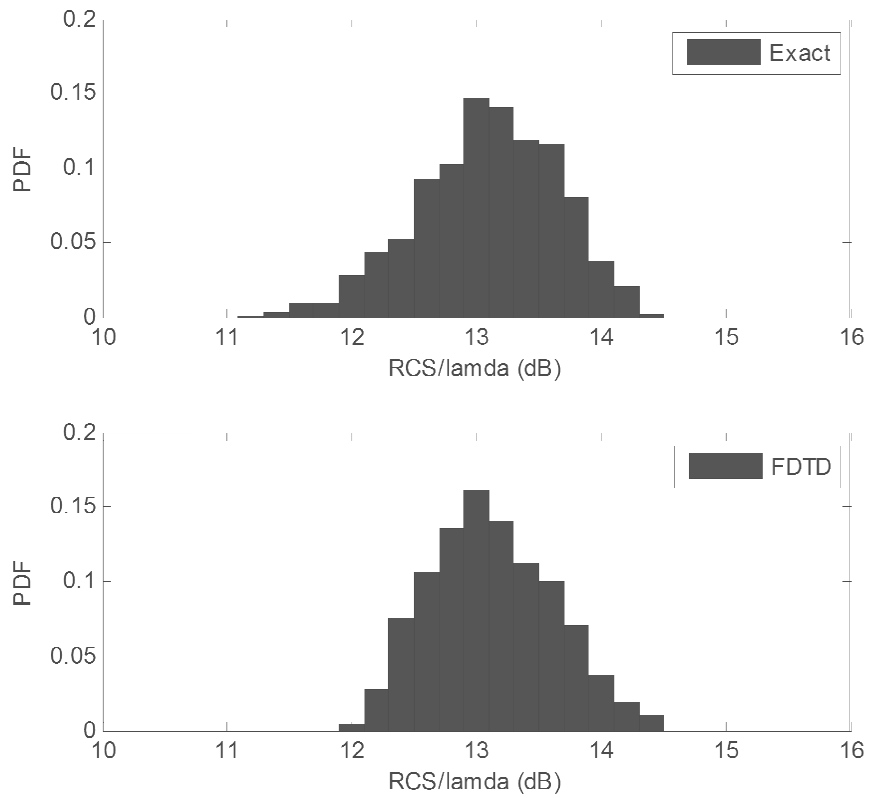


Figure 4-6 Forward RCS Histograms by FDTD and Analytical Method for ( $\mu_m = 3$  and  $\sigma_{sd} = 0.1$ )

As it could be understood from the figures that the results calculated by FDTD and Analytical simulation are close enough, but the results are not the same because of inexactness of FDTD method.

Table 4-1 Evaluation of Code for ( $\mu_m = 3$  and  $\sigma_{sd} = 0.1$ )

	Mean (dB)	Stand. Dev. (dB)	Min. (dB)	Max (dB)
Exact	13,1274	4,1082	11,2926	14,3114
FDTD	13,1528	3,7815	12,0448	14,4439

The Gaussian distribution of relative permittivity reflects to the radar cross section as Gaussian distribution.

When we applied the error formula to the results, it can be calculated that the root mean square error of FDTD results as compared to the analytical one is equal to 0.2846 dB. The formula is applied to the dimensionless values of RCS and the root mean square error is calculated in “dB” format after the error calculation.

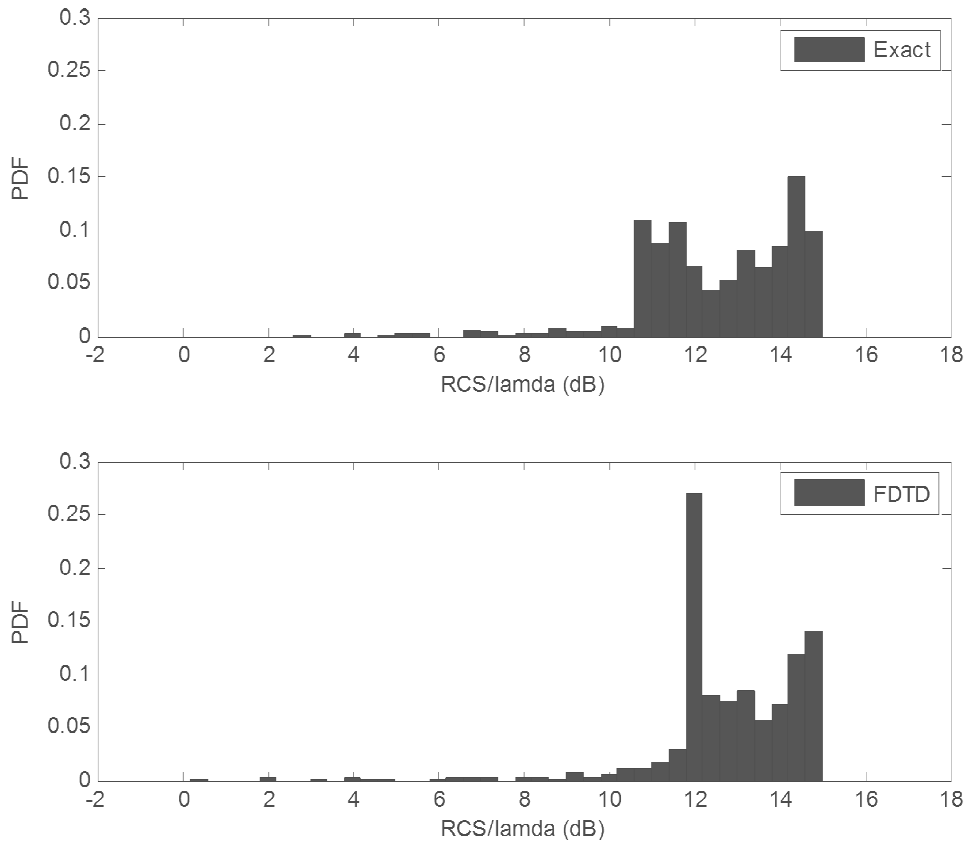


Figure 4-7 Forward RCS Histograms via FDTD and Exact Method for ( $\mu_m = 3$  and  $\sigma_{sd} = 0.5$ )

Table 4-2 Evaluation of Code for ( $\mu_m = 3$  and  $\sigma_{sd} = 0.5$ )

	Mean (dB)	Stand. Dev. (dB)	Min. (dB)	Max (dB)
Exact	12,9272	8,2653	14,7166	2,6162
FDTD	13,1286	7,8661	14,8219	0,4241

The results gathered by Analytical and FDTD methods for the standard deviation of relative permittivity 0.5 are given in Figure 4-7. The mean and standard deviation are given in Table 4-2. The root mean square error is calculated with the formula given above and its result is 0.6636 dB.

The errors found above show that the FDTD code is fair enough to be used with the random relative permittivity. The outcomes gathered passing through the FDTD code give nearly accurate results.

#### 4.1.1.2 Permittivity Uncertainties for Dielectric Square Cylinder

Simulations related to permittivity uncertainties are also performed for square cylinders with diameters equal to  $\lambda$ . Again, the relative permittivity is defined as a Gaussian random variable with 3 as the mean and 0.5 as standard deviation, as shown in Figure 4-8.

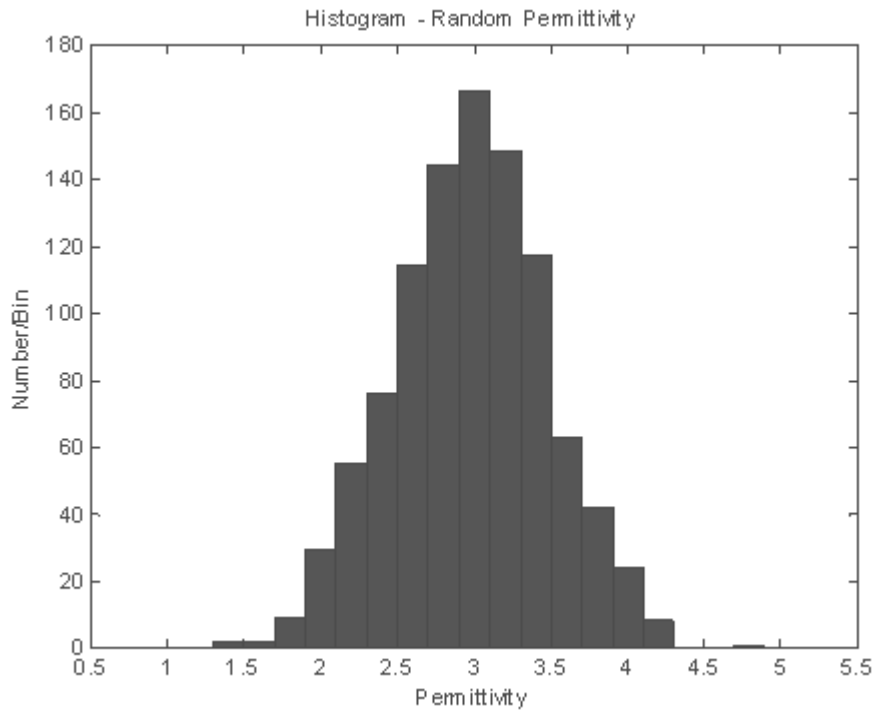


Figure 4-8 Relative Permittivity Histogram for ( $\mu_m = 3$  and  $\sigma_{sd} = 0.5$ )

The RCS values calculated by FDTD method are given in Figure 4-9. The standard deviation and mean of RCS are evaluated as 11.3962 dB and 14.8079 dB. From the histogram it is not possible to associate a meaning to the distribution of the RCS values. Therefore, we try to understand how the RCS changes with respect to the relative permittivity, by increasing the relative permittivity gradually.

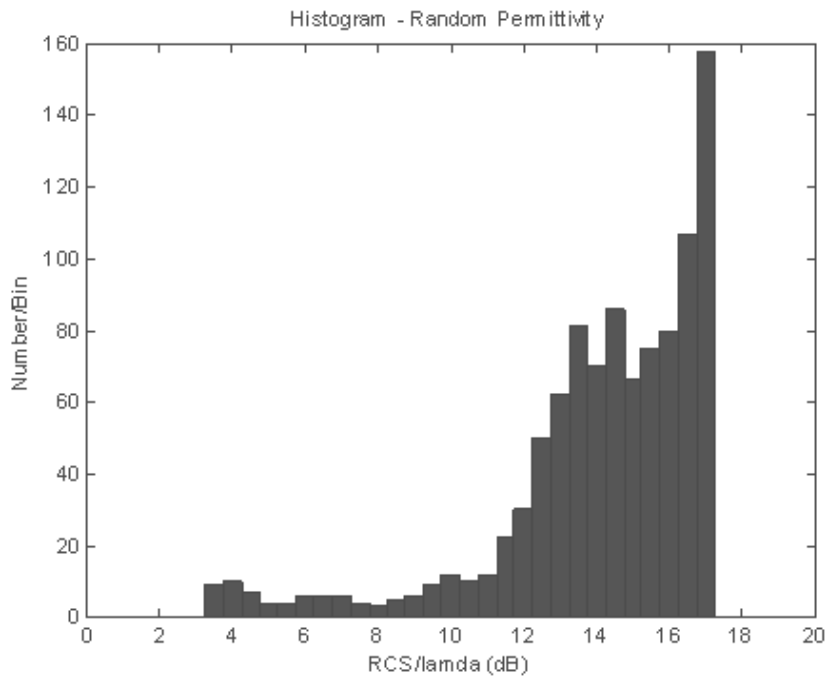


Figure 4-9 Forward RCS Histogram via FDTD for ( $\mu_m = 3$  and  $\sigma_{sd} = 0.5$ )

When we draw the RCS with respect to relative permittivity which increases gradually, the RCS distribution could be interpreted (in Figure 4-10). The RCS has a peak value around 17 dB and after that value the RCS stops to increase. As expected there is a local maximum near 3 which is mean of the relative permittivity for radar cross section. Thus, the local maximum explains the sharp stop.

The forward RCS of a square cylinder nearly pursues the same trajectory with the circular cylinder when the relative permittivity is changed. It starts with a sharp increase, which is predictable. When the relative permittivity becomes smaller and finally approaches 1, the scattered field becomes negligible, so the RCS gets weak.

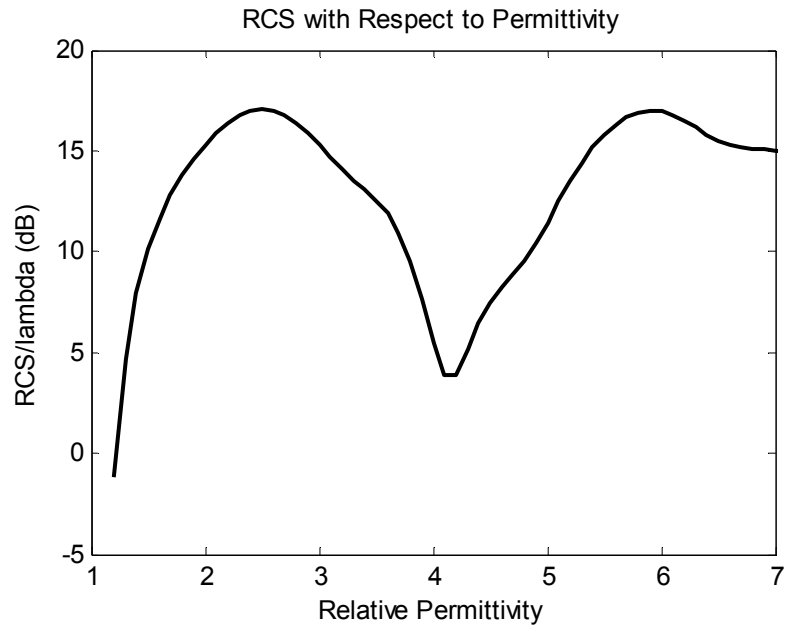


Figure 4-10 Forward RCS as a function of Relative Permittivity for Square Cylinder (*Side-length*= $\lambda$ )

Another simulation for square cylinder is executed for random permittivity values which are distributed normally with mean and standard deviation equal to 3 and 0.1 as can be seen in Figure 4-11.

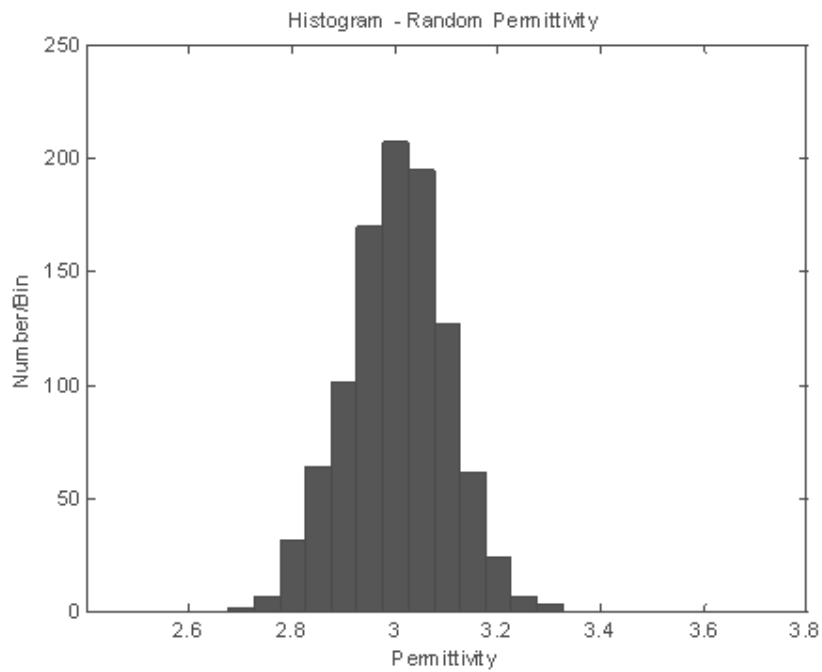


Figure 4-11 Relative Permittivity Histogram for ( $\mu_m = 3$  and  $\sigma_{sd} = 0.1$ )

It is observed that the RCS resembles Gaussian distribution as given in Figure 4-12. The mean and standard deviation are equal to 14.7045 dB and 6.012 dB. The RCS values do not reach the local maximum value, because standard deviation of the relative permittivity is sufficiently low. Therefore, the RCS obeys the behavior of Gaussian distribution.

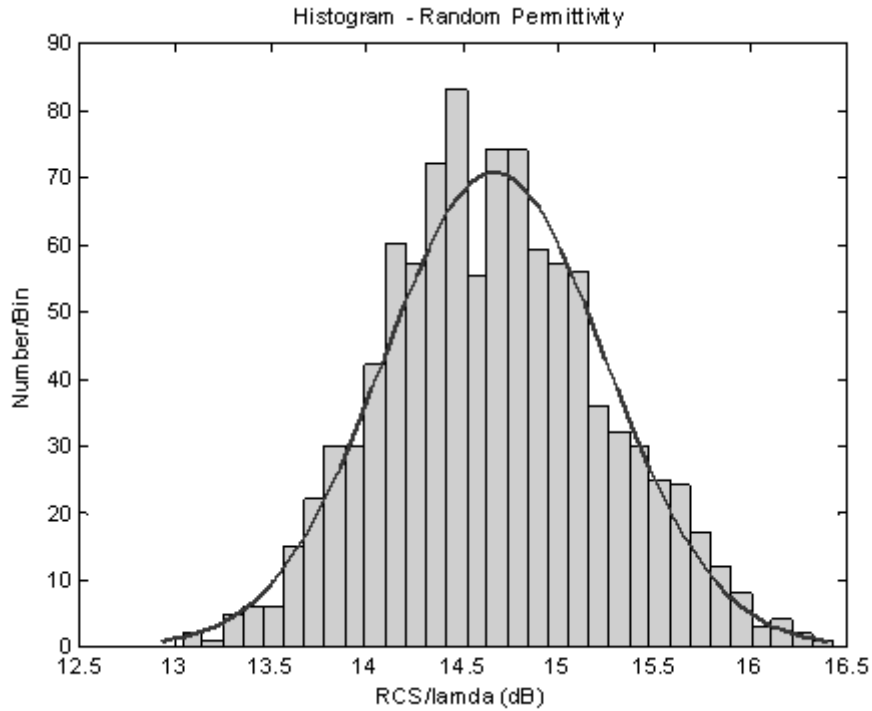


Figure 4-12 Forward RCS distribution via FDTD for ( $\mu_m = 3$  and  $\sigma_{sd} = 0.1$ )

#### 4.1.2 Results for Shape Uncertainties

This section is devoted to the analysis of the effect of an unknown shape imperfection on the RCS of the object.

##### 4.1.2.1 PEC Circular Cylinder with an Omitted Part

A circular PEC cylinder shown in Figure 4-13 with a shape imperfection is used to analyze the problem. A little part of the circle is omitted and this omitted part is rotated randomly around the circular cylinder. The complete circle (i.e. angularly  $360^\circ$ ) is traced by 100 steps. The RCS of the object is computed through the 2D – FDTD simulation program, and the outcomes are presented as a histogram. The mean and standard deviation of the RCS are calculated.

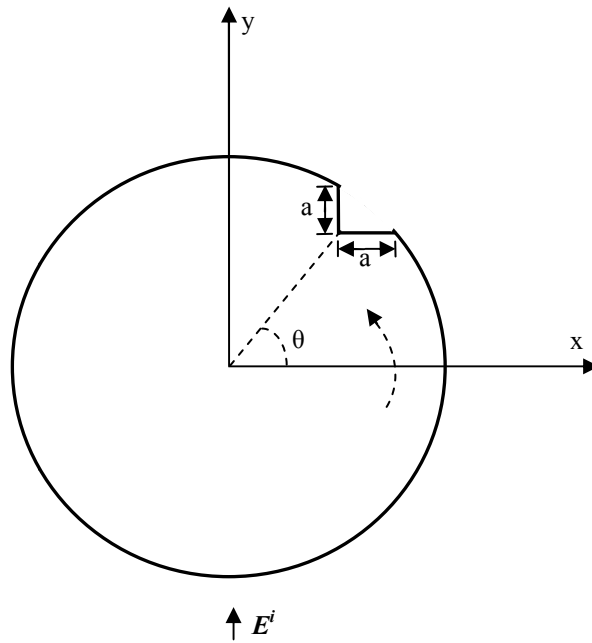


Figure 4-13 Circular Cylinder with an Omitted Part

The first simulation is run with a PEC circular cylinder whose radius is equal to  $\lambda/2$ . The outcomes with a mean around 9.3013 dB and standard deviation -9.6959 dB could be seen in Figure 4-14. The RCS outcomes of the simulation mostly accumulate around the mean. However it could not be asserted that the distribution of the RCS is close a Gaussian distribution.

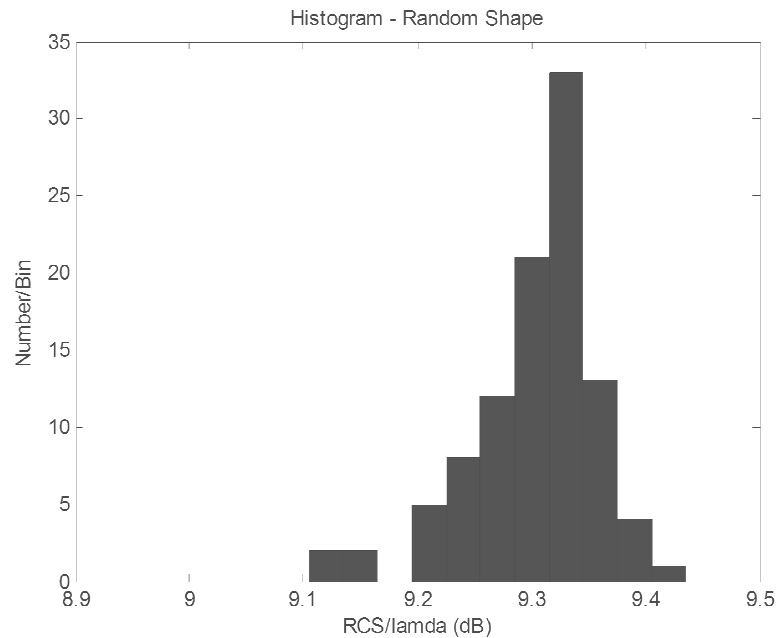


Figure 4-14 Forward RCS Histogram via FDTD for ( $r = 0.5\lambda$  and  $a = 0.1\lambda$ )

The second simulation is carried out by a PEC circular cylinder whose radius is equal to  $\lambda$ . This time as it could be predicted, the variation of RCS is squeezed to a narrower band because of the smaller size of the omitted part as seen in Figure 4-15. The mean and standard deviation are computed as 15.2161 dB and -16.3189 dB.

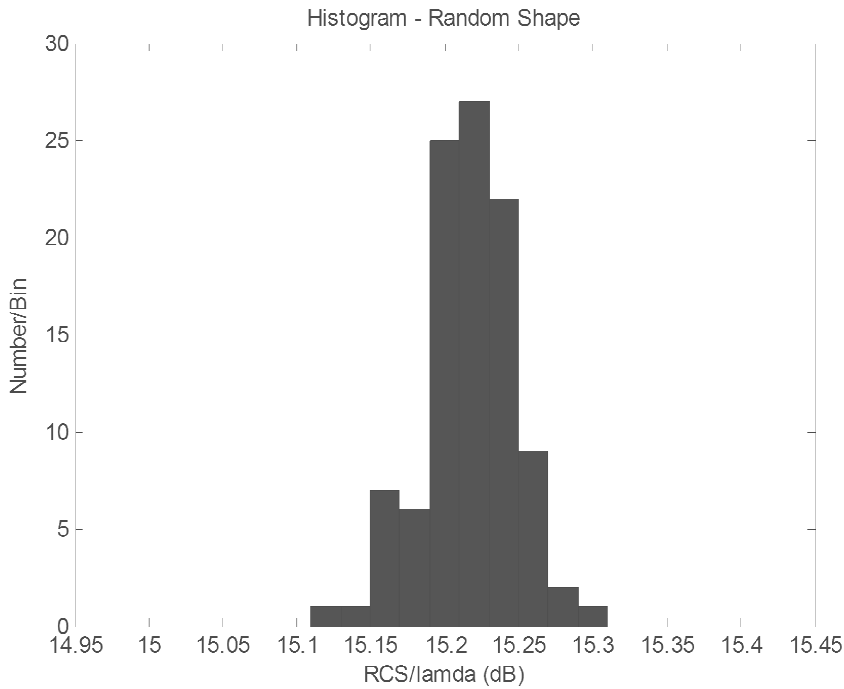


Figure 4-15 Forward RCS Histogram via FDTD for ( $r = \lambda$  and  $a = 0.1\lambda$ )

Approximately 80 percent of the RCS values are very close to the mean which could be interpreted in terms of the very small standard deviation.

**4.1.2.2 PEC Square Cylinder with Shape Uncertainty Modeled in terms of a PEC Square Deformity**

Another simulation is made on a square PEC cylinder having a shape deformity in the form of an exterior square with a random location on the main square cylinder as given in Figure 4-16. The position of the exterior square changes randomly with respect to  $\theta$  angle.

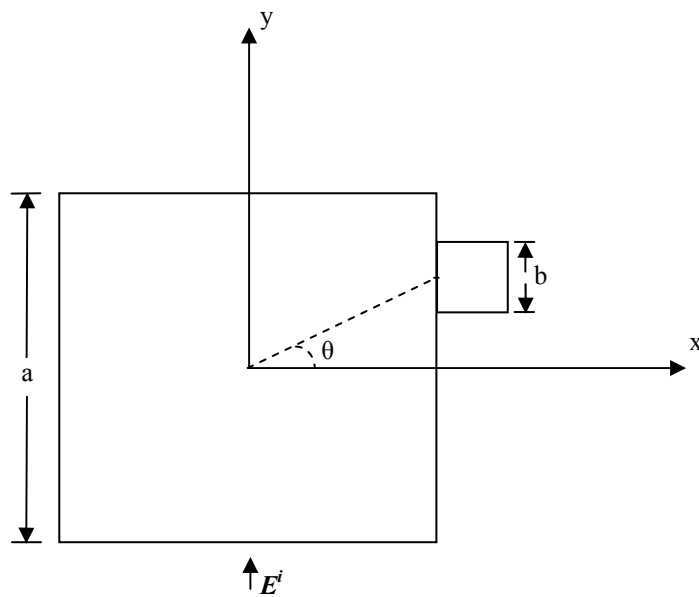


Figure 4-16 PEC Square Cylinder with PEC Square Deformity

The second simulation on shape imperfection is done by the structure given above. FDTD code is updated with respect to the shape given above and the randomness is reflected on the  $\theta$  angle.

The object is subjected to the incident wave coming from  $-y$  direction. First of all, the RCS of the object is calculated by moving the exterior square around the main square to understand how the radar cross section of the object changes with respect to  $\theta$  angle. The results are shown in Figure 4-17 and Figure 4-18, for  $b = \lambda/2$  and  $b = \lambda/4$ , respectively.

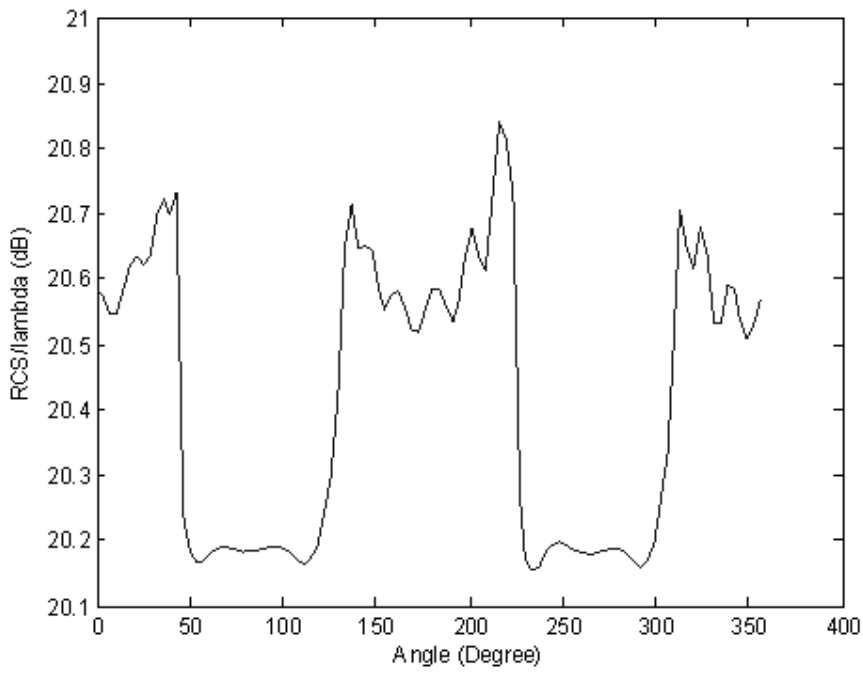


Figure 4-17 Forward RCS as a function of the angular position of the deformity via FDTD for ( $a = 3\lambda$  and  $b = 0.5\lambda$ )

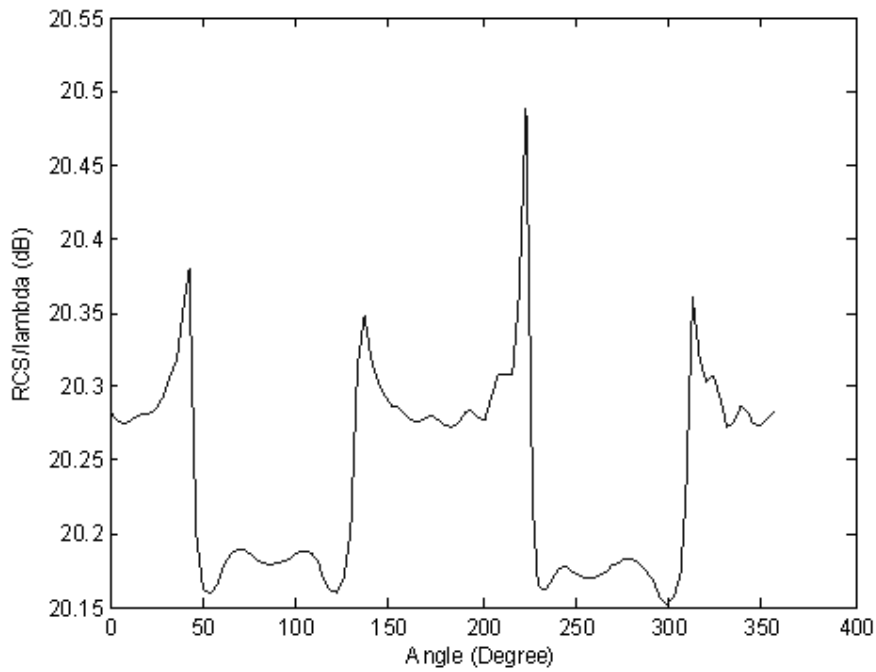


Figure 4-18 Forward RCS as a function of the angular position of the deformity via FDTD for ( $a = 3\lambda$  and  $b = 0.25\lambda$ )

The entire angular range  $360^0$  is divided into a hundred steps during the plotting of the figures above.

The following observations could be inferred from Figure 4-17 and Figure 4-18. The RCS of the object is nearly equal to the RCS of main square when the exterior part is in front and behind of the main object with respect to direction of the incident wave. In such a case, the RCS is not affected by the shape deformity.

The RCS of the object increases when the exterior square is at the lateral side (with respect to the incident field).

Some simulations have been done on the object given in Figure 4-16. The  $\theta$  angle is chosen randomly between  $150^0 - 210^0$  degree with uniform distribution and 100 trials to test the situation where the exterior is at the lateral parts of the main object. The randomly generated angle values are seen in Figure 4-19.

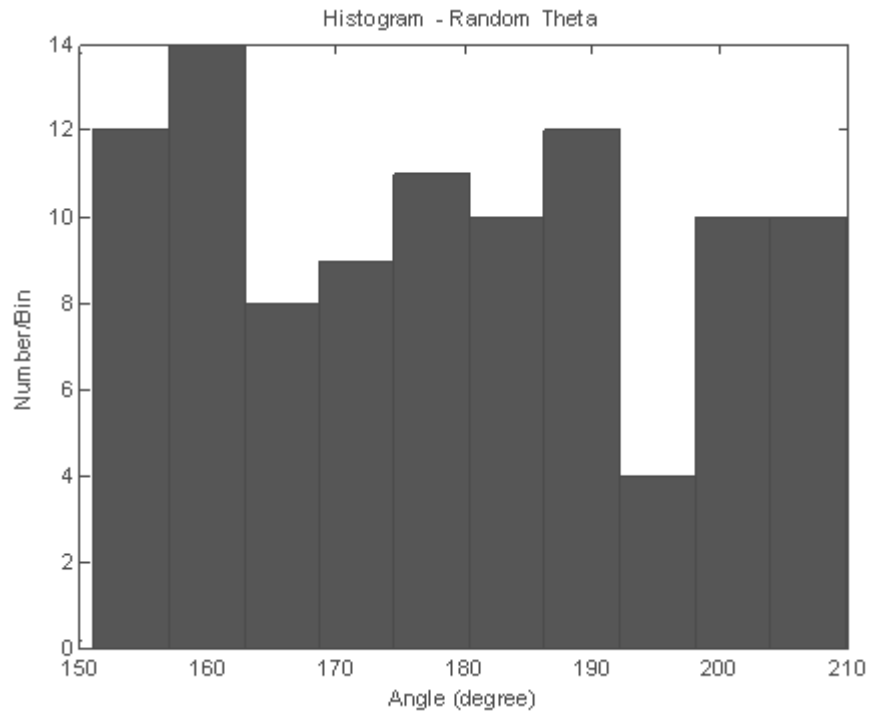


Figure 4-19 Histogram of the Randomly Generated  $\theta$  Values between  $150^0$ - $210^0$

The histograms are plotted for the  $\theta$  values given above assuming that the side-length of square is  $\lambda/2$  and  $\lambda/4$  in Figure 4-20 and Figure 4-21, respectively.

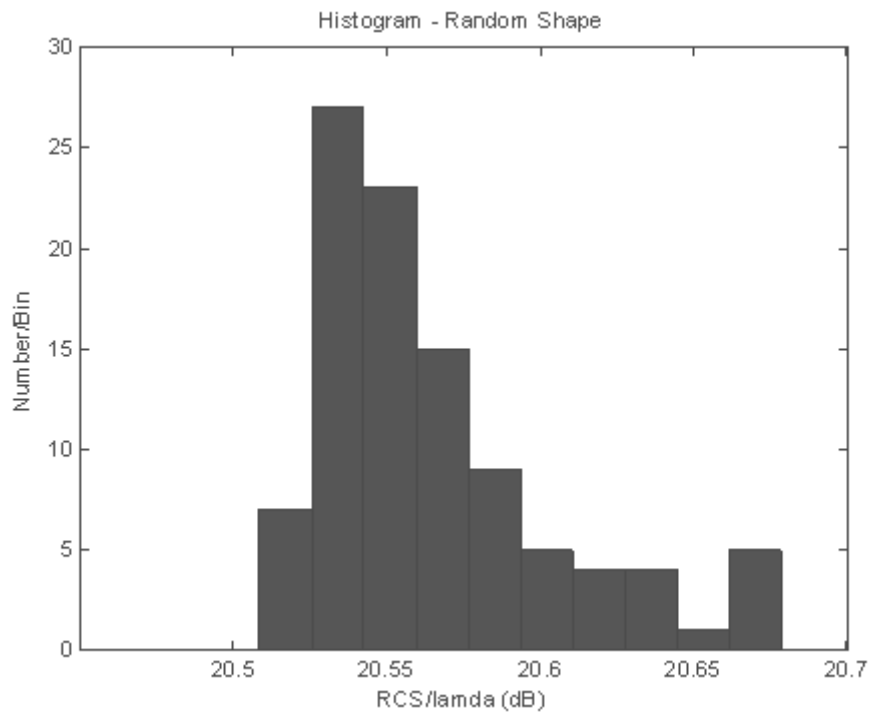


Figure 4-20 Forward RCS Histogram for Angular Position between  $(150^{\circ}-210^{\circ})$  via FDTD for  $(a = 3\lambda$  and  $b = 0.5\lambda)$

The mean and standard deviation are equal to 20.5797 dB and 0.4258 dB for Figure 4-20. The RCS values are almost squeezed in a 0.2 dB range which is a small variation from the mean. This is obviously linked to the small variance parameter.

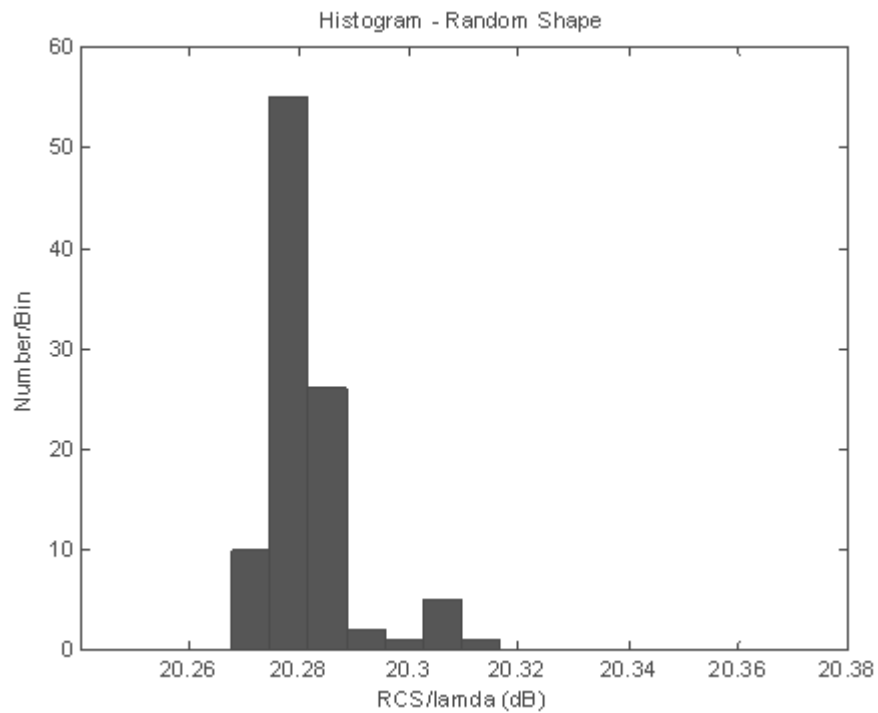


Figure 4-21 Forward RCS Histogram for Angular Position between  $(150^{\circ}-210^{\circ})$  via FDTD for  $(a = 3\lambda$  and  $b = 0.25\lambda)$

The calculated mean and standard deviation values are 20.2818 dB and -6.9217 dB for the case given in Figure 4-21. The mean decreases with respect to the former case because of the decrease in the dimension of the deformity. Also the variation decreases as compared to the former case.

Another experiment is done for the angle changing from  $230^{\circ}$  to  $300^{\circ}$  to test the case when the deformity is located at the back and front parts of the main object (with respect to the incident field coming from the front). The randomly produced angle values with uniform distribution used in 100 trials are given in Figure 4-22.

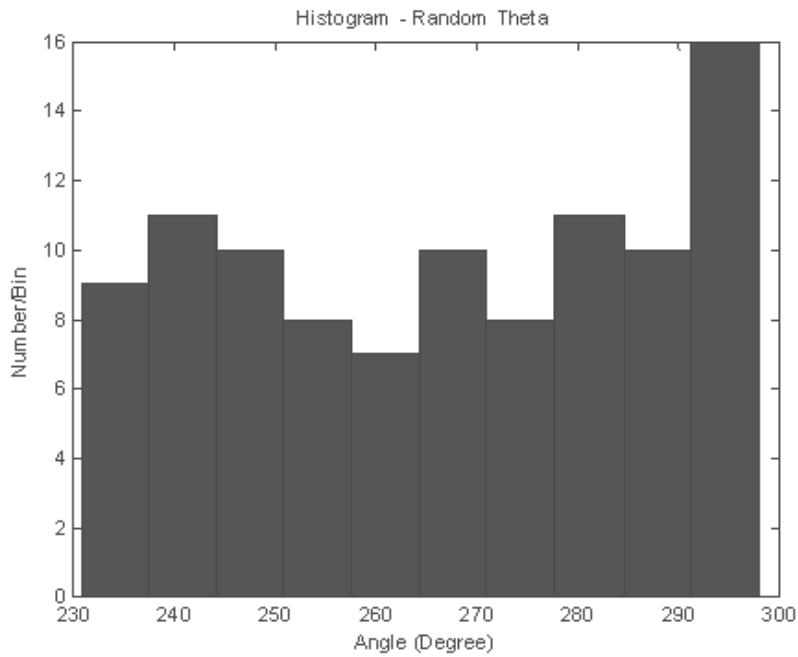


Figure 4-22 Histogram of the Randomly Generated  $\theta$  Values between  $230^{\circ}$ - $300^{\circ}$

The results are computed for two different side-length values of the square deformity ( $\lambda/2$  and  $\lambda/4$ ) and the corresponding histograms are given in Figure 4-23 and Figure 4-24.

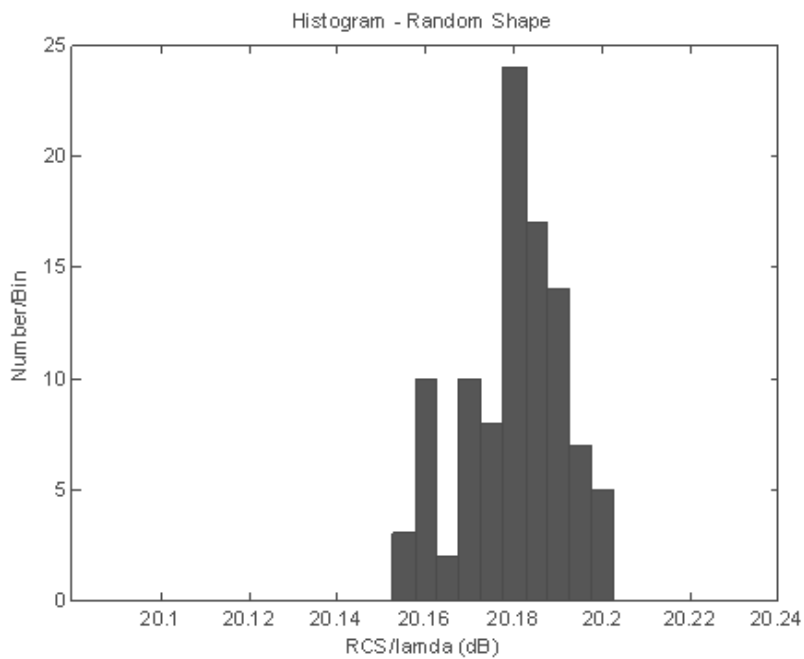


Figure 4-23 Forward RCS Histogram for Angular Position between ( $230^{\circ}$ - $300^{\circ}$ ) via FDTD for ( $a = 3\lambda$  and  $b = 0.5\lambda$ )

The mean and standard deviation of the distribution given above, in Figure 4-23, are equal to 20.1797 dB and -5.6879 dB. If we compare this result with the simulation done for angular positions between  $150^{\circ}$  –  $210^{\circ}$ , its standard deviation is smaller as it is mentioned above that the corresponding change of RCS is small for the case when the deformity lies at the front and back of main object.

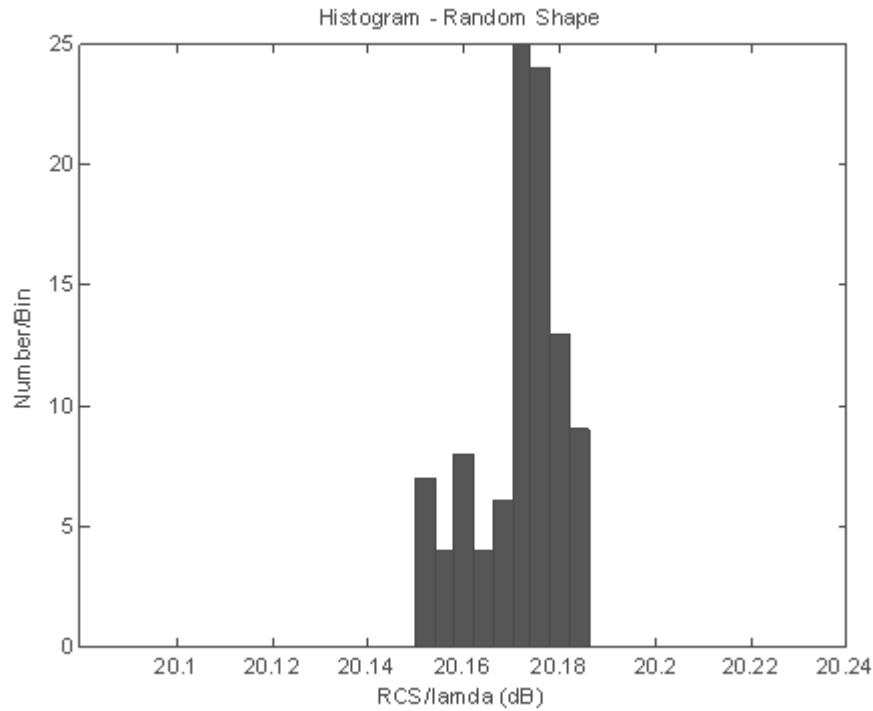


Figure 4-24 Forward RCS Histogram for Angular Position between ( $230^{\circ}$ - $300^{\circ}$ ) via FDTD for ( $a = 3\lambda$  and  $b = 0.25\lambda$ )

The mean and standard deviation of the RCS corresponding to a shape deformity of side-length  $\lambda/4$  are computed and they are equal to 20.1717 dB and -6.9035 dB. The mean is nearly equal to the former, but the standard deviation is smaller which means that if the size of the deformity decreases, the standard deviation of the RCS also decreases.

The mean values calculated in the cases shown in Figure 4-23 and Figure 4-24 are nearly equal to that of the square cylinder which has no shape deformity. If the imperfection of the object lies at the back or front part of the object, its RCS change will not be at a recognizable level.

**4.1.2.2.1 Comparison of FDTD with MoM Results for Shape Imperfection**

As it could be seen from the plots given below, the FDTD results are close to the MoM solutions. The direction of the incident field is “-y” which corresponds to the angular value  $270^{\circ}$ .

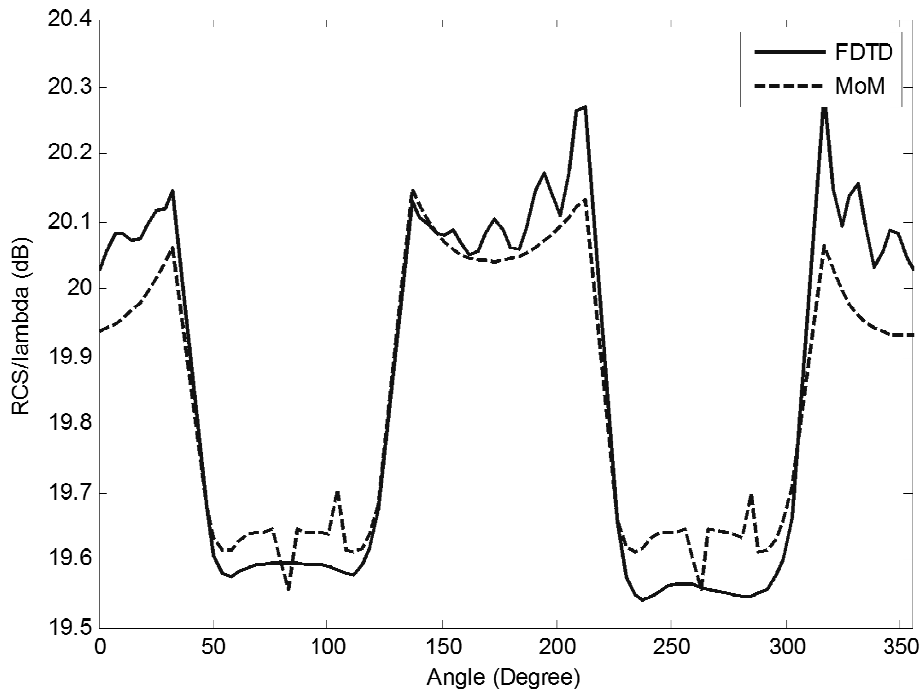


Figure 4-25 Forward RCS as a function of the angular position of the deformity for ( $a = 3\lambda$  and  $b = 0.5\lambda$ )

Mean and standard deviations for the RCS values given in Figure 4-25 are given in Table 4-3.

Table 4-3 Mean and Standard Deviation of Forward RCS in Figure 4-25

	<b>FDTD</b>	<b>MoM</b>
<b>Mean (dB)</b>	19,8528	19,8352
<b>Standard Dev. (dB)</b>	-2,0042	-3,2232
<b>Root Mean Square Error</b>	1,420	

The forward RCS mostly depends the direction of incidence of the incident wave and the location of the deformity. When the incident field does not interact with the deformity directly, the forward RCS is approximately equal to that of the main object forward RCS. On the other hand, if the incident field interacts with the deformity, the forward RCS increases.

When we compare the means and standard deviations obtained by FDTD and MoM, it could be stated that the two numerical methods yield close results.

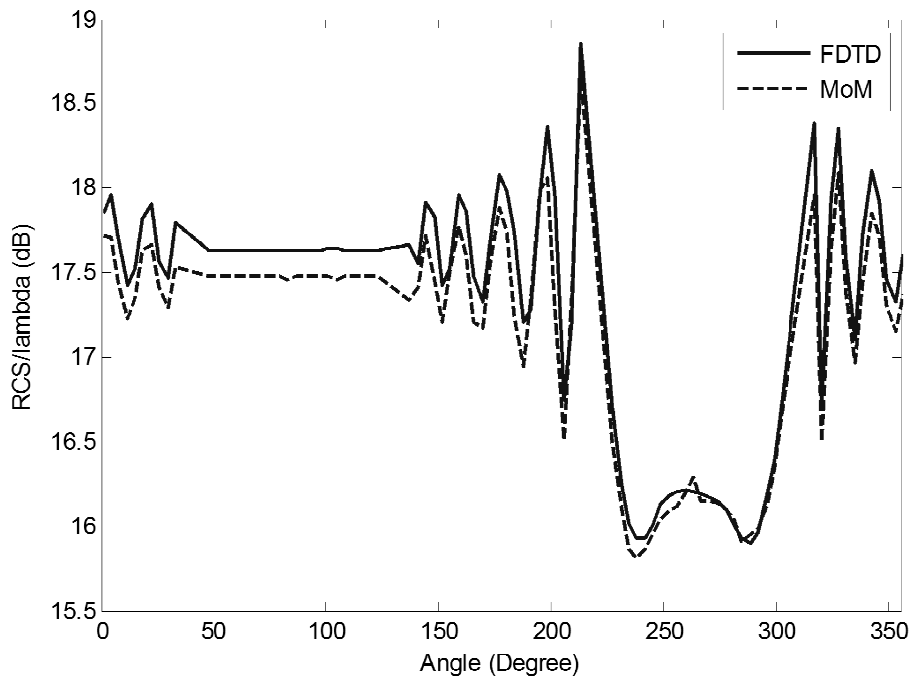


Figure 4-26 Backward RCS as a function of the angular position of the deformity via FDTD for ( $a = 3\lambda$  and  $b = 0.5\lambda$ )

Mean and standard deviations for the RCS values given in Figure 4-26 is shown in Table 4-4.

Table 4-4 Mean and Standard Deviation Values of Forward RCS in Figure 4-26

	<b>FDTD</b>	<b>MoM</b>
<b>Mean (dB)</b>	17,3572	17,1873
<b>Standard Dev. (dB)</b>	-0,3864	-0,9292
<b>Root Mean Square Error</b>	2,114	

The effect of the deformity on the backward RCS is different from that of the forward RCS. When the deformity is at the back, the backward RCS is approximately equal to the backward RCS of the main object. The backward RCS decreases when the deformity is at the front of the main object. Additionally, the backward RCS oscillates when the deformity lies at the lateral side of the main object.

It could be claimed that the backward RCS match is worse than the former one. We see that the mean difference between FDTD and MoM is only 0.1701 dB. The standard deviation is also nearly the same for two methods.

## 4.2 Effect of a Small-size Secondary Object over the RCS of a Main object

This subchapter comprises three parts to analyze the effect of small-size secondary objects over the forward and backward RCS of a main object. Also the same simulation is done via MoM (Method of Moments) and the MoM results are compared with those of the FDTD to validate the generated code.

### 4.2.1 Effect of the Dimension of the Secondary Object over RCS

The incident field comes from the angular direction  $270^0$  in all simulations below. The backward radar cross section is calculated at  $270^0$  and forward radar cross section is found at  $90^0$ .

Firstly, the effect of the dimension of the secondary object over the backward and forward RCS is going to be analyzed. The simulation domain given in Figure 4-16 is used to examine this effect. The side-length of the secondary object changes between  $0.1\lambda - 1.5\lambda$  and the secondary object positions are at  $0^0$ ,  $90^0$ ,  $180^0$ , and  $270^0$ . The side-length of the main PEC square side is equal to  $3\lambda$ .

#### 4.2.1.1 Forward RCS Simulations

The forward RCS results are given in Figure 4-27 and Figure 4-28 which are simulations for the cases when the secondary object is at  $0^0$  and  $270^0$ . The simulations at  $90^0$  and  $180^0$  are not given because these are the same as those corresponding to  $270^0$  and  $0^0$ .

When Figure 4-27 is analyzed closely, it could be seen that the forward RCS increases linearly as the side-length of the secondary object increases. When the side-length of the secondary object is  $1.5\lambda$ , the forward RCS rises 3 dB. The plot for the case when the secondary object is located at  $0^0$  is given and as mentioned above it is equal to the case corresponding to the location at  $180^0$ .

It could be seen that the forward RCS does not change with respect to the size of the secondary object for the location angle  $270^0$  in Figure 4-28. The forward RCS is approximately equal to that of the main object.

MoM and FDTD results are close enough and there is only 0.2 dB differences between these methods.

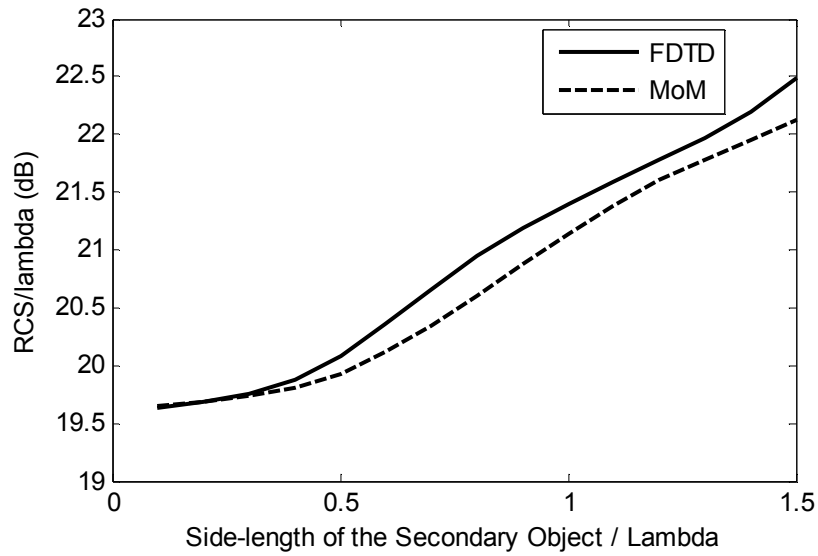


Figure 4-27 Forward RCS as a function of the side-length of the secondary object for ( $a = 3\lambda$  and  $\theta = 0^\circ$ )

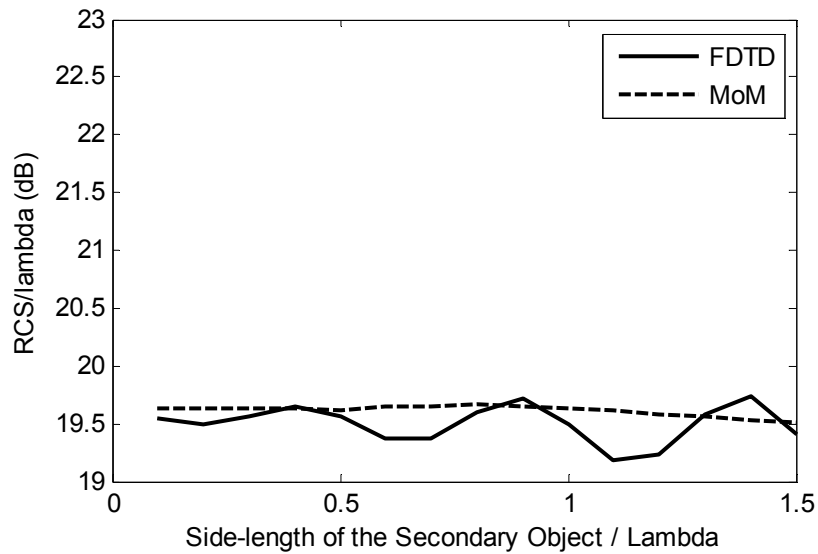


Figure 4-28 Forward RCS as a function of the side-length of the secondary object for ( $a = 3\lambda$  and  $\theta = 270^\circ$ )

As it could be understood and expected at the Figure 4-27 that the forward RCS of the PEC Square Cylinder increases while the side-length of the secondary object increases. The changes in RCS occur while the secondary object is at the lateral side of the main object (with respect to the incident field). The forward RCS does not change when the secondary object gets larger if the secondary object is located at the front or back side of the main object. The forward RCS When the side-length of the secondary object is  $1.5\lambda$ , the forward RCS is found as 3 dB (which means two times greater than that of the main object).

MoM results approximately matche with the FDTD results. The only difference is that small oscillations are observed in the FDTD results.

Another simulation is performed by reducing the side-length of the main object to  $2\lambda$ . The size of the secondary object is kept the same as the previous simulation (i.e.,  $1.5\lambda$ ). It is observed that the forward RCS increases and approaches 4 dB.

#### 4.2.1.2 Backward RCS Simulations

In this part, the effect of the side-length of the secondary object over backward RCS is examined and the results are given in Figure 4-29, Figure 4-30, and Figure 4-31 for the angular positions of the secondary object at  $90^\circ$ ,  $180^\circ$ , and  $270^\circ$ , respectively. The result for the angular position at  $0^\circ$  is not given because they are the same as those for the angular position at  $180^\circ$ .

Firstly, it is observed that the side-length of the secondary object located at  $90^\circ$  does not have considerable effect over the backward RCS. As shown in Figure 4-29, the backward RCS is almost equal to that of the main object.

Secondly, the effect of the side-length of the secondary object located at  $180^\circ$  is shown in Figure 4-30. The size of the secondary object does not influence the backward RCS until when the side-length becomes  $0.5\lambda$ . After that side-length, the backward RCS starts to increase until the side-length of the secondary object becomes  $1\lambda$ . At this side-length, the backward RCS becomes maximum and is approximately 2 dB greater than that of the main object. After that point, the backward RCS decreases dramatically with a great slope. When the side-length of the secondary object becomes  $1.5\lambda$ , the backward RCS becomes 4 dB smaller than that of the main object.

Thirdly, when the angular position of the secondary object is at  $270^\circ$ , the backward RCS shows a more complex behavior with respect to the side-length of the secondary object, as shown in Figure 4-31. The backward RCS exhibits some oscillations with local minimums observed when the side-length of the secondary object becomes  $0.8\lambda$  and  $1.3\lambda$ .

When the MoM and FDTD results are compared, they are close enough and the differences are in an acceptable range.

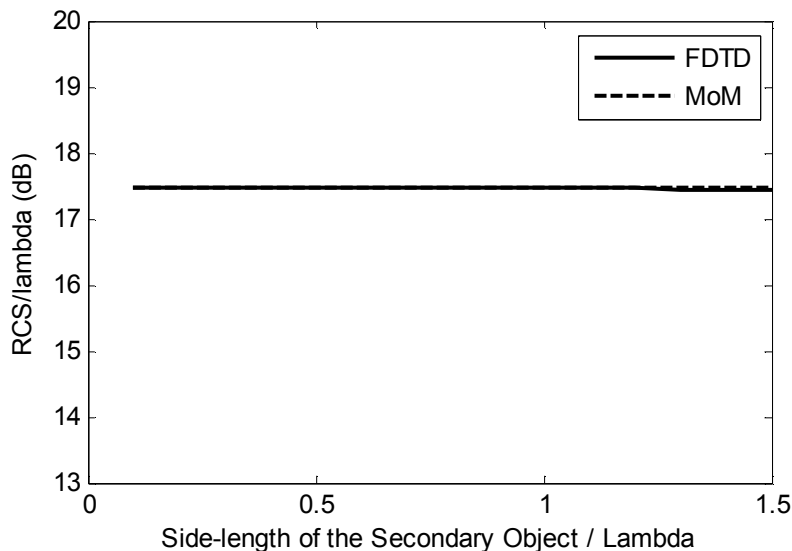


Figure 4-29 Backward RCS as a function of the side-length of the secondary object for ( $a = 3\lambda$  and  $\theta = 90^\circ$ )

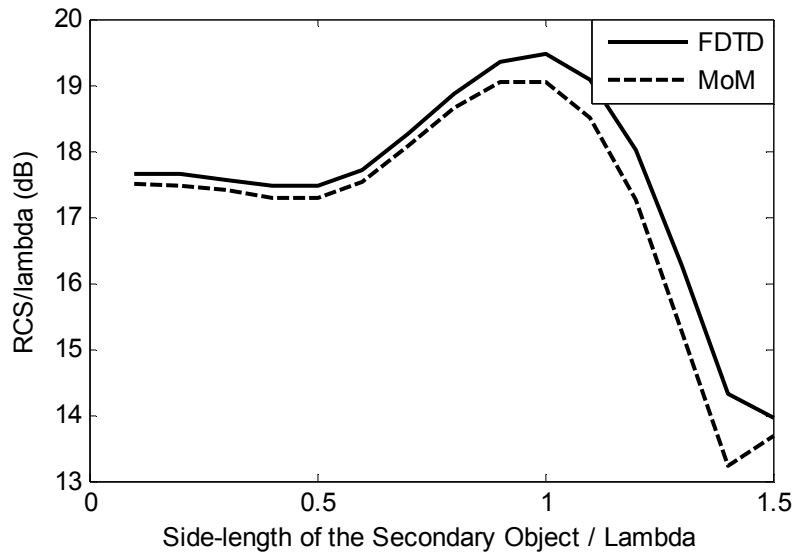


Figure 4-30 Backward RCS as a function of the side-length of the secondary object for ( $a = 3\lambda$  and  $\theta = 180^\circ$ )

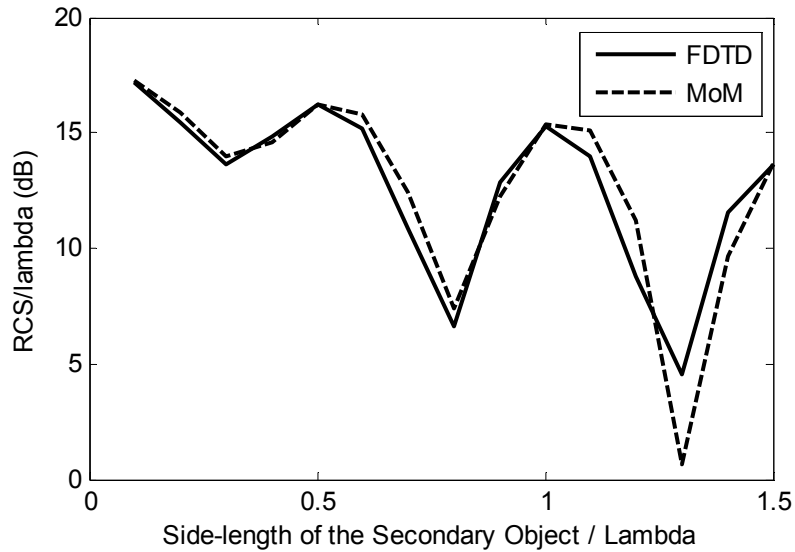


Figure 4-31 Backward RCS as a function of the side-length of the secondary object for ( $a = 3\lambda$  and  $\theta = 270^\circ$ )

The backward RCS is also plotted for different side-lengths of the secondary object in Figure 4-32. The backward RCS does not illustrate a linear relation with respect to the side-length of the secondary object. Actually, when the secondary object is at the lateral side and back side of the main object, the backward RCS slightly increases up to case where the side-length of the secondary object is  $1\lambda$ . After that, the backward RCS decreases linearly. Additionally, when the secondary object is located at the back side of the main object, the backward RCS is equal to that of the main object without secondary object.

The most interesting results are observed when the secondary object is located at the front side of main object. There is no linear relation between the backward RCS and the dimension of the

secondary object. Indeed, the backward RCS could be adjusted by changing the side-length of the secondary object. For example, the backward RCS decreases the most while the side-length of the secondary object is  $1.3\lambda$ . However, when the side-length of the secondary object is  $1.5\lambda$ , the backward RCS approaches to that of the main object without any secondary object. Also, only when the side-length is  $1.5\lambda$ , the backward RCS displays an increase.

The MoM results are also calculated, and it is observed that MoM and FDTD results are close to each other.

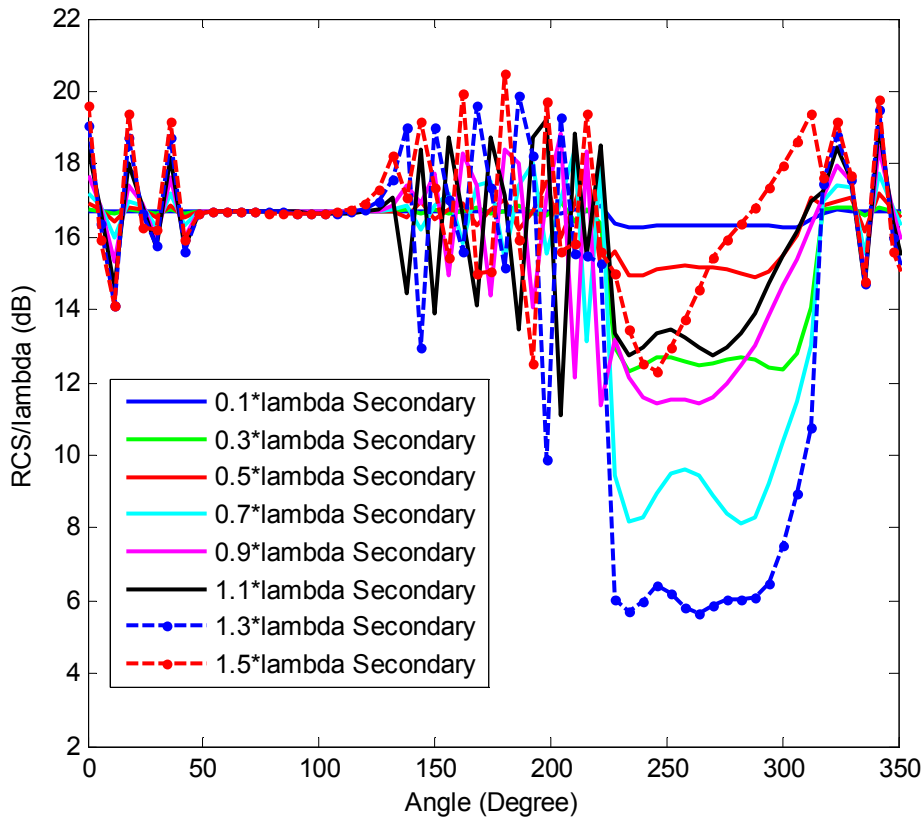


Figure 4-32 Backward RCS as a function of the angle  $\theta$  for different values of the side-length of the secondary object via FDTD for  $(a = 3\lambda)$

The simulation is also run by changing the side-length of the main object to  $2\lambda$ . It could be seen that there is a dramatic change in the RCS results when the secondary object is located at the lateral side of the main object. Again the backward RCS shows its global minimum when the side-length of the secondary object is  $1.3\lambda$  and it is at the front side of the main object.

#### 4.2.2 RCS Analysis in Plane-Missile Model

In this section, a plane – missile model is studied. The simulation area in Figure 4-33 is created to analyze a large plane (i.e., main square) and a small missile (i.e., small secondary square) going away from it.

The simulation area is illuminated by a plane wave incident from the angle  $270^\circ$ , and the forward and backward RCS are calculated. The side-length of main square is equal to  $3\lambda$ , the side-length of the

small secondary square is  $0.5\lambda$ , and the distance (c) between them is  $1\lambda$ . The forward and backward RCS are plotted with respect to the “d” distance which varies from  $1\lambda$  to  $3\lambda$ .

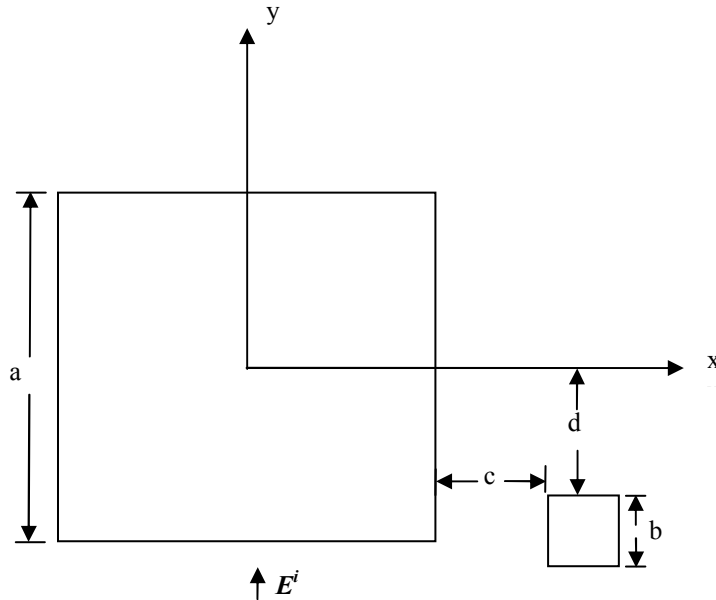


Figure 4-33 Simulation Area for Plane-Missile Model

Firstly, the forward RCS is plotted in Figure 4-34. The forward RCS does not change too much, in spite of slight oscillations, if the “d” distance is increased. The maximum variation in the forward RCS is only 1 dB. The MoM and FDTD results approximately match each other.

Secondly, the backward RCS is given in Figure 4-35. It is observed that the backward RCS fluctuates to a great extent with respect to the distance. The maximum variation in the backward RCS is around 4 dB. The FDTD does not match with MoM perfectly but the difference can be considered as acceptable. There are local maximums when the “d” distance is  $1\lambda$ ,  $1.5\lambda$ ,  $2\lambda$ ,  $2.5\lambda$ ,  $3\lambda$ ; and there are local minimums when the “d” distance is  $1.25\lambda$ ,  $1.75\lambda$ ,  $2.25\lambda$ ,  $2.75\lambda$ . The oscillation period is approximately equal to  $0.5\lambda$ .

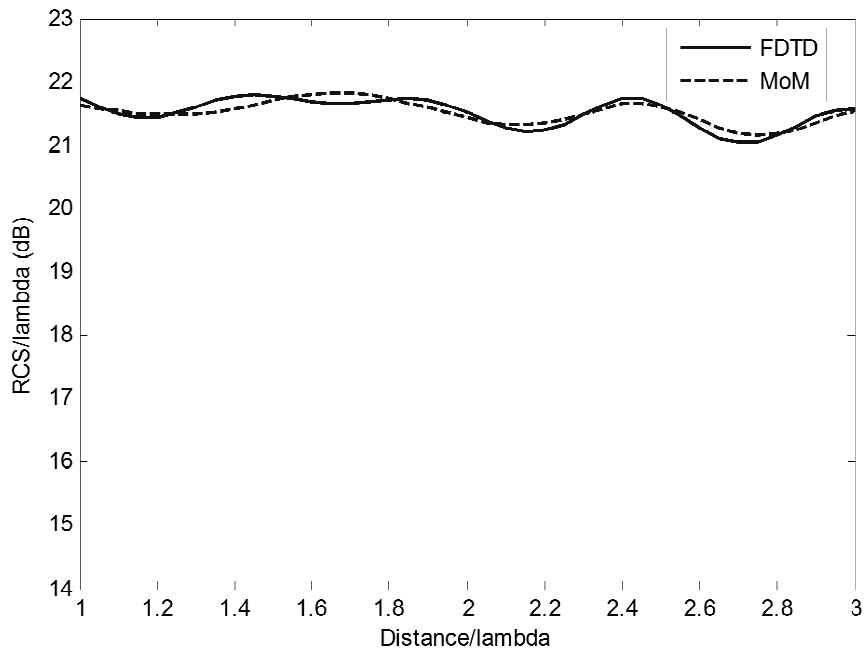


Figure 4-34 Forward RCS as a function of the distance between missile and plane ( $a = 3\lambda$  and  $b = 0.5\lambda$ ; and  $c = \lambda$ )

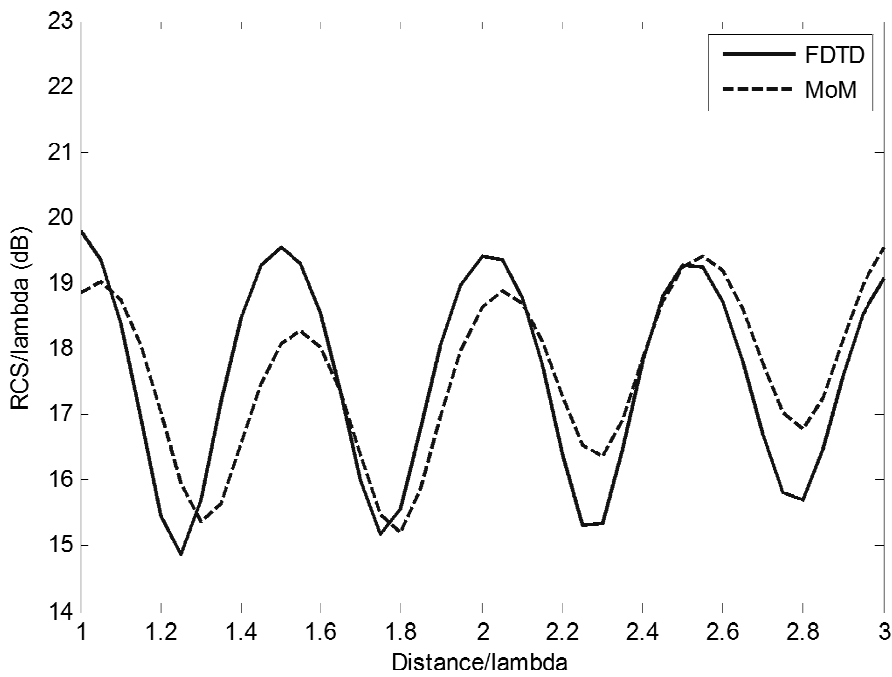


Figure 4-35 Backward RCS as a function of the distance between missile and plane ( $a = 3\lambda$  and  $b = 0.5\lambda$ ; and  $c = \lambda$ )

### 4.2.3 Effect of the Distance between the Main and Secondary Objects over RCS

In this section, the effect of the distance "c" between the main object and the secondary object over forward and backward RCS is analyzed by using the simulation area given in Figure 4-36. The distance between secondary object (small PEC square cylinder) and the main object (large PEC square cylinder) is varied from  $0\lambda$  to  $1.5\lambda$ .

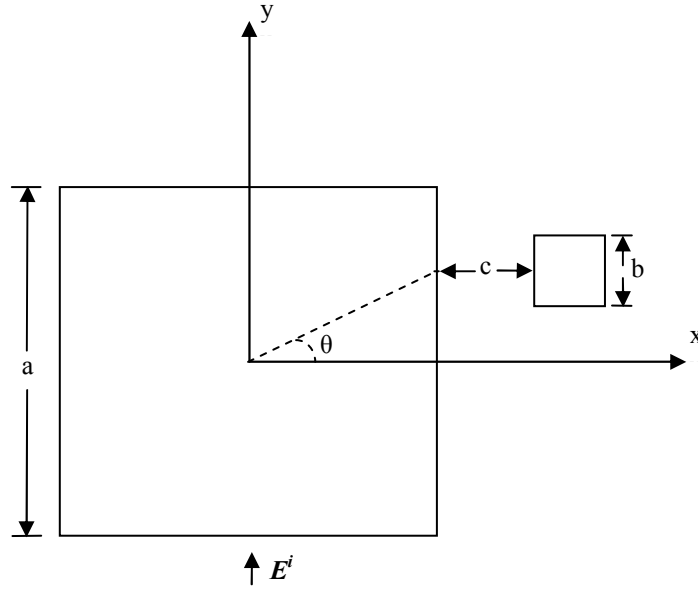


Figure 4-36 Simulation area to observe the effect of the distance between the main and secondary objects

The side-length of the main PEC square is taken as  $3\lambda$  and the side-length of secondary PEC square is equal  $0.5\lambda$ . The simulations in the following sub-sections are performed for the cases where the angular position of the secondary object is at  $0^\circ$ ,  $90^\circ$ ,  $180^\circ$ , and  $270^\circ$ .

#### 4.2.3.1 Forward RCS Simulations

The forward RCS results for the secondary object are located at the angular positions of  $0^\circ$  and  $90^\circ$  are given in Figure 4-37 and Figure 4-38, respectively. The results for angular positions at  $180^\circ$  and  $270^\circ$  are the same as those at  $0^\circ$  and  $90^\circ$ , respectively.

Firstly, the case where the secondary object is located at  $0^\circ$  is examined in Figure 4-37. It is observed that the forward RCS increases until when the distance becomes  $1.1\lambda$ . The maximum variation in RCS is about 2 dB up to this point. The RCS starts to decrease after this point.

Secondly, the case where the secondary object is located at  $90^\circ$  is illustrated in Figure 4-38. The forward RCS does not change too much, and hence, the forward RCS is almost independent of the distance between the main and secondary objects.

It is observed that the results for MoM and FDTD are approximately the same.

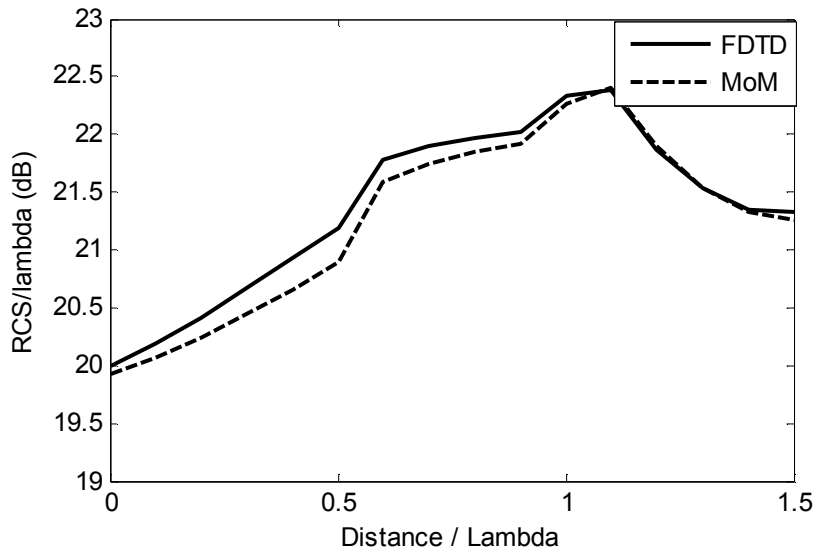


Figure 4-37 Forward RCS as a function of the distance between the main and secondary objects ( $a = 3\lambda$ ;  $b = 0.5\lambda$ ; and  $\theta = 0^\circ$ )

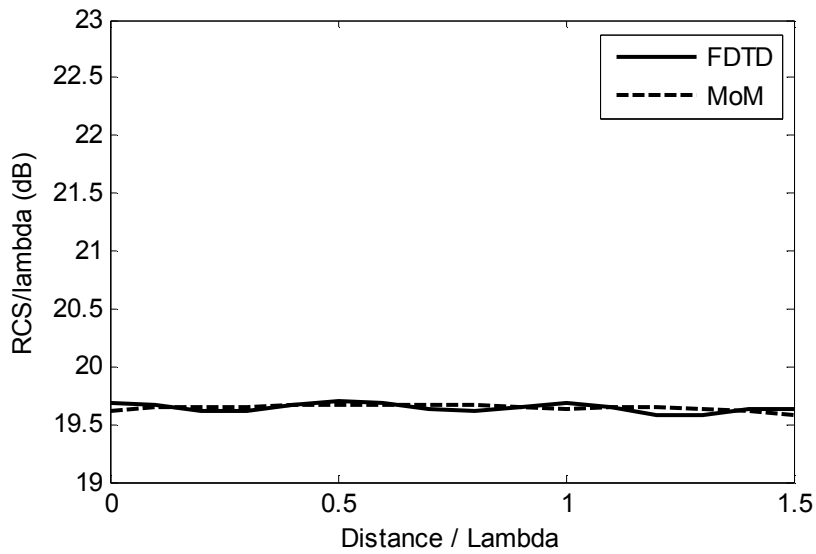


Figure 4-38 Forward RCS as a function of the distance between the main and secondary objects ( $a = 3\lambda$ ;  $b = 0.5\lambda$ ; and  $\theta = 90^\circ$ )

In this simulation, we vary the distance between a PEC square cylinder with side-length of  $3\lambda$  and a small PEC square cylinder with side-length of  $0.5\lambda$ . It is observed from the results that the forward RCS increases until when the distance becomes  $1\lambda$  and the secondary object is located at the lateral side of the main object. However, the forward RCS does not change if the secondary object is located at the front and back side of the main object.

#### 4.2.3.2 Backward RCS Simulations

The effect of the distance between main and secondary objects over backward RCS is examined in this part. Interesting results are obtained in this simulation.

Firstly, we analyze the effect of distance, when the secondary square is positioned at  $90^\circ$ . The results are given in Figure 4-39. We observe that the backward RCS does not vary with the distance and the backward RCS is nearly equal to that of the main square.

Secondly, the angular position of the secondary PEC square is at  $180^\circ$  and behavior of the backward RCS is given in Figure 4-40. The backward RCS decreases up to the point where the distance is  $0.9\lambda$ , and then it exhibits an upward regime until when the distance becomes  $1.5\lambda$ .

Lastly, the small square located at  $270^\circ$  is given in Figure 4-41. The backward RCS shows a triangular behavior with respect to the distance. The minimums are approximately measured when the distance is  $0.3\lambda$ ,  $0.8\lambda$ ,  $1.3\lambda$ , and the maximums are  $0.25\lambda$  away from the minimums. The maximum variation of RCS is about 6 dB.

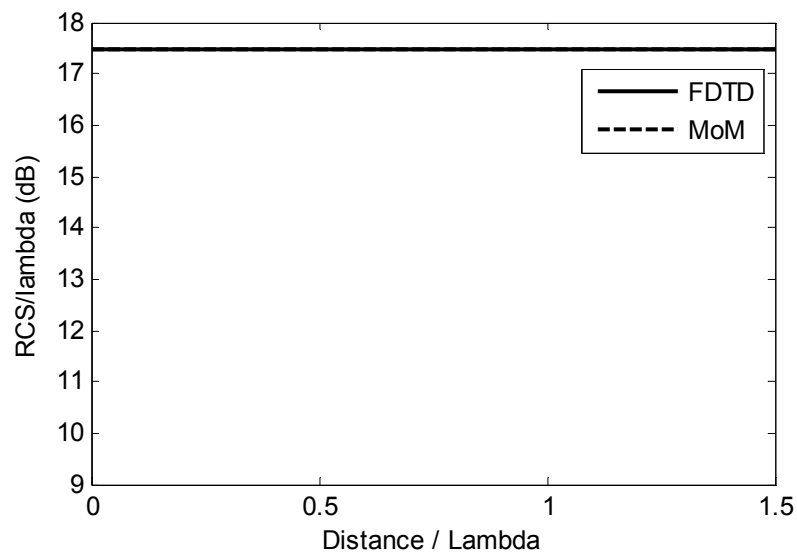


Figure 4-39 Backward RCS as a function of the distance between the main and secondary objects ( $a = 3\lambda$ ;  $b = 0.5\lambda$ ; and  $\theta = 90^\circ$ )

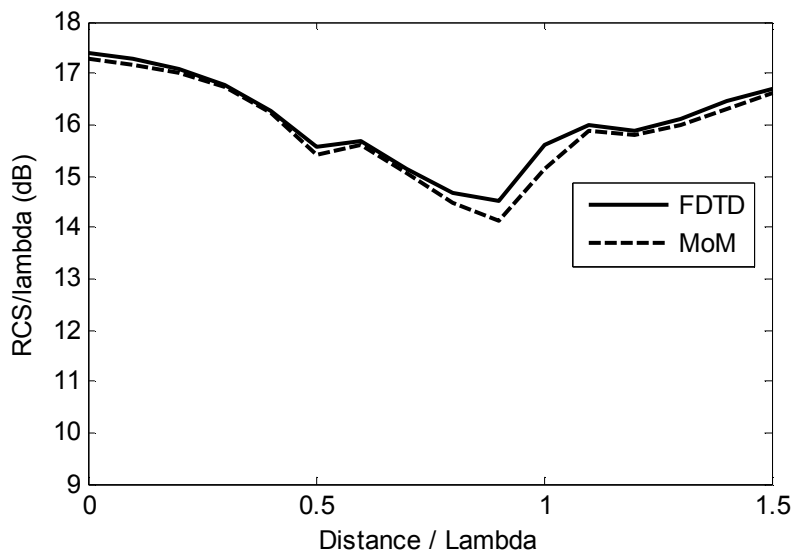


Figure 4-40 Backward RCS as a function of the distance between the main and secondary objects ( $a = 3\lambda$ ;  $b = 0.5\lambda$ ; and  $\theta = 180^\circ$ )

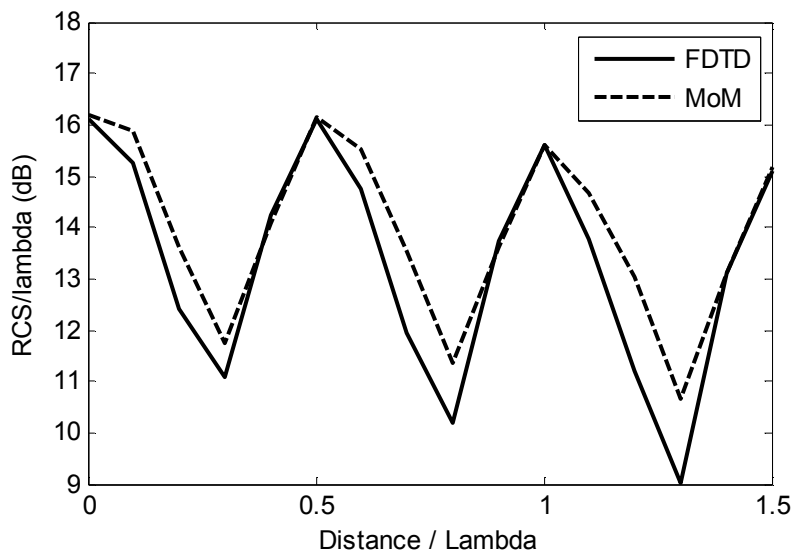


Figure 4-41 Backward RCS as a function of the distance between the main and secondary objects ( $a = 3\lambda$ ;  $b = 0.5\lambda$ ; and  $\theta = 270^\circ$ )

The behavior of the backward RCS is different from that of the forward RCS. When the secondary object is at lateral side of the main object, the backward RCS oscillates as shown in Figure 4-42. The backward RCS does not deviate from the backward RCS of the main object when the secondary object is behind the main one.

The backward RCS shows a different behavior when the secondary object is at front side of the main object. By adjusting the distance, the backward RCS could be approximately decreased to 10 dB which can be obtained by setting the distance to  $0.8\lambda$ .

In this simulations as well, the MoM and FDTD results agree well.

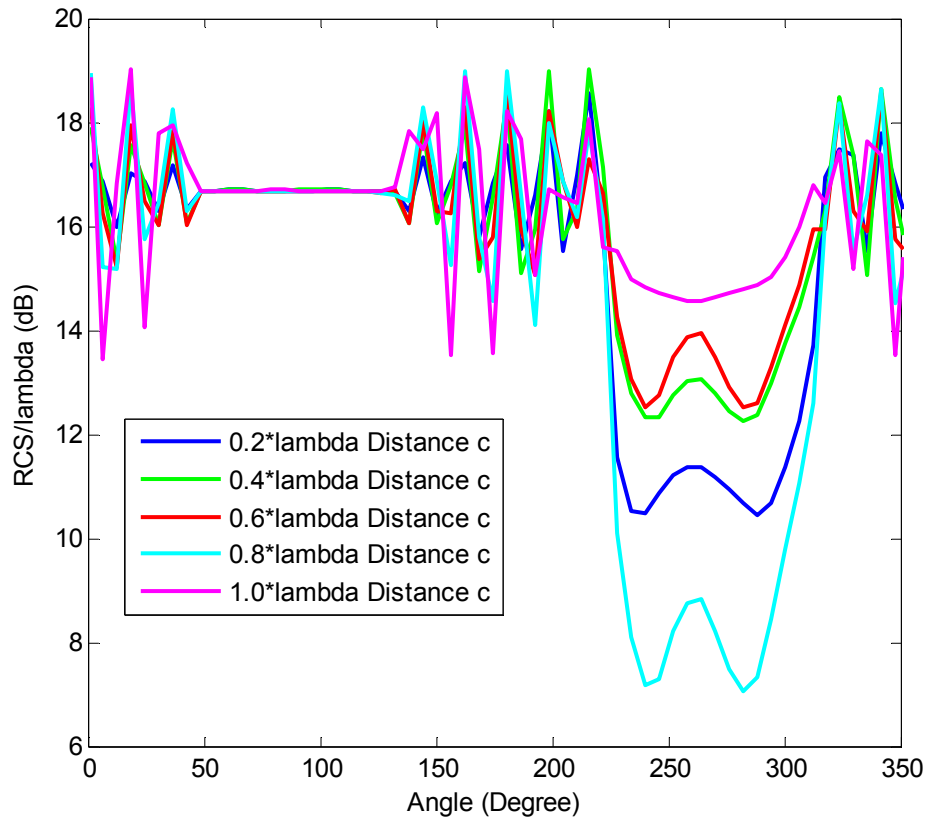


Figure 4-42 Backward RCS as a function of angle  $\theta$  for different values of distance between the main and secondary objects ( $a = 3\lambda$ ;  $b = 0.5\lambda$ )



## CHAPTER 5

### CONCLUSIONS AND FUTURE WORK

#### 5.1 Summary

In this thesis, the variations in Radar Cross Section values of dielectric and PEC objects due to material and shape uncertainties are stochastically analyzed by employing the Finite Difference Time Domain Method and the Monte Carlo approach in two dimensional electromagnetic scattering problems. The Monte Carlo technique is based on repeated sampling of a stochastic system to obtain its average behavior. There might be different varieties of this technique; but in our case, Monte Carlo is applied by generating a set of problems corresponding to different material parameters or geometries by using a probability distribution, and by solving each problem repeatedly by means of the FDTD method. The results (RCS values in our case) are collected as a family and some statistical parameters (such as mean, variance, and distributions represented by histograms) are derived from this family. Next, the results are validated through some comparisons with numerical (such as Method of Moments) or analytical results.

Since the Monte Carlo technique employs the FDTD repeatedly, an effective FDTD code is essential to get reliable results. Hence, as a first step in this thesis, two MATLAB codes have been developed and validated to analyze the electromagnetic scattering from two and three dimensional arbitrarily-shaped dielectric or PEC objects. The main steps in developing the FDTD codes can be summarized as follows: The computational domain is divided into three regions: total field region, scattered field region, and Perfectly Matched Layer to eliminate the outgoing waves. The object within the computational domain is defined by assigning proper constitutive parameters at the space lattices where the object is located. A function is generated to evaluate electrical and magnetic fields at a particular time step. In a loop, the calculation of the electromagnetic field values progresses at discrete steps in time. After computing the field values over time, the scattered fields along a hypothetical (Huygens) surface enclosing the object are transformed to phasor domain counterparts via Fourier transformation. The electrical and magnetic fields are converted into equivalent surface magnetic and electric current densities by the surface equivalence theorem. The far field electric and magnetic fields, as well as the RCS, are computed by using these equivalent currents.

After developing the FDTD code, various simulations have been performed by varying the relative permittivity and the geometry of the object. These simulations can be summarized as follows:

(i) Permittivity uncertainties have been analyzed for dielectric cylinder. It has been observed that if the variance of the relative permittivity defined by Gaussian distribution is kept small enough, the forward RCS follows a Gaussian distribution.

(ii) Shape uncertainties have been analyzed for a PEC cylinder having either an omitted part or a shape deformity in the form of a "bump", both of which have random angular positions. It has been concluded that the forward RCS of an object with shape deformity is almost equal to that of the object without deformity, when the deformity is located at the front and back sides of the object. However, the forward RCS increases as the size of the deformity increases when the deformity is at the lateral side of the object with respect to the incident field. When the deformity is located at the front, the backward RCS shows an oscillatory behavior.

(iii) The effect of a small-sized secondary object located nearby the main object has been analyzed by varying the distance between the objects, as well as the size of the secondary object. In this context, a representative missile-plane problem has been studied. It has been observed that the backward RCS exhibits an oscillatory behavior when the size of the secondary object and the distance changes at the front side of the main object.

In all these simulations, the results of the FDTD and the MoM agree well. Thus, the developed code has practical capabilities to analyze electromagnetic problems in an accurate and robust manner.

## **5.2 Future Work**

In this thesis, the FDTD code in conjunction with the Monte Carlo approach has been generated for 2-D problems. Although a 3-D FDTD code has also been developed within the context of this thesis, it has not been employed for Monte Carlo analysis yet because it is time consuming to run 3-D FDTD code repeatedly due to considerable increase in computation time. This study can be extended to 3-D problems by increasing the speed of the code.

In addition, the problems examined in this thesis have been chosen from canonical examples, rather than real-life problems. Therefore, the objects and their uncertainties can be defined more realistically, for example by using some experimental observations.

The FDTD code developed in this thesis is an effective tool to simulate and analyze various electromagnetic problems. A number of problems, such wave penetration or reflection coefficient analysis, can efficiently be simulated with the help of this code. In our future work, the modes of a cavity will be calculated by introducing a small deformity to the terminated part.

## REFERENCES

- [1] J. C. Maxwell, A Treatise on Electricity and Magnetism, Oxford at the Clarendon Press, 1873.
- [2] C. A. Balanis, Advanced Engineering Electromagnetics, John Wiley & Sons, 1989.
- [3] J. A. Kong, Electromagnetic Wave Theory, John Wiley & Sons, 1986.
- [4] R. F. Harrington, Time-Harmonic Electromagnetic Fields, John Wiley & Sons, 2001.
- [5] A. Ishimaru, Electromagnetic Wave Propagation, Radiation, and Scattering, Prentice Hall, 1991.
- [6] R. Garg, Analytical and Computational Methods in Electromagnetic, Artech House, 2008.
- [7] M. N. O. Sadiku, Numerical Techniques in Electromagnetic, CRC Press, 2001.
- [8] M. N. O. Sadiku, Numerical Techniques in Electromagnetic with MATLAB, CRC Press, 2009.
- [9] K. F. Warnick, Numerical Methods for Engineering, Scitech Publishing Inc., 2011.
- [10] W. C. Gibson, The Method of Moments in Electromagnetics, Chapman & Hall/CRC, 2008.
- [11] A. C. Polycarpou, Introduction to the Finite Element Method in Electromagnetics, Morgan & Claypool Publishers, 2006.
- [12] K. S. Yee, "Numerical Solutions of Initial Boundary Value Problems Involving Maxwell' Equations in Isotropic Media," *IEEE Transactions on Antennas and Propagation*, Vols. AP-14, no. 3, pp. 302-307, 1966.
- [13] A. Taflove, "Application of the Finite-Difference Time-Domain Method to Sinusoidal Steady-State Electromagnetic-Penetration Problems," *IEEE Transaction on Electromagnetic Compatibility*, Vols. EMC-22, no. 3, pp. 191-202, 1980.
- [14] A. Taflove, S. C. Hagness, Computational Electrodynamics: The Finite-Difference Time-Domain Method, Artech House, 2000.
- [15] K. S. Kunz, R. J. Luebbers, The Finite Difference Time Domain Method For Electromagnetics, CRC Press, 1993.
- [16] J. B. Schneider, Understanding the Finite-Difference Time-Domain Method, IEEE Press, 2011.
- [17] W. Yu, R. Mittra, T. Su, Y. Liu, X. Yang, Parallel Finite-Difference Time-Domain Method, Artech House, 2006.
- [18] D. M. Sullivan, Electromagnetic Simulation Using the FDTD Method, IEEE Press, 2000.
- [19] S. D. Gedney, Introduction to the Finite-Difference Time-Domain (FDTD) Method for Electromagnetics, Morgan & Claypool Publishers, 2011.

- [20] E. Kant, Pratik Aklın Eleştirisi, Türkiye Felsefe Birliği, 2010.
- [21] S. M. Ross, Introduction to Probability Models, Academic Press, 2007.
- [22] C. Monet, Artist, *Le gare Saint Lazare*. [Art]. Musee d'Orsay, 1877.
- [23] J. L. Devore, Probability & Statistics, Brooks/Cole, 2010.
- [24] A. Papoulis, Probability, Random Variables, and Stochastic Processes, McGraw-Hill, 2001.
- [25] D. C. Jenn, Radar and Laser Cross Section Engineering, AIAA Educational Series, 2005.
- [26] A. Taflove, K. Umashankar, "A Novel Method to Analyze Electromagnetic Scattering of Complex Objects," *IEEE Transactions on Electromagnetic Compatibility*, Vols. EMC-24, no. 4, pp. 397-405, 1982.
- [27] A. Taflove, K. Umashankar, T. Jurgens, "Validation of FD-TD Modelling of the Radar Cross Section of Three-Dimensional Structures Spanning up to Nine Wavelengths," *IEEE Transactions on Antennas and Propagation*, Vols. AP-33, no. 6, pp. 662-666, 1985.
- [28] A. Taflove, M. Brodwin, "Numerical Solution of Steady State Electromagnetic Scattering Problems Using the Time-Dependent Maxwell's Equations," *IEEE Transactions Microwave Theory Techniques*, Vols. MTT-23, no. 8, pp. 623-630, 1975.
- [29] G. Mur, "Absorbing Boundary Conditions for the Finite-Difference Approximation of the Time-Domain Electromagnetic-Field Equations," *IEEE Transaction on Electromagnetic Compatibility*, Vols. EMC-23, no. 4, pp. 377-382, 1981.
- [30] J. P. Berenger, "A Perfectly Matched Layer for the Absorption of Electromagnetic Waves," *Journal of Computational Physics*, vol. 114, pp. 185-200, 1994.
- [31] J. P. Berenger, "Three-Dimensional Perfectly Matched Layer for the Absorption of Electromagnetic Waves," *Journal of Computational Physics*, vol. 127, pp. 363-379, 1996.
- [32] Z. S. Sacks, D. M. Kingsland, R. Lee, J. F. Lee, "A Perfectly Matched Anisotropic Absorber for Use as an Absorbing Boundary Condition," *IEEE Transactions on Antennas and Propagation*, vol. 43, pp. 1460-1463, 1995.
- [33] S. D. Gedney, "An Anisotropic Perfectly Matched Layer-Absorbing Medium for the Truncation of FDTD Lattices," *IEEE Transactions on Antennas and Propagation*, vol. 44, pp. 1630-1639, 1996.
- [34] M. D. Sullivan, "An Unsplit Step 3-D PML for Use with the FDTD Method," *IEEE Microwave and Guided Wave Letters*, vol. 7, pp. 184-186, 1997.
- [35] S. D. Gedney, J. A. Roden, "Convolutional PML (CPML): An Efficient FDTD Implementation of the CFS-PML for Arbitrary Media," *Microwave Optical Tech. Lett.*, pp. 334-339, 2000.
- [36] S. D. Gedney, B. Zhao, "An Auxiliary Differential Equation Formulation for the Complex-Frequency Shifted PML," *IEEE Transactions on Antennas and Propagation*, vol. 58, pp. 838-847, 2010.
- [37] M. Kuzuoğlu, R. Mittra, "Frequency Dependence of the Constitutive Parameters of Casual Perfectly Matched Anisotropic Absorbers," *IEEE Microwave and Guided Wave Letters*, vol. 6,

pp. 447-449, 1996.

- [38] R. Luebbers, F. P. Hunsberger, K. Kunz, R. Standler, M. Schneider, "A Frequency Dependent Finite Difference Time Domain Formulation for Dispersive Materials," *IEEE Transaction on Electromagnetic Compatibility*, vol. 32, pp. 222-227, 1990.
- [39] D. J. Robinson, J. B. Schneider, "On the Use of the Geometric Mean in FDTD Near-to-Far-Field Transformations," *IEEE Transaction on Antennas and Propagation*, vol. 55, pp. 3204-3211, 2007.
- [40] K. S. Yee, "Time-Domain Extrapolation to the Far Field Based on FDTD Calculations," *IEEE Transactions on Antennas and Propagation*, vol. 39, pp. 410-413, 1991.
- [41] R. Luebbers, F. P. Hunsberger, K. Kunz, R. Standler, M. Schneider, "A Finite-Difference Time-Domain Near Zone to Far Zone Transformation," *IEEE Transaction on Antennas and Propagation*, vol. 39, pp. 429-433, 1991.
- [42] D. Sullivan, J. L. Young, "Far-Field Time-Domain Calculation from Aperture Radiators Using the FDTD Method," *IEEE Transaction on Antennas and Propagation*, vol. 49, no. 3, pp. 464-469, 2001.
- [43] S. G. Garcia, B. G. Olmedo, R. G. Martin, "A Time-Domain Near-To-Far-Field Transformation for FDTD in Two Dimensions," *Microwave and Optical Technology Letters*, vol. 27, no. 6, pp. 427-432, 2000.
- [44] A. Taflove, K. Umashankar, "Radar Cross Section of General Three-Dimensional Scatterers," *IEEE Transactions on Electromagnetic Compatibility*, Vols. EMC-25, no. 4, pp. 433-440, 1983.
- [45] A. Taflove, K. Umashankar, "User Code for the Finite-Difference Time-Domain Method," IIT Research Institute, New York, 1982.
- [46] D. M. Sullivan, "A Simplified PML for Use with the FDTD Method," *IEEE Microwave and Guided Wave Letters*, vol. 6, no. 2, pp. 97-99, 1996.
- [47] A. Taflove, M. E. Brodwin, "Numerical Solution of Steady-State Electromagnetic-Penetration Problems," *IEEE Transactions on Microwave Theory and Techniques*, Vols. MTT-23, no. 8, pp. 623-630, 1975.
- [48] D. M. Sullivan, O. P. Gandhi, "Use of PML Absorbing Layers for the Truncation of the Head Model in Cellular Telephone Simulations," *IEEE Transactions on Microwave Theory and Techniques*, vol. 48, no. 11, pp. 2033-2039, 2000.
- [49] D. M. Sullivan, Y. Xia, D. Butherus, "A Perfectly Matched Layer for Lossy Media at Extremely Low Frequencies," *IEEE Antennas and Wireless Propagation Letters*, vol. 8, pp. 1080-1083, 2009.



## APPENDIX A

### ANALYTICAL RCS CALCULATION FOR CIRCULAR CYLINDERS (2-D – TM<sub>z</sub>)

In this section, RCS is analytically computed for a circular cylinder. Firstly, the incident TM<sub>z</sub> polarized plane wave is defined as follows [4]:

$$E_z^i = E_0 e^{-jkx} = E_0 e^{-jk\rho \cos\varphi} \quad (\text{A.1})$$

Where  $j$  denotes the imaginary unit. The field can be re-expressed by utilizing the wave transformation as follows:

$$E_z^i = E_0 \sum_{n=-\infty}^{\infty} j^{-n} J_n(k\rho) e^{jn\varphi} \quad (\text{A.2})$$

$J_n$  represents Bessel Function of the first kind. The scattered field is expressed as in A.3 to characterize outward traveling waves, and the total field is expressed as a summation of the incident and scattered fields as in A.4.

$$E_z^s = E_0 \sum_{n=-\infty}^{\infty} j^{-n} a_n H_n^{(2)}(k\rho) e^{jn\varphi} \quad (\text{A.3})$$

$$E_z^i = E_0 \sum_{n=-\infty}^{\infty} j^{-n} [J_n(k\rho) + a_n H_n^{(2)}(k\rho)] e^{jn\varphi} \quad (\text{A.4})$$

Where  $H_n^{(2)}$  denotes Hankel Function of the second kind. The boundary condition must be imposed at the boundary of the circle whose radius is ( $\rho = a$ ). The tangential component of total electric field must be set to zero for a PEC circular cylinder. This condition is satisfied by setting the coefficient as follows:

$$a_n = \frac{-J_n(ka)}{H_n^{(2)}(ka)} \quad (\text{A.5})$$

The RCS of a conducting circular cylinder is driven from far field approximation that uses the asymptotic form of the Hankel Function.

$$RCS(\varphi) = \lim_{k\rho \rightarrow \infty} 2\pi\rho \left| \frac{E_z^s}{E_z^i} \right|^2 = \frac{4}{k} \left| \sum_{n=-\infty}^{\infty} \frac{J_n(ka)}{H_n^{(2)}(ka)} e^{jn\varphi} \right|^2 \quad (\text{A.6})$$

The RCS formulation for a dielectric circular cylinder is more challenging than the PEC one because of the effort in imposing the boundary condition. The incident plane wave is written in the following form by using the Addition Theorem.

$$E_z^i = E_0 e^{-jkx} = E_0 \sum_{n=0}^{\infty} \epsilon_n (-j)^n J_n(k_0 \rho) \cos n\varphi \quad (\text{A.7})$$

Where,

$$\epsilon_n = 1 \text{ if } n = 0 \text{ or } \epsilon_n = 2 \text{ if } n \neq 0 \quad (\text{A.8})$$

The scattered and total electric fields in the region exterior to the cylinder are expressed as follows:

$$E_z^s = E_0 \sum_{n=-\infty}^{\infty} \epsilon_n (-j)^n a_n H_n^{(2)}(k_0 \rho) \cos n\varphi \quad (\text{A.9})$$

$$E_z^t = E_0 \sum_{n=-\infty}^{\infty} \epsilon_n (-j)^n b_n J_n(k_1 \rho) \cos n\varphi \quad (\text{A.10})$$

Next, the magnetic field is computed from the electric field. The boundary conditions are enforced across the boundary of the circular cylinder. The tangential electric field must be continuous on the boundary. The tangential magnetic field also shows the same behavior because there is no surface current on the surface of dielectric material. The coefficients, which are unknown at the total and the scattered field formula, are calculated with the following equations.

$$a_n = \frac{\eta_1 J_n'(k_0 a) J_n(k_1 a) - \eta_0 J_n(k_0 a) J_n'(k_1 a)}{\eta_0 J_n'(k_1 a) H_n^{(2)}(k_0 a) - \eta_1 J_n(k_1 a) H_n^{(2)'}(k_0 a)} \quad (\text{A.11})$$

$$b_n = \eta_1 \frac{J_n'(k_0 a) H_n^{(2)}(k_0 a) - J_n(k_0 a) H_n^{(2)'}(k_0 a)}{\eta_0 J_n'(k_1 a) H_n^{(2)}(k_0 a) - \eta_1 J_n(k_1 a) H_n^{(2)'}(k_0 a)} \quad (\text{A.12})$$

The prime (') in the equations represents the derivative. Finally, the RCS can be computed as follows:

$$RCS(\varphi) = \lim_{k\rho \rightarrow \infty} 2\pi\rho \left| \frac{E_z^s}{E_z^i} \right|^2 = \frac{4}{k_0} \left| \sum_{n=0}^{\infty} \epsilon_n a_n \cos n\varphi \right|^2 \quad (\text{A.13})$$